Identification of the host phase(s) for vanadium in various blast furnace feed materials and the impact of material processing on this.

Master Thesis
S. Loskamp

Delft University of Technology

TU Delft

TATA

Identification of the host phase(s) for vanadium in various blast furnace feed materials and the impact of material processing on this.

by

S. Loskamp

to obtain the degree of Master of Science
at the Delft University of Technology,
to be defended publicly on Friday November 15, 2024 at 15:00.

Student number: 4690176
Project duration: February, 2023 – November, 2024
Thesis committee:

Dr. F.S. Desta,	TU Delft, supervisor
Dr. M.W.N. Buxton,	TU Delft, supervisor
Dr. J. Lewis,	Tata Steel Nederland, Company Advisor
Dr. S.A. Weihmann,	RWTH Aachen, Committee Member
Prof. Dr. R. Serna,	Aalto University, Committee Member

TU Delft

Abstract

Vanadium is a heavy metal and is reproductive and developmental toxic for mammals. Therefore, Tata Steel Nederland should prevent vanadium emissions from entering the groundwater. Consequently, a good understanding of blast furnace burden feed material's microstructural development and phase transformations is required. This thesis aims to investigate how the distribution of vanadium in iron ores changes when these are processed into pellets and how this affects the leaching potential. Therefore, a semi-quantitative approach is applied, using different analytical techniques, including XRD, SEM-EDS, LA-ICP-MS and leaching tests.

The results show that vanadium is initially hosted in the spinel structures of the magnetite iron ores. A secondary melt phase is formed during firing, where the vanadium is partially transferred to from the iron oxides. The amount of vanadium is controlled by the basicity of the pellets and the oxygen fugacity during firing. This melt phase is likely susceptible to vanadium leaching.

In conclusion, this research showed how the distribution of vanadium changed during the pelletization process. Further research is recommended to perform this study on sinter blast furnace feed material, study the influence of the oxygen fugacity in more depth, perform a more extensive leaching study and research how the leaching of vanadium from pellets can be prevented.

Keywords: vanadium, iron ores, leaching, blast furnace feed material, pellets, pelletising process, host phases, and leaching.

Preface

Before you lies the master thesis, “Identification of the host phase(s) for vanadium in various blast furnace feed materials and the impact of material processing on this.” This thesis fulfils the last requirement of the triple degree master program ”European Mining Course” organised by Delft University of Technology, RWTH Aachen and Aalto University. This thesis is written on behalf of Tata Steel Nederland, a steel manufacturer based in Velsen-Noord, the Netherlands. They provided the samples, laboratory equipment and supervision required for this research.

During the master’s program, I noticed I lacked knowledge in the fields of material science and geology. This thesis allowed me to fill that gap compared to my fellow students. This required a steep learning process. This thesis taught me how to perform laboratory work, learn about the origins of iron ores, and show how metallurgical processes work.

I am grateful for all the support and supervision from my supervisor at Tata Steel Jonathan Lewis. He guided me through this research and taught me everything I needed to know to complete this thesis. I also want to thank Frank van der Does, Jolien Linckens, James Small, Mary van Wijngaarden-Kroft, Stefan Melzer, and Vincent van Hinsberg from Tata Steel for all their help with the sample preparation and laboratory equipment. Finally, I want to thank my supervisors, Feven Desta and Mike Buxton, for their support and feedback. Everybody’s input has been crucial to delivering this end product.

Enjoy reading this report.

S. Loskamp
Delft, November 2024

Contents

Abstract i

Preface ii

List of Figures v

List of Tables vii

List of abbreviations viii

1 Introduction 1
- 1.1 Tata Steel Netherlands . . . 1
- 1.2 Hypothesis . . . 2
- 1.3 Research objectives . . . 2
  - 1.3.1 Overall research objective . . . 2
  - 1.3.2 Specific research objectives . . . 2
- 1.4 Research questions . . . 2
- 1.5 Scope . . . 2
- 1.6 Thesis outline . . . 3

2 Literature Review 4
- 2.1 Steel making process . . . 4
- 2.2 Pellets . . . 5
  - 2.2.1 Introduction to agglomeration . . . 5
  - 2.2.2 Production process of pellets . . . 6
  - 2.2.3 Materials . . . 6
  - 2.2.4 Reactions in pellets . . . 8
  - 2.2.5 Firing parameters influencing the chemistry of pellet . . . 11
- 2.3 Vanadium . . . 13
  - 2.3.1 Vanadium in pellet feed . . . 13
  - 2.3.2 Vanadium partition . . . 14
  - 2.3.3 Vanadium in slags . . . 16
- 2.4 Sensor technologies in material processing and analysis . . . 16
  - 2.4.1 XRD . . . 16
  - 2.4.2 SEM-EDS . . . 16
  - 2.4.3 PARC . . . 16
  - 2.4.4 LA-ICP-MS . . . 17
- 2.5 Key outcomes . . . 17

3 Materials 19
- 3.1 Iron Oxide-Apatite ores . . . 19
- 3.2 Input materials . . . 20
- 3.3 Fabrication of pellets . . . 21
- 3.4 Pellet fabricated by third party . . . 22

4 Methods 23
- 4.1 Analytical techniques . . . 23
  - 4.1.1 Optical microscopy . . . 24
  - 4.1.2 XRD . . . 24
  - 4.1.3 SEM-EDS . . . 26
  - 4.1.4 LA-ICP-MS . . . 27
- 4.2 PARC . . . 27
- 4.3 Leaching test . . . 28

5 Results **29**
5.1 Characterisation input materials . . . 29
5.1.1 XRD . . . 29
5.1.2 SEM-EDS JOEL 5900LV . . . 30
5.1.3 SEM-EDS JOEL 7100F . . . 31
5.2 Microstructural analysis of fired pellets . . . 35
5.3 EDS maps . . . 39
5.4 Pinhole traverses . . . 42
5.5 Chemical analysis . . . 43
5.6 XRD results for the pellet. . . . 45
5.7 LA-ICP-MS results . . . 47
5.8 Leaching tests . . . 49

6 Discussion **51**
6.1 Summary . . . 51
6.2 Model . . . 52
6.3 Mass balances . . . 53
6.4 Limitations . . . 54
6.4.1 Oxigen fugacity . . . 54
6.4.2 Leachning method . . . 54
6.4.3 Dilution of melt phase measurements . . . 54
6.5 Preventive leaching . . . 55
6.6 Reflection . . . 56

7 Conclusions and recommnedations **58**

Bibliography **60**

List of appendixes **65**

List of Figures

2.1 Steel production chain at Tata Steel Ijmuiden. 4
2.2 Schematic cross-section BF with indicative temperatures. 5
2.3 Schematic overview of straight-grate method. 7
2.4 Indicative pellet bed temperatures of induration production pellets at Tata Steel Ijmuiden. The different stages correspond to the schematic overview in Figure 2.3, with UDD as the upward drying direction, DDD as the downward drying direction and firing corresponding to the induration stage. 7
2.5 Different zones in the pellet after firing. 9
2.6 Stable phases of Fe-Si-O system at low silicon content. The red line indicates the indicative temperature of the pellet during firing. 10
2.7 Liquidus surface and sub-solidus equilibria in the CaO-FeO-SiO_2 system. In yellow are the solidus phases that can be expected based on the maximum temperature during firing. 11
2.8 SEM-EDS pellet sections at different temperatures processed with PARC to differentiate different phases. The pellet is fired from left to right at 1100, 1150, 1200 and 1300. The brown colour represents the iron oxides °C. 12
2.9 SEM-EDS pellet sections at different temperatures processed with PARC to differentiate different phases. At the top, a section is shown at the outer mantle, and the bottom is at the pellet's core. The pellet is fired from left to right at 1100, 1150, 1200 and 1300 °C. The brown colour represents the iron oxides. 12
2.10 Amount of slag and flux remnants from the shell to the pellet's core at different firing temperatures. 13
2.11 Partition coefficients obtained for V between Al and Cr spinel relative to silicate melt as a function of fO_2. All data were obtained at 1 atm and 1300 °C, except for the last measurement. 14
2.12 The relation between $\log C_{VO_4^{3-}}$ and the optical basicity at 1600°C. 15
2.13 The use of density plot to group phases in PARC, with (a) a density plot of Si and Ca for Ca-rich group of pixels only. Polygon selection of pixels tuned to correspond with backscatter electron image in Figure 2.13b, and (b) a backscatter electron image with selected pixels from density plot in highlighted orange. Image width = 512 μm. 17

3.1 Location IOA deposits worldwide. 19
3.2 Samples of various materials: (a) IOA ore sample, (b) limestone sample, (c) olivine sample, and (d) bentonite sample. 20
3.3 Fired pellets with IOA ores, produced for this research. 22
3.4 Thermocouple profile of pellet 5177. 22

4.1 Six embedded pellets in epoxy resign. 23
4.2 The optical microscope used to analyse the structures of the samples is this Zeiss Axio Imager Z1. 24
4.3 The XRD used to measure the bulk phases and proportions of the samples is this Bruker D8 Endeavour diffractometer. 25
4.4 XRD pinhole traverse of pellet 5177-1 with point analyses. 25
4.5 The SEM-EDS used for point analysis is this JEOL 5900LV. 26
4.6 The SEM-EDS used for point analysis and scanning tiles is this JEOL 7001F. 26
4.7 PARC result of pellet 5177-3 tile 51, with (a) image of PARC indicating different groups, (b) backscatter image of SEM, and (c) legend and calculated phases abundance in this tile. 28

5.1 Backscatter image of IOA ore sample using SEM-EDS at (a) area IOA ore(1), and (b) area IOA ore (24). 31
5.2 SEM backscatter images of the limestone sample: (a) zinc sulfide inclusion, (b) pyrite and quartz inclusion, (c) iron oxide and quartz inclusion, and (d) calcite with dolomite. . 32
5.3 SEM backscatter images of the olivine sample: (a) olivine with pyroxene gangue, (b) olivine with pyroxene, chromite, and pyrite inclusions, (c) particle with structures of brucite, pyroxene, chromite, and calcite, and (d) iron oxide and chromite gangue and olivine with lizardite intrusions. 33
5.4 SEM backscatter of the bentonite sample: (a) silicate with inclusions, (b) bentonite particle, (c) quartz, feldspar, Ca silicate, rutile and calcite gangue, and (d) baryte gangue. . 34
5.5 Polarised reflected light microscope images of all used pellets: (a) pellet 5177-1, (b) pellet 5177-2, (c) pellet 5177-3, (d) pellet 5171-1, (e) pellet 5171-2, and (f) pellet 9999. . 36
5.6 Micropcope and SEM images of microstructures in category 1, with (a) microscope image of the pellet 5177-2, (b) SEM image of pellet 5177-2, (c) microscope image of pellet 5171-2, and (d) SEM image of pellet 5171-2. 37
5.7 Micropcope and SEM images of microstructures in category 2, with (a) microscope image of the pellet 5177-1, (b) SEM image of pellet 5177-1, (c) microscope image of pellet 5171-1, (d) SEM image of pellet 5171-1, and (e) SEM image of pellet 9999 38
5.8 Micropcope and SEM images of microstructures in category 3, with (a) microscope image of the pellet 5177-1, and (b) SEM image of pellet 5177-1. 39
5.9 Micropcope and SEM images of microstructures in category 4, with (a) microscope image of the pellet 5177-3, and (b) SEM image of pellet 5177-3. 39
5.10 EDS maps of the core in pellet 5177-2. The brighter the colour, the higher the concentration of relevant elements, with (a) SEM backscatter image, (b) purple representing V concentration, (c) green representing Ca concentration, (d) green representing Al concentration, (e) yellow representing Cr concentration, (f) blue representing Fe concentration, (g) purple representing Mg concentration, (h) orange representing Si concentration, and (i) yellow representing Ti concentration. 40
5.11 EDS maps of the core in pellet 5177-1. The brighter the colour, the higher the concentration of relevant elements, with (a) SEM backscatter image, (b) purple representing V concentration, (c) green representing Ca concentration, and (d) brown representing Si concentration. 41
5.12 EDS maps of rutile particle. The brighter the colour, the higher the concentration of relevant elements, with (a) SEM backscatter image, (b) light blue representing Ti concentration, (c) purple representing V concentration, and (d) EDS spectrum of point analysis on rutile phase. 42
5.13 Relation between V and Ca in melt phase: (a) melt pellet 5177, (b) melt pellet 5171, (c) melt leached pellet 5177, and (d) PARC density plot of V and Ca of melt in pellet 5177 tile 3. 44
5.14 SEM image of an area near olivine particle partially dissolved in pellet 5177-1. 45
5.15 XRD powder refraction results of pellets: (a) pellet 5177, and (b) pellet 5171. 46
5.16 Results XRD pinhole traverse of pellet 5177-1 with point analyses. 47
5.17 LA-IPC-MS maps, with pixel size of 5 μm. 48
5.18 Boxplot of LA-IPC-MS data. 49
5.19 Results of leaching tests on pellets 5177 and 5171: (a) leaching V, (b) leaching Ca, (c) Leaching Si, and (d) ration leaching V/Ca. 50

6.1 Backscatter image of SEM point analysis to show the dilution of iron oxide in the melt phase. 55

List of Tables

2.1 Iron ore products. 8

3.1 Blend of different pellets. 20
3.2 Chemical composition of IOA ores with XRF (wt%). 20
3.3 Chemical composition of olivine using XRF (wt%). 21
3.4 Chemical composition of limestone using XRF (wt%). 21
3.5 Chemical composition of bentonite using XRF (wt%). 21
3.6 Chemical composition of used pellets. 21

4.1 Used standards with certified concentrations of $Fe, Na, Mg, Al, Si, Ca, V, Cr$ and Mn for LA-ICP-MS analysis. 27

5.1 XRD measurement IOA ore in compositional wt% with the std. 29
5.2 XRD measurement limestone in compositional wt% with the std. 30
5.3 XRD measurement olivine in compositional wt% with the std. 30
5.4 XRD measurement bentonite in compositional wt% with the std. 30
5.5 SEM point analysis of region 1 and 24 in IOA ore sample corresponding to Figure 5.1 in wt% oxide. 31
5.6 SEM-EDS point analysis data of the limestone sample in wt% oxide. 33
5.7 SEM-EDS point analysis data of the olivine sample in wt%. 34
5.8 SEM-EDS point analysis data of the bentonite sample in wt% oxide. 34
5.9 Mean area of melt phases, iron oxides, magnesium ferrite and other phases in different samples. The mean melt with its standard deviation is given for the total pinhole traverse, rim and core. The mean of the rim is the mean of the first 10 tiles of the traverse, and of the core is the last 10 tiles. The phase abundances are corrected for epoxy. 43
5.10 Mean area and standard deviation of the porosity in different samples. Mean of the total pinhole traverse, rim and core. The mean of the rim is the mean of the first 10 tiles of the traverse, and of the core is the last 10 tiles. 43
5.12 Pearson correlation coefficient between the concentrations of Ca and V in melt phase corresponding to data shown in Figure 5.13. 44
5.11 Statistical data on V concentrations from point analysis on different phases in pellet. . . 44
5.13 SEM point analysis in wt% oxide corresponding to Figure 5.14. 45
5.14 XRD powder diffraction results corrected for silicon standard in compositional wt%. . . . 46
5.15 Mean V concentrations of different laser-ablated areas in pellet 5177. 47
5.16 Amount of V present in pellet 5171 and amount V from that pellet leached in leachate. . 49

6.1 SEM point analysis of melt in wt% oxide corresponding to Figure 6.1, showing the dilution of iron oxide in the melt phase. 55
6.2 Different V leaching methods. 56

List of abbreviations

Abbreviaton	Definition
B_2	Basicity
BF	Blast Furnace
BIF	Banded Iron Formation
BOF	Basic Oxygen Furnace
CCS	Cold Crushing Strenght
DDD	Downward Drying Direction
DRI	Direct Reduced Iron
EAF	Electric Arc Furnace
fO_2	Oxygen Fugacity
GIF	Granular Iron Formation
IOA	Iron Oxide-Apatite
L/S	Liquid and Solid ratio
LA-ICP-MS	Laser Ablation Inductively Coupled Plasma-Mass Spectrometry
PARC	PhAse Recognition and Characterization
SDD	Silicon Drift Detector
SDD	Silicon Drift Detector
SEM-EDS	Scanning Electron Microscopy - Energy Dispersive X-ray Spectroscopy
SFCA	Silico-Ferrite of Calcium and Aluminium
SI	Spectral Image
TOF	Time-Of-Flight
TSN	Tata Steel Nederland
UDD	Upward Drying Direction
VMS	Volcanogenic Massive Sulfide
XRD	X-Ray Diffraction
XRF	X-Ray Fluorescence
Λ	Optical Basicity

1

Introduction

Vanadium (V) is a mildly incompatible transition metal. This means that V is enriched in the earth's crust and relatively depleted in the mantle. In the crust, it has the same abundance as Zn and Ni but is highly dispersed in igneous and sedimentary rocks, so concentrated mineral deposits are rare (Huang et al., 2015; Reimann & Caritat, 2012). Some relatively small reserves have been reported in Europe, but none are being exploited (Yang et al., 2021). This situation makes Europe completely reliant on suppliers like China and Russia, which account for 62% and 20% of global production, respectively. It is crucial for Europe to have access to high-strength alloys with V, which is essential for applications in industries like the aerospace industry. Since 2017, V has been added to the European Critical Raw Material list (Grohol & Veeh, 2023). Although V has a strategic value, it has an environmental downside. It is now well established that specific valence states of V pose reproductive and developmental toxicity in mammals (Domingo, 1996). Hence, emissions of V, like in groundwater, should be avoided in industries involved with this element.

1.1. Tata Steel Netherlands

Tata Steel Netherlands (TSN) receives iron ore from many places worldwide, with varying V concentrations. Most of these ores are fine-grained because of the beneficiation process of iron ores and, therefore, are not suitable for use in the blast furnace directly; this is why the ores are processed into pellets and sinters beforehand. In this process, the fine particles are mixed with fluxes and coke breeze, agglomerated, and fired so that the blast furnace burden has the required strength, porosity, and permeability (Geerdes et al., 2015). The heating process creates secondary phases that might influence the distribution of V. TSN suspects that V in iron ores do not leach but that agglomerated iron ores (e.g. pellet and sinter) do.

Measurements performed by the authorities show that the groundwater in and around the production facility is contaminated with heavy metals like V (Omgevingsdienst Noordzeekanaalgebied, 2023). According to the Dutch law 'wet bodembescherming' article 13, TSN must take remediation measures that are expected to be reasonable (van der Wilt, 2000). The emission of V into groundwater should be minimized or ideally avoided to limit environmental impact. To achieve this, a better understanding of the microstructural development and phase transformations of blast furnace burden feed material is required because this helps predict the iron ores' chemical and physical modifications (Meyer, 2016). By understanding the phase transformations and the influence of different firing conditions, TSN will get insight into effectively minimising V emissions into the groundwater caused by blast furnace burden feed material.

1.2. Hypothesis

Depending on the origin of the iron ores, they can contain varying concentrations of V. It has been shown that iron ores do not leach V, while agglomerated iron ores do. During the production process of agglomerated products, additives are added to the iron ores, and the blend is fired at high temperatures. These changes will probably create new host phases for V that differ from iron ores. These new host phases might cause V to leach. Therefore, the following hypothesis is formulated: *'The host phase of V in iron ores changes during the agglomeration process to a phase susceptible to leaching.'*

1.3. Research objectives

The current literature describes well how V is distributed in the input materials for the steel-making process and where the V ends at the end of this production process. There has been a lot of research on the chemistry of BF and BOF slags and what phases host V. What is missing in the literature is how V develops in between the steel production process. This study aims to partially fill that gap and show how the distribution of V develops during the pelletization process. The literature does provide some mechanisms that might drive the redistribution of V, namely the influence of the basicity and the oxygen fugacity during firing. These mechanisms might provide the foundation of this research.

1.3.1. Overall research objective

The main objective of this thesis is to explore how the distribution of V in iron ores alters during pelletization and assess the impact of these changes on the leaching potential of V using a Scanning Electron Microscope with Energy Dispersive X-ray Spectroscopy (SEM-EDS), X-ray Diffraction (XRD), and Laser Ablation Inductively Coupled Plasma Mass Spectrometry (LA-IPC-MS) techniques and leaching tests.

1.3.2. Specific research objectives

The specific objectives of this thesis are:

- To identify the main host phase of V and other major phases present in the pellets and input materials using SEM-EDS and XRD.
- To quantify concentrations of V in major phases of the pellets and input materials, using SEM-EDS and LA-IPC-MS.
- To identify the phases in iron pellets that leach V using the leaching tests.
- To determine the key process parameters that primarily influence the distribution of V and the leaching potential of the fired pellets.

1.4. Research questions

This thesis aims to answer the following research question:

- What is the main host phase of V in the pellets and input materials, and what other major phases are present?
- What are the concentrations of V in the major phases of the pellets and input materials?
- What phase(s) in the fired pellets leaches V?
- What key process parameters primarily influence the distribution of V and the leaching potential of the fired pellets?

1.5. Scope

This research combines qualitative and semi-quantitative analysis of fired pellets and their input materials. This means this thesis identifies phases and estimates the approximate concentrations and phase abundances. A fully quantitative analysis is not required to answer the research questions, as this research looks more generally at sources and sinks for V in iron pellets.

This research aims to provide new insights into the relationship between the leaching behaviour of V and the main host phase of the pellets. However, providing an immediate solution to prevent leaching falls outside the scope of this study. However, a suggestion has been made in the discussion. The samples used in this thesis will be limited to the pellets used by TSN. This also excludes other blast furnace feed materials like sinter. An assessment of the environmental and economic impact caused by leached V from the pellets in the vicinity of TSN is also not part of this research.

1.6. Thesis outline

This thesis has seven chapters. Chapter 1 informs the basis of the study in which the motivation, problem, objectives and research questions, and the scope of this study are addressed. The literature review is done in chapter 2. It gives the reader background information about steel production and the production of pellets and examines the existing literature that forms the foundation of this thesis. In chapter 3, the materials used for this research are introduced along with some geological information. The methodology of this research is given in chapter 4, where the data acquisition and processing techniques are described. The results of the analysis that are made are shown in chapter 5. In chapter 6, the main findings of this research are discussed. Finally, in chapter 7, the conclusions from this study are given.

2

Literature Review

This chapter gives readers insights into the background of steel production and pellet manufacturing, and the relevant existing literature is examined. Therefore, this chapter is divided into four sections. The first section briefly introduces the steel-making process and where the focus of this research fits in this production chain. The second section gives all the necessary background information about pellet production. In section three, the behaviour of V in minerals is reviewed. Finally, the most important sensor techniques used in material processing and analysis are discussed.

2.1. Steel making process

There are two major steel production routes. First is the integrated route using the Blast Furnace (BF) and Basic Oxygen Furnace (BOF). This method is accountable for 71 % of global steel production in 2023 (WSA, 2024). The second route is the Electric Arc Furnace (EAF), which is a major route for scrap or Direct Reduced Iron (DRI) and comprises 30 % of the world steel production (WSA, 2021).

Tata Steel in Ijmuiden is using the integrated route. Figure 2.1 shows the chain of production processes, with the pelletizing processes in the red box. It shows that the pelletizing of iron ores, the relevant process in this thesis, is at the beginning of the production chain. After the agglomeration of

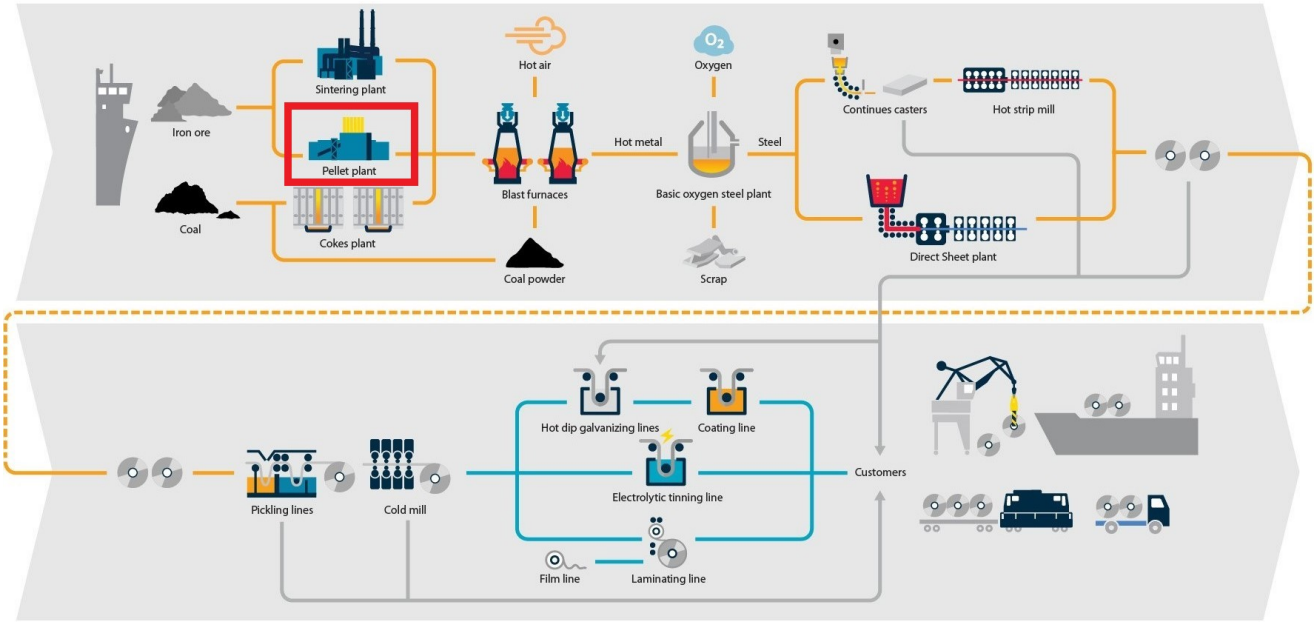

Figure 2.1: Steel production chain at Tata Steel Ijmuiden (Clarijs, 2022).

iron ores, the sinter and pellets are used in the BF, combined with cokes, to create pig iron. This needs to be converted into steel by reducing the carbon content in the pig iron. After this, the steel is refined by different processes to produce coils that meet the customers' requirements.

2.2. Pellets

2.2.1. Introduction to agglomeration

The BF is fed from the top, alternating a layer of coke and a layer of burden material like lump ore, sinter or pellets. Hot compressed air, called hot blast, is injected through tuyeres at the raceway flame, which is located near the bottom. Figure 2.2 shows that the temperature at the raceway flame rises to about 2200 °C. As the process continues, the feed material moves down, where, along the way, various reactions happen. At the bottom, pig iron and BF slag are formed and are collected separately. For the efficiency of the BF, the hot gasses must be able to flow upwards and therefore, the feed materials need to be porous (Bhagat, 2019). The problem with most iron ore products is that the product is too finely grained and, therefore, is impermeable to hot gasses. Thus, fine-grained ores must be agglomerated to larger sizes to increase airflow and reduce dust emissions. Next to that, over the years, efforts have been made to improve the efficiency of the BF and utilise a wider variety of burden materials as many high-grade ore deposits are getting depleted (Geerdes et al., 2015). The efficiency of the BF can be improved by increasing the furnace's productivity or reducing the fuel rate (Strassburger, 1969).

The following burden properties are required to operate an efficient BF and prevent clogging of burden material (Bhagat, 2019; Tupkary, 2018).

- High iron content
- Low amount of fines
- Close grain size distribution
- High cold crushing strength (CCS)
- High reduction resistance at low temperatures
- High reducibility of burden material
- Low swelling tendency
- High softening temperature with a narrow range

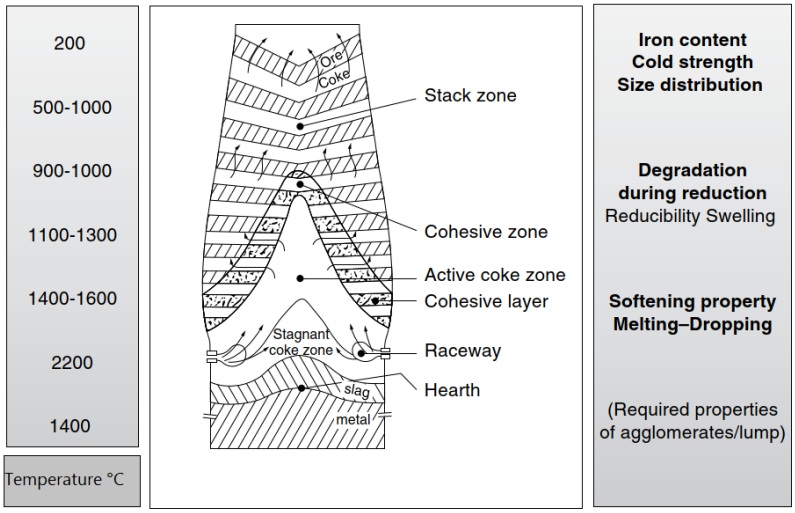

Figure 2.2: Schematic cross-section BF with indicative temperatures (Bhagat, 2019).

These criteria illustrate the necessity for implementing agglomeration methods in the production process, such as sintering and pelletizing. It produces a coarse porous burden material that is permeable to hot air (Bhagat, 2019). It also allows the addition of other materials needed to meet other requirements. On the other hand, it also shows how an agglomerated product is constrained by many requirements, which makes it complicated to change the blend of materials because this might have a trade-off.

The sintering process involves mixing iron ores with fluxes and a solid fuel, like coke breeze. This mixture is loaded on a moving grate and fired from the top. The combustion front moves from the top of the bed to the bottom, forming strong bonds between the particles. After the sinter process is completed, the sinter cake is tipped off the grate, breaking the cake into coarse particles (Ball et al., 1973; Bhagat, 2019).

In contrast to the sintering process, the pelletizing process is somewhat more controlled. First, spherical-shaped green balls are produced from fine-grained iron ores with additives. The result is a small, spherical-shaped, porous and strong pellet with a diameter of about 10 - 16 mm (Ball et al., 1973). The pellets can be used in the BF or the direct reduction plant, but the DRI pellets hold a lower gangue content (Mourao et al., 2020). The pelletizing process is explained in Subsection 2.2.2.

In general, the biggest difference between sinter and pellets is that sinter is not strong enough to withstand long-distance transportation, while pellets are. There are chemical differences between the two; the most important are that the pellets have lower basicity (B_2), a higher Fe content and a lower gangue content. The basicity is the ratio of basic oxides (typically CaO) to acidic oxides (typically SiO_2). The basicity is an important parameter in the ironmaking process, as it can significantly affect the efficiency and quality of iron production. Because of the chemical differences, pellets have the advantage over sinter that fewer fluxes are required, less slag is formed, and lower fuel consumption is required (Mourao et al., 2020).

2.2.2. Production process of pellets

According to M. Meyer et al. (2016) and Tupkary (2018), the pelletising process consists of three stages:

1. Feed preparation: comminution, screening and mixing of different iron ores to ensure homogenisation of the physical and chemical properties of the pellet's ore feed, which is then mixed with fluxes, coke breeze and binder.

2. Balling process: formation of green pellets in rotating drums or disks. Adding water to the mixture while rotating the drums or disks forms small round pellets that gradually grow until the desired size is achieved.

3. Induration process: green pellets are dried, fired, and cooled. In this stage, new slag bonds are formed between the particles, enhancing the pellets' physical properties. The reactions taking place in this stage are explained in Subsection 2.2.4.

Two methods could be applied for the induration process: the straight-grate and grate-kiln-cooler methods (Bhagat, 2019). The straight-grate method is used at Tata Steel in IJmuiden, and a schematic overview of this method is given in Figure 2.3. It is shown that the pellets are dried in two stages before induration, and afterwards, they are actively cooled down. Figure 2.4 shows the indicative temperature profiles of the pellets at different zones in the pellet bed and corresponds with the different stages as is shown in Figure 2.3. It is shown that during the initial drying stage, UDD, the pellet bed is heated from the bottom, resulting in a small peak in the temperature of the bottom zone. Afterwards, the pellet is dried and fired from the top. At the end, the pellet bed is cooled from the bottom. This is why the top layer reaches a higher temperature and for a longer duration than the bottom layer. This is important because the pellets at the top are better fired than pellets at the bottom and therefore show different characteristics.

2.2.3. Materials

Iron ores make up the majority of the pellet material. Additives are added to iron ore concentrates to enhance their properties during the pelletising process and improve the properties of fired pellets. The required additives are fluxes, coke breeze and bentonite.

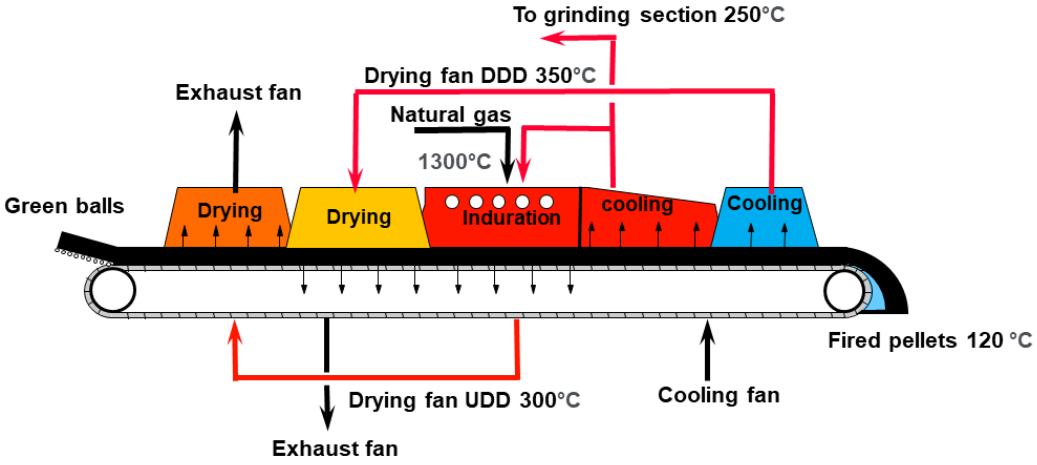

Figure 2.3: Schematic overview of straight-grate method (Xiao & Pacheco, 2022).

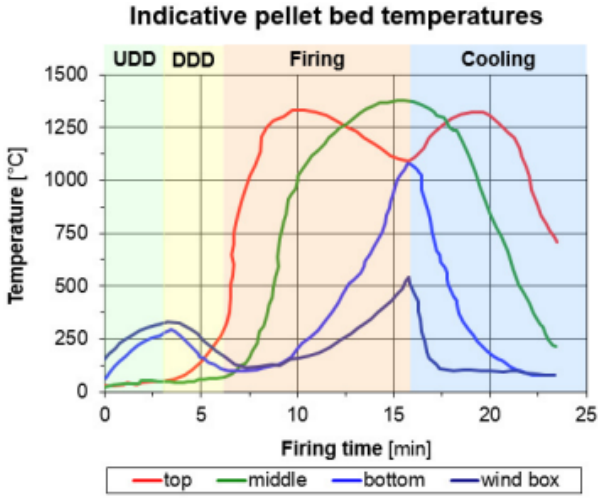

Figure 2.4: Indicative pellet bed temperatures of induration production pellets at Tata Steel Ijmuiden. The different stages correspond to the schematic overview in Figure 2.3, with UDD as the upward drying direction, DDD as the downward drying direction and firing corresponding to the induration stage (Small & Firth, 2023).

.

Iron ores

Iron in the Earth's crust is most abundant as a (hydro)oxide and minor as a carbonate, sulfide, or silicate. The most common minerals that source iron are hematite, magnetite, and goethite. Magnetite has the highest iron content of 72.4 wt % and has a spinel structure. It is found in all types of rocks: igneous, metamorphic, and sedimentary. Pure hematite has an iron content of 69.9 wt% and has a trigonal structure. Hematite, too, can also be found in all types of rocks. Weathering of other iron minerals can lead to the formation of goethite. Goethite has an iron content of 62.8 wt% and has an orthorhombic crystal structure (Bhagat, 2019; Smil, 2016).

The most common iron ore deposits are sedimentary deposits formed during the Precambrian. Iron oxides precipitated on the ocean floors in these sedimentary rocks. These can be divided into two types. The first type is the Algoma-type iron formation interlayered with submarine-emplaced volcanic rocks or volcanogenic massive sulfide (VMS) deposits. The second type is the Superior-type iron formations, which lack a direct link with volcanic rocks. Based on the texture, the sedimentary rocks can also be divided into the Banded Iron Formation (BIF) or Granular Iron Formation (GIF) (Bekker et al., 2010). Iron ore deposits can also be formed by igneous and hydrothermal processes, like iron oxide-apatite deposits (Knipping et al., 2015).

Depending on the size, iron ore can be categorised into three different products: lump ore, fines, and concentrate. Only lump ore is big enough to be used directly in the BF. This is high-grade iron ore and only requires a grinding and crushing process to meet the size requirements, but it has become increasingly scarce (Ball et al., 1973; Geerdes et al., 2015). Low-grade ores require a beneficiation process to meet the required iron content. For this process, the minerals must be liberated from the gangue material by comminution (e.g. crushing and grinding) before these are separated. This results in finely-grained concentrates. Some low-grade ores can not be beneficiated but still have economic value; these are crushed to fines (Ball et al., 1973; Jankovic, 2015). Table 2.1 shows the different products and their applications.

Although the beneficiation process removes gangue material, it is not feasible to remove all of it. There are three categories of gangue material. The first is a slag-forming gangue containing acid oxides like silica (SiO_2) and aluminium oxide (Al_2O_3). These acid oxides will form bonds with base oxides (CaO and MgO), forming slag phases. The second category is metallic oxides. These oxides, like MnO, CrO, and TiO, will partially reduce to metal. The final category is deleterious impurities. This contains sulphur and phosphorous and impacts steel negatively and should therefore kept to the minimum (Ball et al., 1973).

Table 2.1: Iron ore products (Ball et al., 1973; Small & Firth, 2023).

Product	Production	Size range (mm)	Application
Lump ore	Sized product	10-40	Direct BF feed
Fines	Result from sizing lump ore or deliberate crushed	1-10	Sinter
Concentrate	Result from beneficiation process	<1	Pellet

Fluxes
As stated before, iron ores contain acid oxides SiO_2 and Al_2O_3, which can be neutralised by adding base oxides CaO and MgO and will form slag phases. Fluxes are typically used in the form of limestone ($CaCO_3$), dolomite ($CaMg(CO_3)_2$), and olivine ($(Mg,Fe)_2SiO_4$). Adding fluxes to the pellets has several advantages; for example, it improves the strength of the pellet, increases the reduction rate, increases the softening temperatures and reduces the swelling of the pellets (Bhagat, 2019; Boucher & Wilhelmy, 2007). The addition of fluxes is also important for the BF slag chemistry. Granulated blast furnace slag, which is fast-cooled, is a by-product used in cement production as a partial replacement for clinker (Bilim et al., 2009).

Solid fuel
Solid fuel, typically coke breeze, is added to the mix as an internal energy source. This lowers fuel consumption during the induration process and accelerates the pelletizing process. Cokes are produced in the coke plant, where coal is heated to remove volatile constituents like sulphur. The cokes are then crushed to a particle size <12 mm to make it coke breeze (Mousa et al., 2016).

Binder
Binders provide green balls with a certain strength but also increase the strength of fired pellets. Bentonite is typically used as a binder, which is a montmorillonite clay formed from altered volcanic ash. Because of its swelling and colloid properties, it has proven to be a good binder (Ball et al., 1973; Bhagat, 2019; Dehn & McNutt, 2015).

2.2.4. Reactions in pellets
In a book written by Boucher and Wilhelmy (2007), it is well explained how iron ores reduce and oxidise during the induration process. When firing the pellets, the coke breeze will partially burn, which causes high levels of CO_2. This restricts the access of O_2 in the core of the pellets, causing incomplete combustion of the remaining coke breeze. The $CO2$ becomes unstable at high temperatures and reacts with solid coke, forming CO, shown in equation (2.1). The CO reduces primary hematite to secondary magnetite according to equation (2.2). The reduction front moves from the core to the shell of the pellet (Boucher & Wilhelmy, 2007).

$$CO_2(g) + C(s) \rightarrow 2CO(g) \tag{2.1}$$

$$3Fe_2O_3(s) + CO(g) \rightarrow 2Fe_3O_4(s) + CO_2(g) \tag{2.2}$$

$$4Fe_3O_4(s) + O_2(g) \rightarrow 6Fe_2O_3(s) \tag{2.3}$$

Depending on the coke content and firing conditions, primary and secondary magnetite is oxidised to secondary hematite at the induration process's cooling stage, as shown in equation (2.3), because the abundance of CO and CO_2 is replaced with an abundance of O_2. The oxidation front moves from the shell to the pellet's core, although, depending on the conditions, it may not fully be oxidised in the pellet core (Boucher & Wilhelmy, 2007). Because the oxidation front and reduction front move in different directions and don't entirely reduce or oxidise the entire pellet, it causes a heterogeneous pellet with varying hematite, magnetite and slag content, as well as varying grain size and porosity. Hence, the pellets can be divided into four zones: the shell, outer mantel, inner mantel, and core. This and the characteristics of the zones are shown in Figure 2.5 (Boucher & Wilhelmy, 2007).

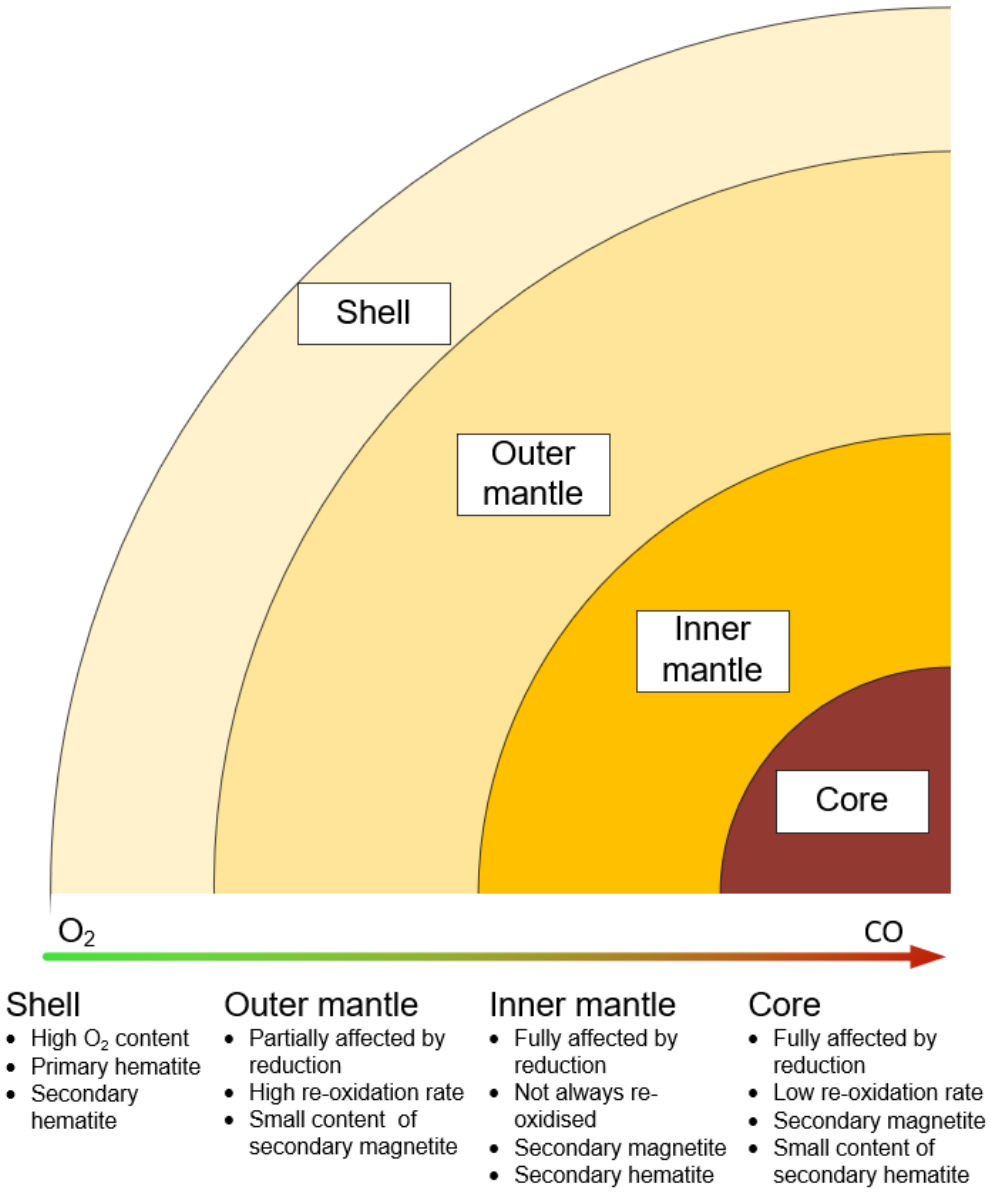

Figure 2.5: Different zones in the pellet after firing.

Figure 2.6 shows the Fe-Si-O phase diagram, which shows what phases are formed under varying temperatures and pCO_2/pCO partition ratios, which tells something about how reduced the environment is. The red line shows the indicative temperature at which the pellets are fired. Under normal firing conditions, silica will completely dissolve and form a melt phase. When the temperature is too low, fayalite (Fe_2SiO_4) is formed or the silica remains intact, which could occur in the bottom zone of the pellet bed. If the silica source, like quartz, mica or olivine, doesn't dissolve, it will lower the fusion temperature of iron oxides around the silica source, resulting in precipitated iron oxides in the rim of the silica source (Boucher & Wilhelmy, 2007). The diagram also shows that if the pCO is too high, wüstite is formed at temperatures above 1200°C.

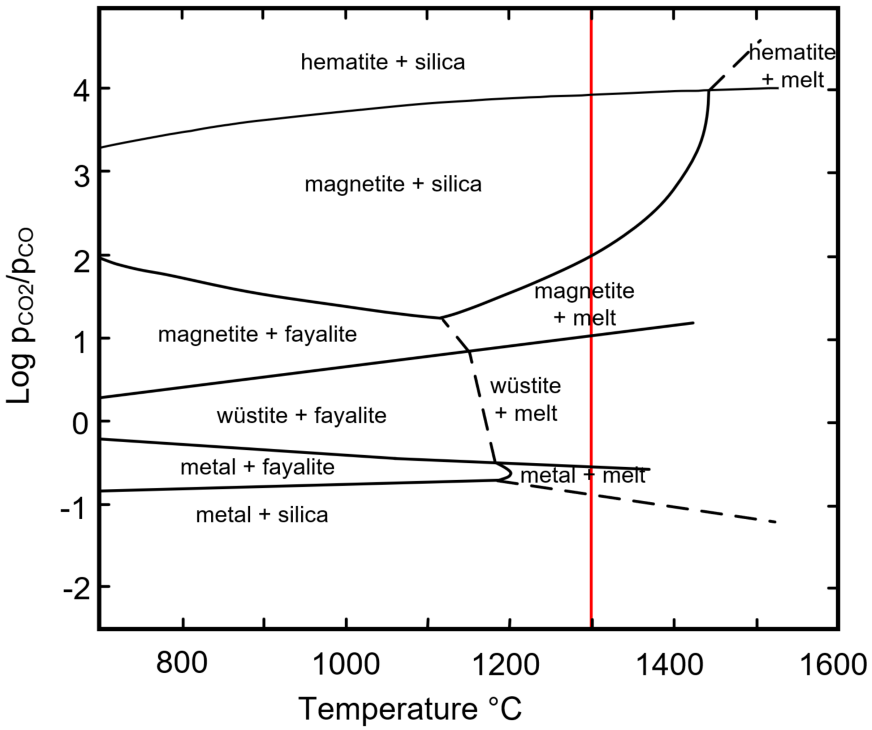

Figure 2.6: Stable phases of Fe-Si-O system at low silicon content. The red line indicates the indicative temperature of the pellet during firing (Darken, 1948).

When heating calcium sources, CaO is liberated. This can react with silica and form orthosilicate ($CaO{\cdot}SiO_2$) at 1000 °C, which is very stable and prevents the formation of iron silicates (K. Meyer, 1980). Figure 2.7 shows a phase diagram of the $CaO - FeO - SiO_2$ diagram, with maximum temperatures of the pellets reached during induration in yellow. It is shown that calcium is able to react with hematite, forming calcium ferrite ($CaO \cdot Fe_2O_3$). With an abundance of Ca, also dicalcium ferrite ($2CaO \cdot Fe_2O_3$) can be formed, but the surrounding iron oxides will assimilate this to form calcium ferrite (Boucher & Wilhelmy, 2007). Depending on the Ca and Fe content and the firing conditions, calcium diferrite ($2CaO \cdot 2Fe_2O_3$) could be formed, although this is very unstable. At a temperature of 1230°C, this will decompose in the melt and Fe_2O_3, and below 1120 °C, decompose in calcium ferrite. A glassy slag phase is formed when SiO_2, CaO, and Fe_2O_3 react under an oxidising atmosphere. M. Meyer et al. (2016) describes that if the Ca content in the pellet is high enough to form, calcium ferrite phases are formed besides the glassy melt phase.

If the temperature increases more than 1300 °C and calcium ferrite phases are present, these phases, together with silicates, form complex silico-ferrite of calcium and aluminium (SFCA) structures (Boucher & Wilhelmy, 2007). The iron pellets should not reach this temperature, so no SFCA should be expected.

MgO reacts with magnetite, stabilising the spinel structure and preventing oxidation to hematite. The product is a magnesium ferrite ($Mg(Fe^{3+})_2O_4$) and forms closely to the MgO source because MgO is not very mobile (Panigrahy et al., 1984). With local high concentrations of MgO, periclases could be formed, which together with iron oxide forms a ferroan periclase (Boucher & Wilhelmy, 2007).

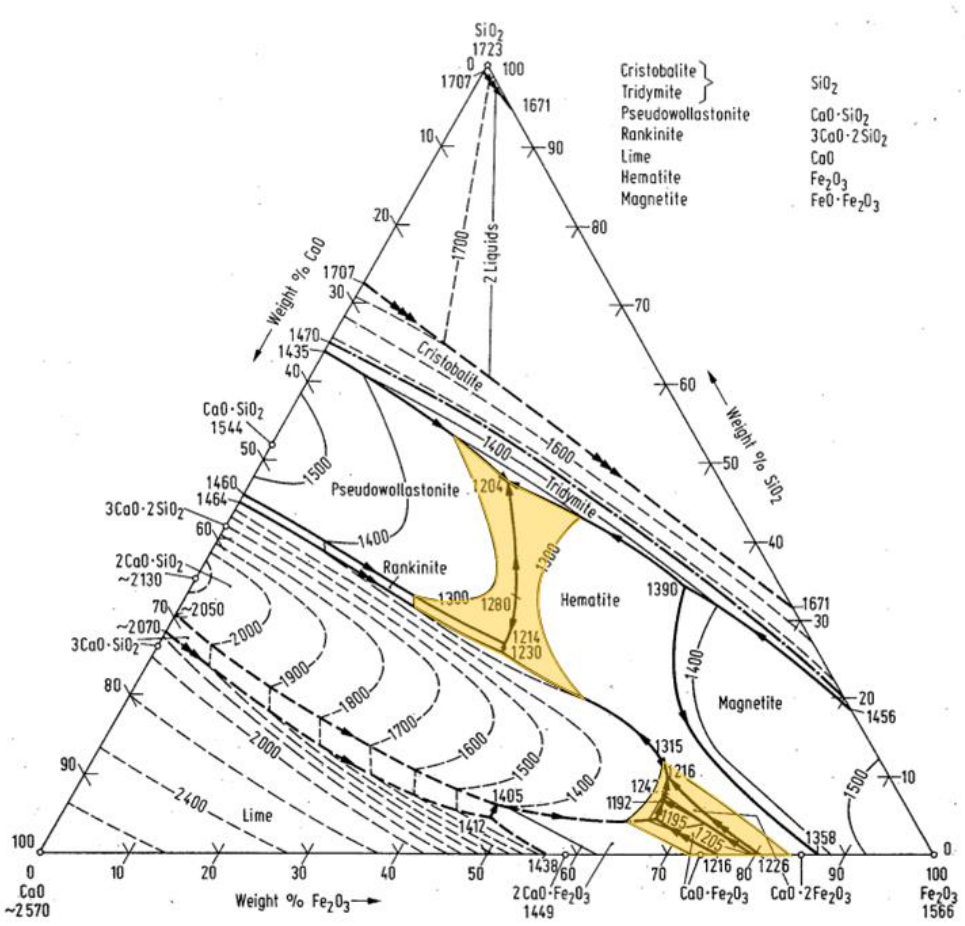

Figure 2.7: Liquidus surface and sub-solidus equilibria in the CaO-FeO-SiO_2 system. In yellow are the solidus phases that can be expected based on the maximum temperature during firing (Allibert, 1995).

2.2.5. Firing parameters influencing the chemistry of pellet

TSN has researched the influence of temperature on the chemistry of the pellets. Figure 2.8 shows that the temperature influences the reactions during induration. At 1100 °C Ca, the fluxes start to react with the iron oxides around the flux particles forming calcium ferrites. As the temperature increases to 1200 °C, the calcium ferrites decompose in hematite and melt, as is described in Subsection 2.2.4. From 1150 °C, the Mg from the dolomite fluxes starts to react with the iron ores, which must be a magnetite ore, forming magnesium ferrites. As the temperature keeps increasing, the number of magnesium ferrites keeps rising. The silica gangue material still exists at 1200 °but entirely dissolves at 1300 °C. As seen in Figure 2.7 in Subsection 2.2.4, the temperature on which magnetite and silica become magnetite and melt phase depends on the ratio between CO_2 and CO present in the environment, but varies somewhat between 1150 and 1450 °C. In conclusion, the higher the temperature, the more the flux and gangue material starts to react with the ore, and the more secondary phases are formed, like magnesium ferrites and slag.

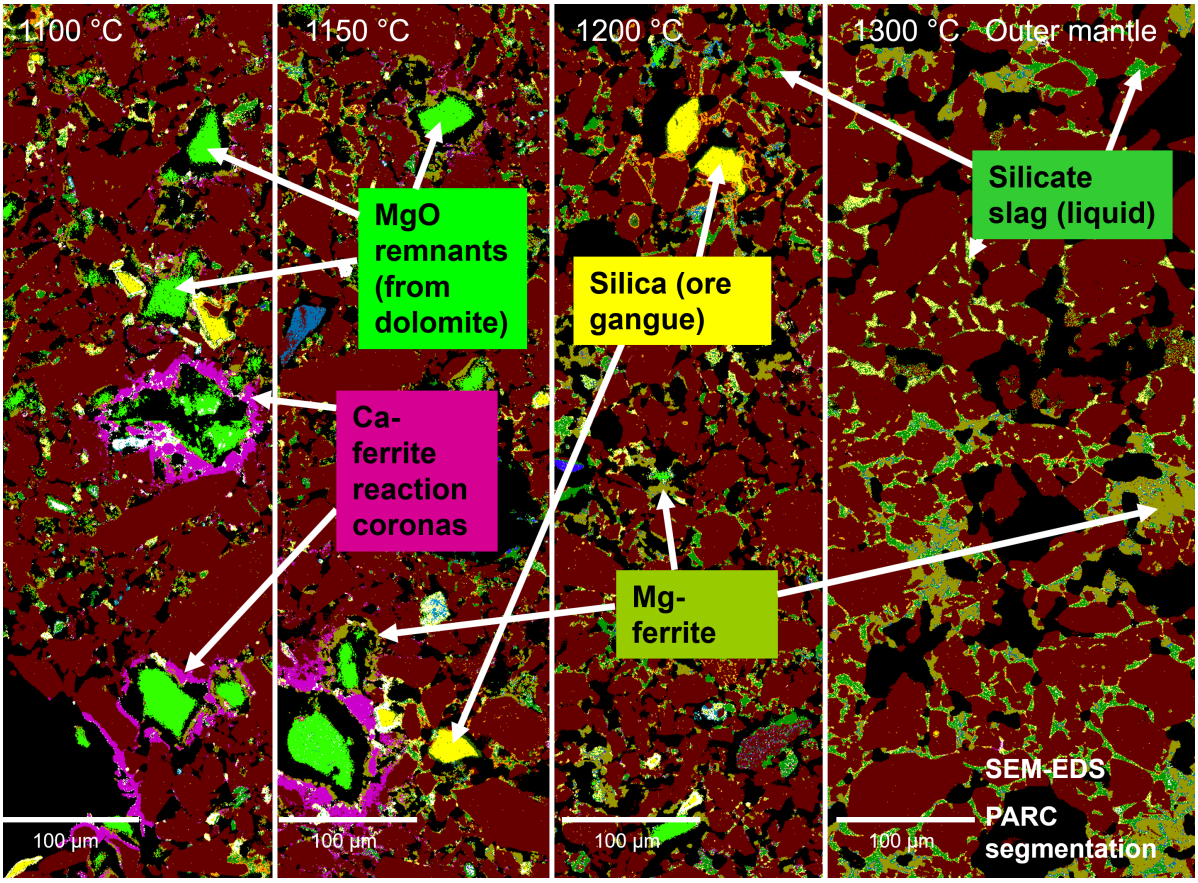

Figure 2.8: SEM-EDS pellet sections at different temperatures processed with PARC to differentiate different phases. The pellet is fired from left to right at 1100, 1150, 1200 and 1300. The brown colour represents the iron oxides °C (Small & Firth, 2023).

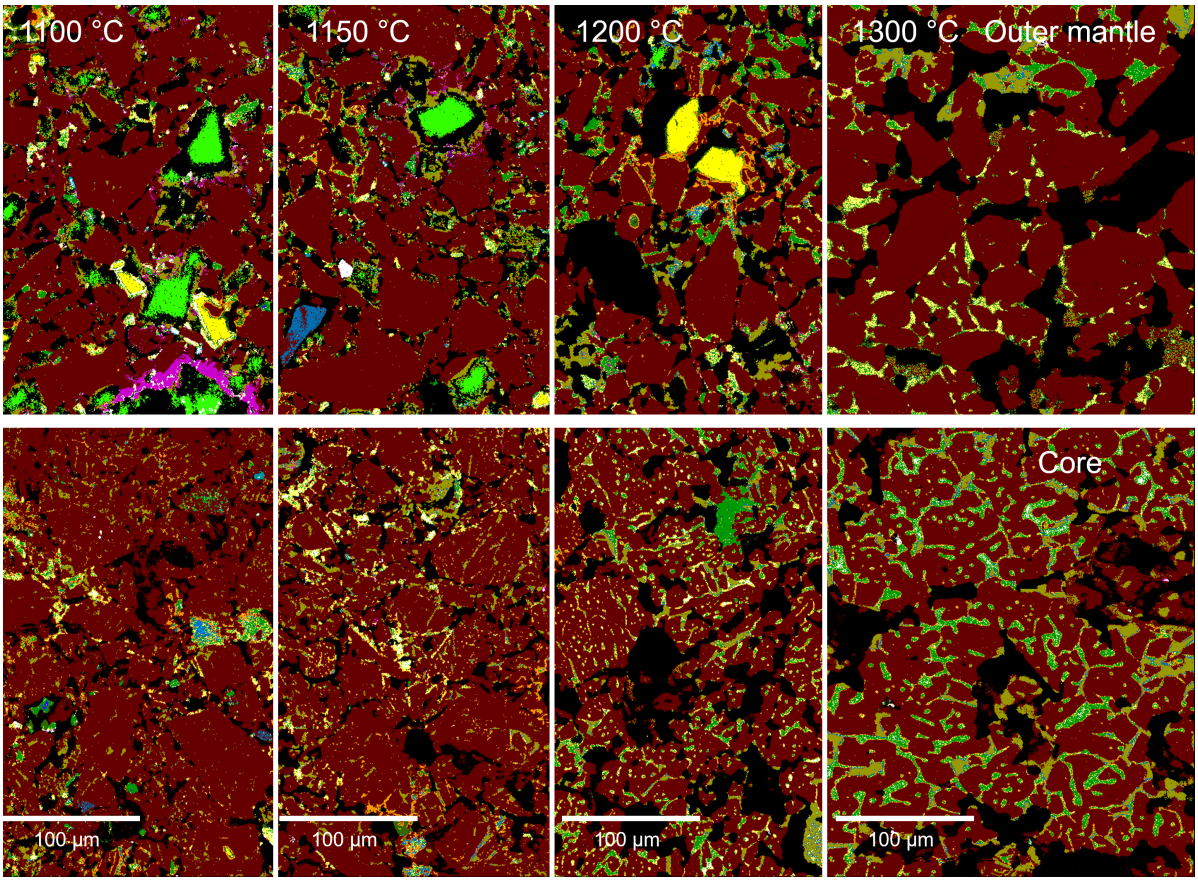

Figure 2.9: SEM-EDS pellet sections at different temperatures processed with PARC to differentiate different phases. At the top, a section is shown at the outer mantle, and the bottom is at the pellet's core. The pellet is fired from left to right at 1100, 1150, 1200 and 1300 °C. The brown colour represents the iron oxides (Small & Firth, 2023).

Figure 2.9 shows the difference in the structure between the core and the outer mantle at different temperatures. This is caused by the difference in O_2 concentration in the environment, in other words, the oxygen fugacity (fO_2). As is explained in Subsection 2.2.4, the reduction front moves from the core to the shell, and the oxidation moves in the opposite direction, influencing the microstructure and mineralogy. The outer mantle shows easily identifiable particles with a slag phase in between. The core shows that all the phases are more intergrown, and the iron ores have sintered together. The core also shows less flux and gangue material, while more slag and other secondary phases. Even at the lower temperatures of 1100 and 1250 °C, there is a big difference between the amount of fluxes left and the amount of secondary phases formed. This is also illustrated in Figure 2.10, where the slag and fluxes area% are calculated from the shell to the pellet's core at different temperatures.

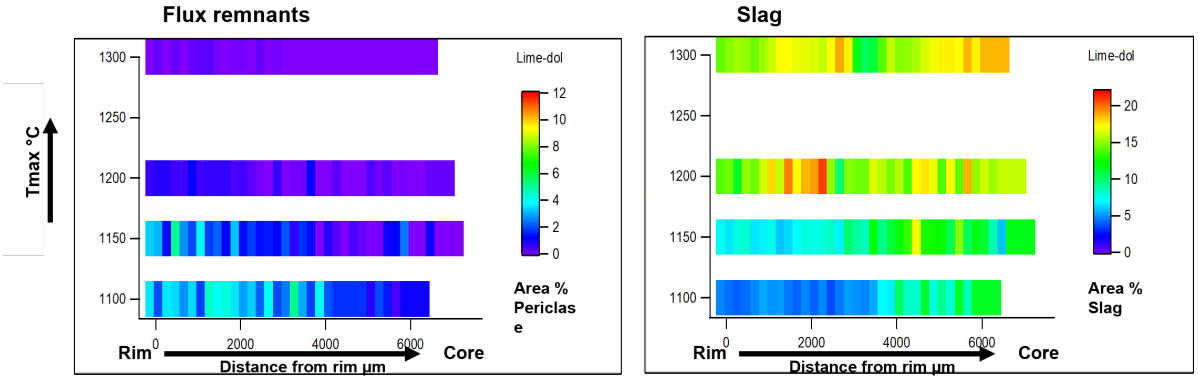

Figure 2.10: Amount of slag and flux remnants from the shell to the pellet's core at different firing temperatures (Small & Firth, 2023).

2.3. Vanadium

2.3.1. Vanadium in pellet feed

V occurs in minerals, melts and oxides as 2+, 3+, 4+, and 5+ and is typically present in minerals as an accessory component. It substitutes for Fe in minerals and, therefore, is more abundant in mafic rocks than in felsic (Huang et al., 2015; Sutton et al., 2005). In magnetite, V mainly occurs as V^{3+}, with minor traces of V^{4+} in the spinel structure of the magnetite (Balan et al., 2006). This is because V^{3+} can substitute for Fe^{3+} (Huang et al., 2015). V^{3+} is insoluble in water, so it is stable in the magnetite structure and can only be soluble when the valence state V is converted to V^{5+}, which requires high temperatures (R. Li et al., 2018; Zhang et al., 2021).

The oxidation V rich magnetite results in V a hematite phase. This process is described by Chen et al. (2021), who reviewed the oxidation of V iron spinel (Fe_2VO_4). Between 300 and 400 °C, the spinel structure starts to be destroyed because of the oxidation Fe^{2+}, while the V remains in V^{3+} valance state, as shown in equation 2.4. Between 400 and 600 °C, this destruction of spinel structure into hematite and $6V_2O_3$ is completed, and the V starts to oxidise into VO_2, as shown in equation 2.5. As the temperature increases between 600 and 1000 °C, the V oxidises further to V_2O_5, as shown in equation 2.6. With the V in valance state V^{5+}, the V can react with the hematite, as shown in equation 2.7.

$$12Fe_2VO_4 + 3O_2 = 6V_2O_3 + 12Fe_2O_3 \tag{2.4}$$

$$2V_2O_3 + O_2 = 4VO_2 \tag{2.5}$$

$$4VO_2 + O_2 = 2V_2O_5 \tag{2.6}$$

$$V_2O_5 + Fe_2O_3 = 2FeVO_4 \tag{2.7}$$

Because V substitutes for Fe, concentrations of V will be higher in mafic than in felsic rocks (Huang et al., 2015). The presence and concentration of V in iron deposits can, therefore, vary widely based on

geological factors, but this is not the only contribution factor — for example, deposition by hydrothermal fluids, secondary enrichment, or weathering. Therefore, substituting V for Fe is not the only reason for the variability of V concentration in iron deposits. For example, BIF deposits usually contain low concentrations of V. If these formations metamorphose, they form magnetite ores, which could increase the trace elements like V by ten times the original concentration (Lan et al., 2019).

So V can be expected in iron ores, depending on the origin of the ore. Other input materials can also contain V. Olivine occurs in mafic and ultramafic rocks and contains Fe, which can be substituted for V. In clays, like bentonite, V can substitute for Al^{3+} (Huang et al., 2015). Limestone and dolomite are carbonated sedimentary rocks. A study by Sharma (1979) has shown that carbonated rocks contain V, but in the case of the Rothan formation, these concentrations are lower than 50 ppm. Huang et al. (2015) describes that V is present in fossil fuels like coal, but the concentration in coal is typically less than 100 ppm. So bentonite and olivine could contain elevated V concentrations. Still, these are used in much smaller quantities than the iron ores and, therefore, are insignificant in the overall V concentration in pellets.

2.3.2. Vanadium partition

In Subsection 2.3.1, it is discussed that V is present as a trace element in iron oxides. At induration, melt phases are created in which V finds a new equilibrium between the melt and the mineral. In the literature, two parameters that influence this partition are the fO_2 and the basicity of the melt phase.

In Section 2.2.5, it is already discussed that the fO_2 influences the secondary phases that are formed during induration. In addition, current research also shows that fO_2 could also influence the partitioning of V between the mineral and melt phases (Karner et al., 2006; Mallmann & O'Neill, 2009; Righter et al., 2006; Righter et al., 2011; Shearer, McKay, et al., 2006; Shearer, Papike, et al., 2006). This is because the oxygen fugacity controls the valence state of V in both melts and crystals, and the

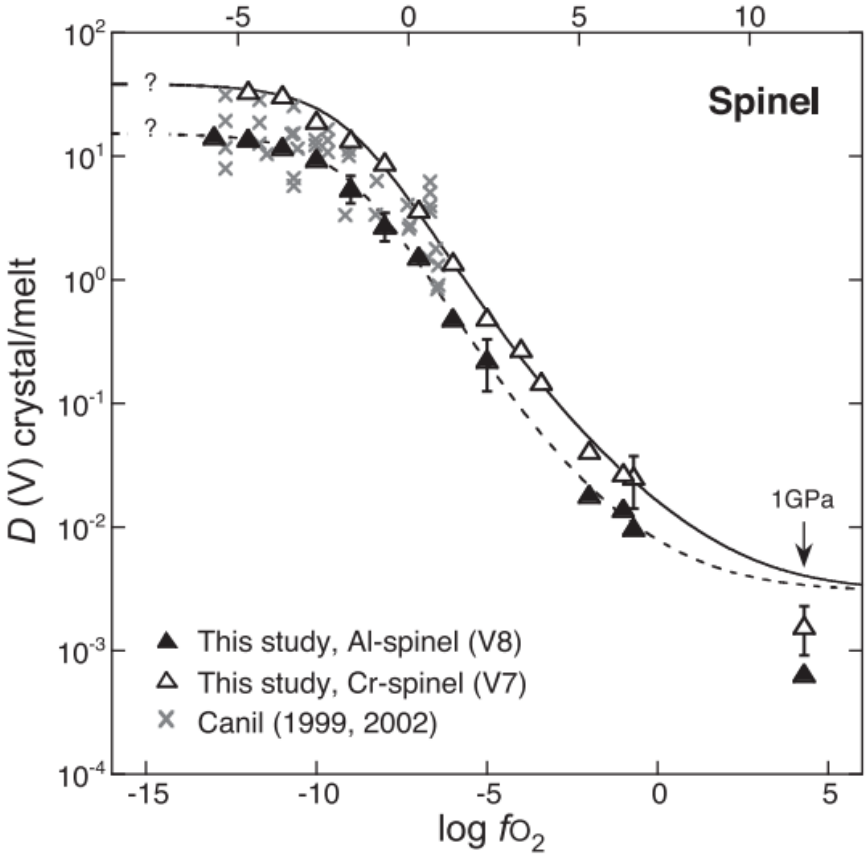

Figure 2.11: Partition coefficients obtained for V between Al and Cr spinel relative to silicate melt as a function of fO_2. All data were obtained at 1 atm and 1300 °C, except for the last measurement (Canil, 1999; Mallmann & O'Neill, 2009).

valence state determines if V can be substituted for Fe in the mineral. The partitioning ratio between the mineral and melt phase is expressed in equation (2.8). Figure 2.11 shows the $D_V^{mineral/melt}$ graph in relation to fO_2 for a spinel.

$$D_V^{mineral/melt} = \frac{wt\%Vmineral}{wt\%Vmelt} \tag{2.8}$$

Bergman (1988) showed in his paper that there is a relation between the optical basicity (Λ) and the V capacity($C_{VO_4^{3-}}$) of the melt. With V present as a trace metal in the crystal and assuming V in the slag present as VO_4^{3-}, the vanadate capacity is derived from equation 2.9. The vanadate capacity is shown in equation 2.10. So, this measures how much V in a crystal will end up in the melt phase.

$$[V] + \frac{5}{2}[O] + \frac{3}{2}(O^{2-}) \rightleftharpoons (VO_4^{3-}) \tag{2.9}$$

$$C_{VO_4^{3-}} = \frac{(\%VO_4^{3-})}{[\%V][\%O]^{\frac{5}{2}}} \tag{2.10}$$

Optical basicity is a measurement of the electron donor power of the oxygen present in glasses or melt, and so is a scale of the acidity/basicity of materials. The theoretical optical basicity can be calculated with equation 2.11

$$\Lambda = X_a\Lambda_a + X_b\Lambda_b + \ldots + X_n\Lambda_n \tag{2.11}$$

where,
Λ_a, Λ_b: Theoretical optical basicity values of the oxides
X_a, X_b: The equivalent cation fractions

The relation between the capacity $C_{VO_4^{3-}}$ and the optical basicity is given in equation 2.12 and Figure 2.12. Although the figure shows data of the capacity V at 1600 °, which is not representative for pellets, the figure shows the relation between the optical basicity and the V capacity. For iron pellets, this implies that the higher the B_2 of the pellet is by using more Ca sources, the higher the optical basicity of the melt phase, so the more V will partition in this melt phase.

$$\log C_{VO_4^{3-}} = 14.92\Lambda - 4.26 \text{ (1600°C)} \tag{2.12}$$

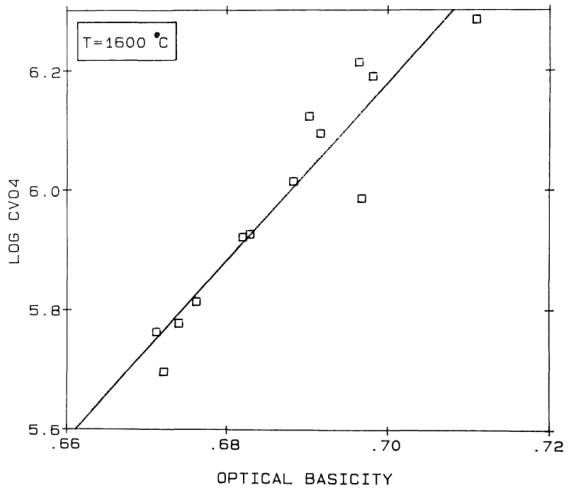

Figure 2.12: The relation between log$C_{VO_4^{3-}}$ and the optical basicity at 1600°C (Bergman, 1988; Selin, 1990).

2.3.3. Vanadium in slags

Heavy metals, like V and Cr, in BF and steel slags have extensively been researched because these slags are used in building products. In these papers, the main host phase responsible for leaching V is dicalcium silicate (Hobson et al., 2017; Kaja et al., 2021; Zomeren et al., 2011). Zhao et al. (2018) describes in their paper that Cr is also hosted in glass, spinel and periclase structures in stainless steel slags. It is helpful to see the mechanisms of Cr because it has a similar electronic configuration and almost the same size, so they have a companionable mechanism. The periclase phase is only formed at a high B_2, which was, in this case, 2.0, but a paper written by Guo et al. (2021) shows that if the B_2 exceeds 1.0 the reduction, swelling and strength properties reduces rapidly, so it is unlikely to find pellets with a B_2 higher than 2.0.

It has been shown that V is also rich in the dicalcium ferrite phase besides dicalcium silicate. There is a low abundance of iron oxides in the slag; therefore, dicalcium ferrite is stable in the slag. This phase is less soluble and, therefore, not considered a main contributor to the leaching of V (Zinngrebe & van der Laan, 2014).

2.4. Sensor technologies in material processing and analysis

2.4.1. XRD

The XRD analysis is used to distinguish minerals based on their crystal structure and their chemistry. Mineral and phase identification is obtained by comparing the measured diffraction patterns to a database of known patterns. The experimental XRD pattern is refined with a Rietveld analysis, which compares experimental patterns with the theoretical pattern calculated from the crystal structures for structure refinement of unknown phases and to quantify phases and minerals. The Rietveld method also enables the calculation of the sample's amorphous content using internal standard material. Although the XRD, in combination with the Rietveld refinement, is a fast and reliable quantification technique, it has its limits. Minerals with a preferred orientation can artificially enhance diffraction peaks. This makes it unreliable for minerals like micas. Also, microabortion affects the accuracy of the results when dealing with samples with varying densities. The last limitation is a relatively high detection limit. Due to poor peak-to-background ratios, XRD has problems detecting phases with an abundance of less than 1 wt% (de Villiers & Lu, 2022; Scarlett & Madsen, 2018).

2.4.2. SEM-EDS

The SEM-EDS is used to examine a sample's structure and chemical composition. Compared to the optical microscope, the SEM generates high-resolution backscatter electron images, which have a greater focus, magnification and higher resolution (Poojari et al., 2023). The EDS equipment is often attached to the SEM and allows quantitative chemical composition analysis. This EDS detects the characteristic X-rays that are released after relaxation of inner shell ionisation caused by the SEM (Exner & Weinbruc, 2004). In a paper written by Schollbach and Laan (2021) they performed a Monte Carlo simulation on the penetration path of the electrons. This showed that atoms in tobermorite with a density of 2.4 g/cm^3 in a radius of 1 μm still generate characteristic X-rays at an acceleration voltage of 15 KeV of the SEM. This could influence the chemical composition of a phase when measuring close to a border of two phases or in a shallow phase. Lowering the acceleration voltage of the SEM will significantly improve the resolution and decrease the efficiency, especially for heavier elements, resulting in longer counting times.

There are limitations to using SEM-EDS. The first limitation is that light elements are difficult to measure because they suffer from absorption from other elements in addition to energy overlap with the L lines of Ti and Cu. This is for elements with an K_α < 0.9 keV, like for C and O. The second limitation is the resolution. If a phase size is smaller than the interaction volume of the beam, this will not be detected as an individual phase (Schollbach & Laan, 2021).

2.4.3. PARC

To further analyse SEM-EDS data, TSN developed in-house software, called PhAse Recognition and Characterization (PARC), to classify phases on scanned maps automatically. van Hoek et al. (2016) has written a paper describing the software. The input for the software is a Spectral Image (SI) data set, where each pixel stores the full EDS spectrum, which can be combined with the greyscale values of backscatter electron images. All the individual pixels are evaluated, and if peaks in the EDS spec-

tra surpass a user-defined threshold, elements are assigned to that particular pixel. All identical peak combinations are then grouped as individual phases. The model can be refined by merging different groups or separating similar phases in a group with different elemental ratios, using histograms, mathematical expressions or density plots, as demonstrated in Figure 2.13. The software can batch-process the model on multiple SI datasets, enabling the visualisation of microstructures and quantifying phases on large areas.

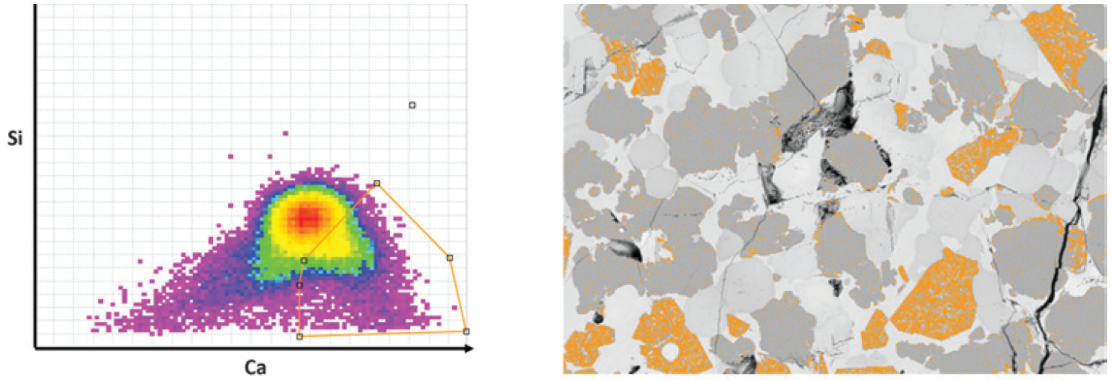

(a) (b)

Figure 2.13: The use of density plot to group phases in PARC, with (a) a density plot of Si and Ca for Ca-rich group of pixels only. Polygon selection of pixels tuned to correspond with backscatter electron image in Figure 2.13b, and (b) a backscatter electron image with selected pixels from density plot in highlighted orange. Image width = 512 μm (van Hoek et al., 2016).

2.4.4. LA-ICP-MS

Laser Ablation Inductively Coupled Plasma Mass Spectrometry (LA-ICP-MS) is the preferred method for analysing trace elements in solid samples. Therefore, it is often used in geology, material sciences, and quality control in the industry. In the ablation cell, the sample and calibration materials are placed on which the laser is focused, typically with a diameter of 10 to 100 μm. The high-energy laser beam ejects particles from the sample, forming an aerosol. The aerosol is transported by a carrier gas, usually argon or helium, into the ICP plasma. Here, the aerosol particles are evaporated, converted to atoms and ionised. The ion beam is extracted in the mass spectrometer interface where the ions are filtered based on their mass-to-charge ratio and then focussed on the detector(Vogt & Latkoczy, 2005). The most common mass filters are quadrupole, magnetic sector field or time-of-flight (TOF) filters. The advantage of the TOF over the quadrupole is that it analyses all the isotopes simultaneously, while the quadrupole can only do one (Fricker & Günther, 2016).

The advantage of the LA-ICP-MS is its very low detection limits, but it also has shortcomings. Fractionation is a complex process that occurs during aerosol formation, transportation of the aerosol and the reaction in the ICP and is not yet fully understood (Miliszkiewicz et al., 2015). Therefore, the LA-ICP-MS should be calibrated every time it is used. External standards are used to interpolate signal intensities between two known standards. Instrumental drifts, laser ablation yields and matrix effects of the sample and external standard are corrected using an internal standard where the concentrations of a major element should be known in advance for the sample and external standards (Longerich et al., 1996).

2.5. Key outcomes

The literature review already outlines the reactions of the major phases that will occur during the induration process of the pellets. Secondary phases are formed, like oxidising and reduced iron oxides, melt and magnesium ferrite. Important firing parameters on the number of secondary phases are the temperature and the amount of O_2 present in the environment. However, it has not been shown how trace elements, like V, relate to these phase changes. A lot of research has been performed on how to process iron ores, pellets and BF slags to recover V, see Section 6.5, which is more a principle of trying some leaching methods and see what the efficiency is, instead of more in-depth research about the chemistry of the phases where it is leached from.

Depending on the origin of the iron ores, these can contain V as a trace element. This is mostly for magnetite iron oxide. Hematite can also contain V, but in much lower concentrations. Also, bentonite and olivine could contain some V. Still, these are used in smaller quantities in the pellet blend and, therefore, don't significantly contribute to the pellet's overall concentration of V.

It has been shown that V is present in BF and steel slags. These slags are used in building products but tend to leach V. A similar trace element Cr has been detected in the glass, periclase and spinel structure in a stainless steel slag. For this research, this already indicates that V is transferred partially from the magnetite structure to the secondary melt phase.

Possible important parameters determining how much V could partition in the melt are the fO_2, which is a measure for how much O_2 is present in the environment during firing and the optical basicity of the melt phase, which is dependent on the B_2 of the pellet.

3

Materials

This chapter describes the materials analysed for this research. First, some geological context is given to the iron oxides used as the most important input material. Then, an overview of all the input materials used is given. Finally, the pellets that have been produced for this research are discussed.

3.1. Iron Oxide-Apatite ores

The iron ores used to produce pellets for this research originate from Iron Oxide-Apatite (IOA) deposits, also referred to as Kiruna-type or magnetite-apatite deposits. The IOA deposits are distributed worldwide, as is shown in Figure 3.1, but the largest deposits are found in Sweden, Iran, Peru and Chile (Reich et al., 2022). The deposits are an important source of Fe but also have other interesting byproducts like P and REEs (Palma et al., 2021).

Magnetite is the main mineral in IOA deposits, with varying amounts of apatite. Possible gangue minerals are pyrite, biotite, actinolite, pyroxene, scapolite, chlorite, titanite, calcite and quartz (Reich et al., 2022).

In the past, there has been extensive debate about IOA being formed by magmatic or hydrothermal processes, but IOA deposits are highly complex systems that cover the entire igneous-hydrothermal spectrum, namely from being purely magmatic to magmatic-hydrothermal and exclusively hydrothermal (Reich et al., 2022). The result is that each orebody has its characteristics and can comprise massive tabular magnetite, lenses, veins, stockworks, breccias, and stratabound bodies (Foerster & Jafarzadeh, 1994; Frietsch & Perdahl, 1995; Nystroem & Henriquez, 1994). The age of the deposits varies between Paleoproterozoic and Plio-Pleistocene (Frietsch & Perdahl, 1995).

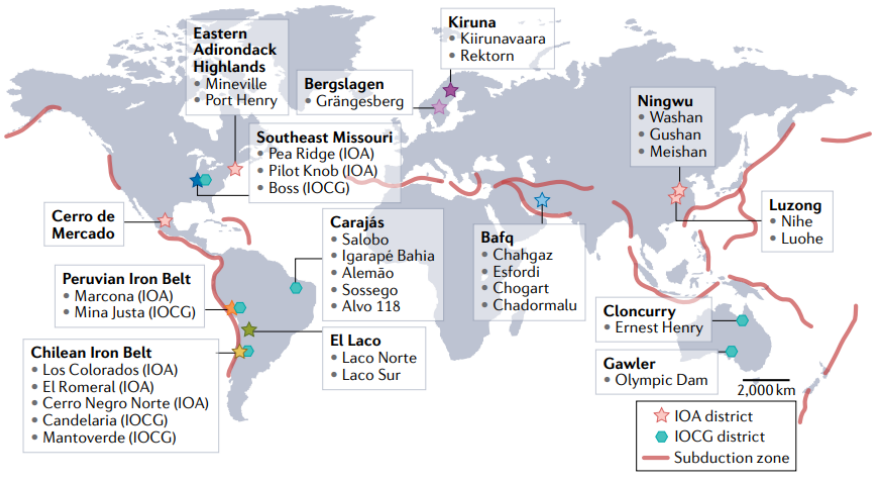

Figure 3.1: Location IOA deposits worldwide (Reich et al., 2022).

3.2. Input materials

For this research, two different pellets are produced, with variations in the B_2, and one pellet is used that has been produced by a third party, who used the same iron oxide, but the rest of the composition is unknown. The blends for the first two pellets are shown in Table 3.1. Note that, other than explained in Subsection 2.2.3, no coke breeze has been used to produce these pellets. The input materials are shown in Figure 3.2.

Table 3.1: Blend of different pellets.

Number	Description	IOA ore	Limestone	Olivine	Bentonite
		wt%			
5171	High V & low B_2	98.31	0.42	0.82	0.45
5177	High V & high B_2	97.12	1.62	0.81	0.45

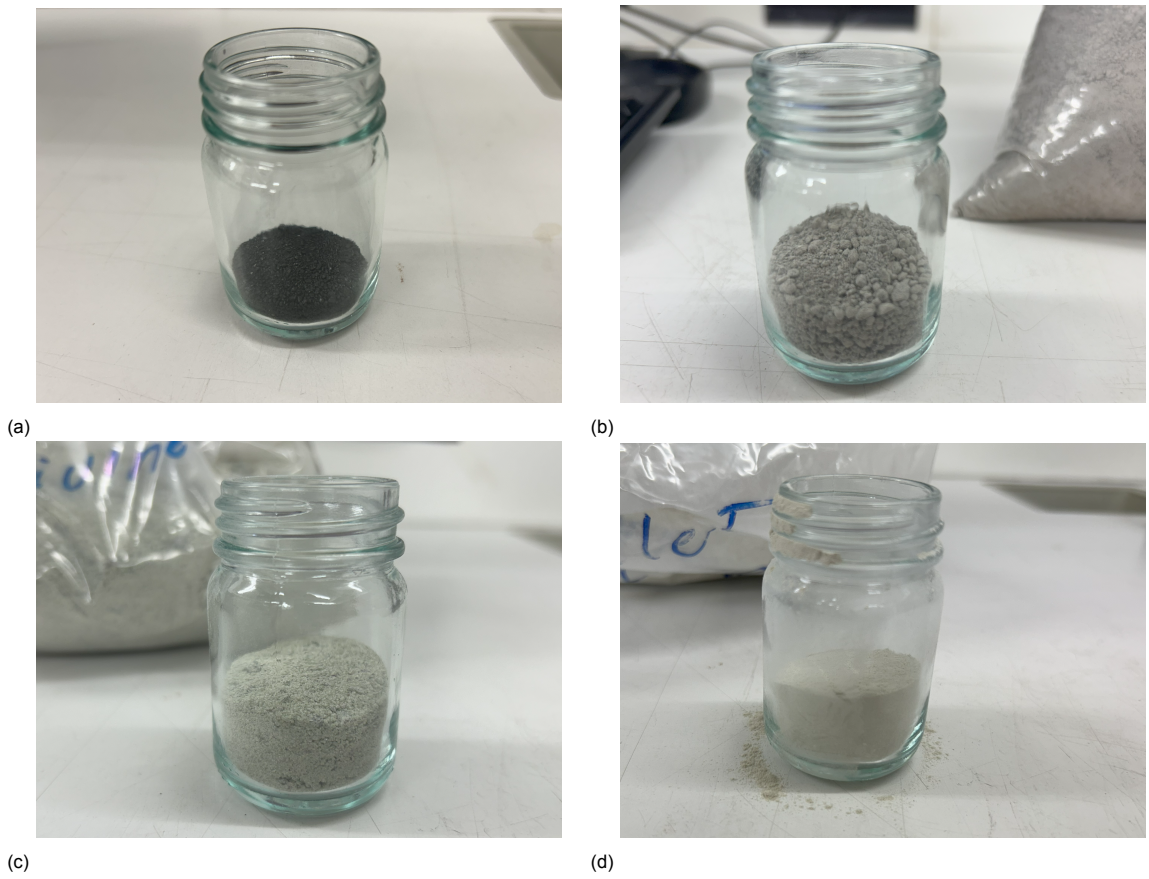

(a) (b) (c) (d)

Figure 3.2: Samples of various materials: (a) IOA ore sample, (b) limestone sample, (c) olivine sample, and (d) bentonite sample.

The analytical department of TSN has measured the chemical composition of the input materials, using X-ray fluorescence (XRF). The results of the IOA iron ore, olivine, limestone and bentonite samples are shown in respectively Table 3.2, 3.3, 3.4 and 3.5. What stands out is that only in the IOA ores V is detected.

Table 3.2: Chemical composition of IOA ores with XRF (wt%).

Al_2O_3	CaO	Fe	FeO	GOI	LOI	MgO	MnO	P_2O_5	SiO_2	TiO_2	V indicative	Zn
0.29	0.29	70.1	29.89	3		0.42	0.064	0.084	0.95	0.38	0.14	0.002

Table 3.3: Chemical composition of olivine using XRF (wt%).

Al_2O_3	CaO	Fe	FeO	GOI	LOI	MgO	MnO	P_2O_5	SiO_2	TiO_2	Na_2O
0.51	0.55	0	0		0	48.2	0.095	0.003	41.5	0.008	0.10

Table 3.4: Chemical composition of limestone using XRF (wt%).

Al_2O_3	CaO	Fe	FeO	GOI	LOI	MgO	MnO	P_2O_5	SiO_2	TiO_2
0.30	53	0.20	0		42.7	0.90	0.013	0.008	2.76	0.02

Table 3.5: Chemical composition of bentonite using XRF (wt%).

Al_2O_3	CaO	Fe	FeO	GOI	LOI	MgO	MnO	P_2O_5	SiO_2	TiO_2	Na_2O	K_2O	ZrO_2
15.7	3.23	0.71	2.95		7	2.9	0.06	0.10	62.6	0.43	2.7	0.71	0.02

3.3. Fabrication of pellets

The pellets are made by the department Proeffabriek Ijzermaken. They make small batches of feed material used for research purposes. The pellets are made similarly to those fired for mass production as described in paragraph 2.2.2 but on a smaller scale. The pellets are fired in a single pot, where hot air can be directed from top to bottom or in the opposite direction. The hot air is also reused, as is done in the industrial pellet plant. In the pot, multiple thermocouples are installed to measure the temperature at different zones in the pellet bed.
The thermocouples and their corresponding zone in the pellet bed:

- T1: Top
- T2: Upper
- T3: Middle
- T4: Bottom
- T5: Ash
- T6: Pan

Note that in zones T5 and T6, no pellets are present. Figure 3.4, shows the thermocouple profiles of pellet 5177 in the different zones. The temperature at T1 is not always reliable as it can sometimes get uncovered as the pellet bed shrinks during firing, leading to a lower reading than expected. The profiles show that the maximum temperature in zones T3 and T4 is higher than in T1 and T2, but the induration time is significantly shorter.

The pellets produced for this thesis are shown in Figure 3.3. The analytical department of Tata Steel has also measured the chemical composition of the fired pellets used in this research. The results are shown in Table 3.6. The table shows that the V content is indicative; this does not mean that the V content is not measured, but only that the XRF is not calibrated for V.

Table 3.6: Chemical composition of used pellets.

Pellet	Al2O3	CaO	Fe	FeO	GLT1000	GLV1000	MgO	MnO	P2O5	SiO2	TiO2	V indicative	Zn	B2
							wt%							
5171	0.36	0.48	67.28	0.98	0.04	0.01	0.79	0.07	0.05	1.42	0.34	0.13	0.00	0.34
5177	0.37	1.20	66.78	0.76	0.04	0.01	0.80	0.06	0.05	1.42	0.34	0.13	0.00	0.85

Figure 3.3: Fired pellets with IOA ores, produced for this research.

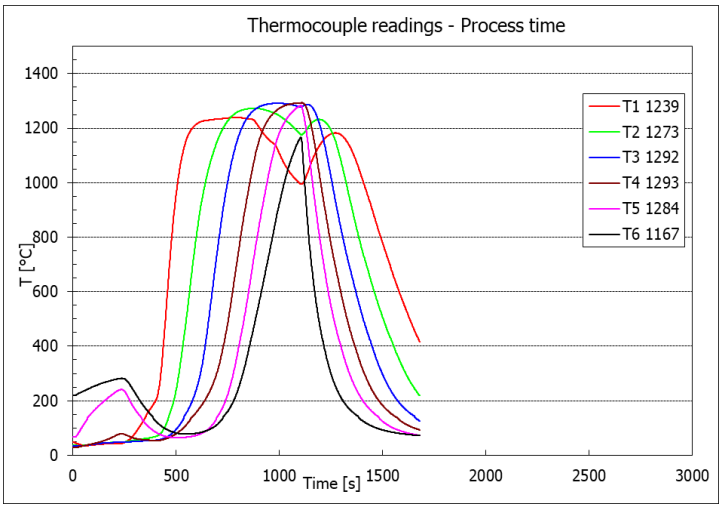

Figure 3.4: Thermocouple profile of pellet 5177.

3.4. Pellet fabricated by third party

One batch of pellets that a third party has produced is used. To prevent discord between companies, the product name can not be given. For this thesis, this pellet will be named pellet 9999. Also, the blend used to produce this pellet is unknown, and no XRF data is available. What is known of this pellet is that it uses the same IOA iron ore as the other pellets. Compared to the other pellet, this pellet is produced in mass production and, therefore, in a less controlled environment. Therefore, it might contain more severe underfired pellets, and it is impossible to trace back in which zone of the pellet bed the pellet is fired. The purpose of using this pellet is to check if the same phases occur as in the pellets produced by TSN.

4

Methods

This chapter describes the methods applied to the results. First, the analytical instruments are described, together with the measurement workflow. Then, a description of how data sets are processed using the in-house-built software PARC will be provided to classify phases on scanned maps. Finally, the process of the leaching tests performed by a third party are discussed.

4.1. Analytical techniques

Different methods are used to characterise the pellets and their ingredients. There has been a workflow for the embedded samples because each of these techniques requires its preparations or is a destructive technique, which makes it undesirable or impossible to change the order of analysis. The analysis with the XRD does not require embedded samples, so it can be done separately through the other analysis.

The starting point of the workflow is analysing all the samples with the microscope. However, before using the microscope, the samples need to be prepared. These are mounted in an epoxy resin. Typically, six pellets would fit in one mount when mounting the pellets. After the epoxy is hardened, the sample is cut in half and polished to expose the materials. Normal samples, like the input materials and the leached pellets, are first polished with silicon carbide paper and water, then polished with a diamond paste up to 0.1 μm grit. The embedded pellets are polished using an alcohol-based suspension instead of water because V and Ca might leach otherwise, so the sample would not be representative. An example of a sample with embedded pellets is shown in Figure 4.1

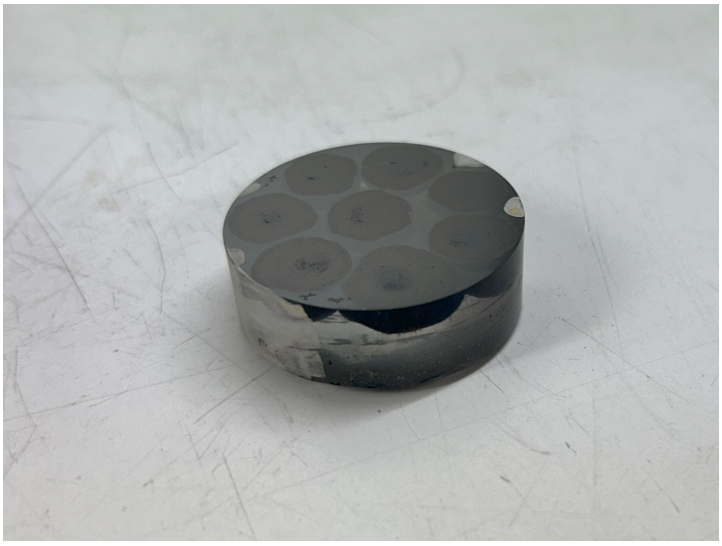

Figure 4.1: Six embedded pellets in epoxy resign.

After the sample is analysed with the microscope, it is analysed with the SEM-EDS. Before use, the embedded samples are carbon-coated to increase the signal/noise ratio and reduce the thermal damage of the electron beam. This is done using the Brandley approach, which is a thermal evaporation method. A current is going through two carbon rods, and at a sharpened contact point, high temperatures are generated, which evaporate the surface. This is done in a vacuum, which allows the carbon rod to evaporate quickly into a monoatomic state.

The LA-ICP-MS is a destructive technique, so it is the final stage of the workflow. Only one pellet has been analysed using this technique. Because the laser ablates the surface of the sample, the carbon coating required for the SEM-EDS must be removed before; otherwise, the carbon coating interferes with the results. This is done by polishing the sample again.

4.1.1. Optical microscopy

The microscope is used to define the regions of interest in the samples and get a first impression of some of the characteristics of the sample. The microscope is used on the pellets to see what pellets are fully oxidised, if there are a lot of gangue materials and if the iron oxides sintered well. This creates an optical map from which a first impression is obtained about the characteristics of the material. For the pellets, this means that it is immediately clear what kind of conditions the pellets are fired in, namely if the temperature is high enough and under what reduced environment. This is shown by the amount of sintering and if the core contains hematite or magnetite iron oxides. From this, a selection can be made of what areas in the sample are worth investigating, which is necessary because of the time other analytical instruments require and the amount of data gathered. A Zeiss Axio Imager Z1 is used for optical microscopy, which is displayed in Figure 4.2. The objectives on the microscope vary from 2.5x to 50x. For this thesis, only the polarised reflective light reflector is used. The accompanying software is Zeiss Zen Core, which is used to process the images. The optical microscope can create a mosaic of different images automatically stitched together to make one image. Initially, the entire sample is mapped with an objective of 5x. The interesting areas are then mapped with an objective of 20x.

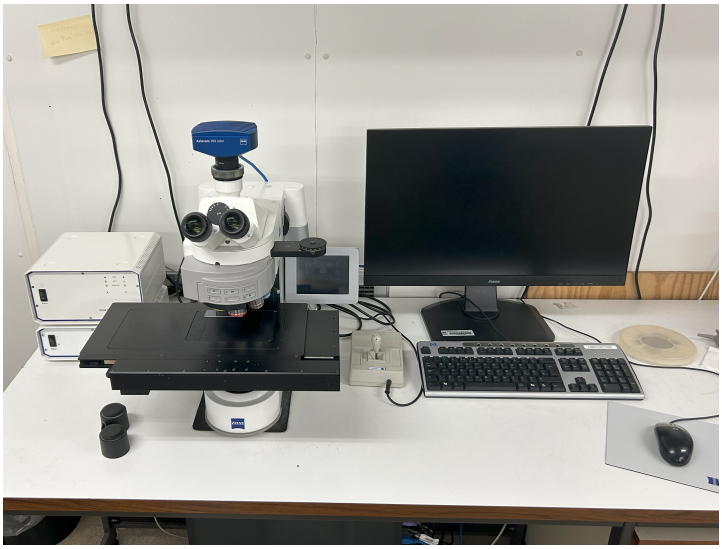

Figure 4.2: The optical microscope used to analyse the structures of the samples is this Zeiss Axio Imager Z1.

4.1.2. XRD

The XRD technique was used to identify the samples' bulk phases and proportions. Quantitative determination of the phase proportions was carried out through Rietveld analysis. The XRD patterns were obtained using a Bruker D8 Endeavour diffractometer, which is fully automated and equipped with a position-sensitive detector. This XRD is displayed in Figure 4.3. Topas software is used to analyse the data. The XRD is used in two ways: for a powder diffraction analysis and point measurements. The patterns are recorded in a range of 10 to 130 °(2 θ), with a step size of 0.02 °, and time per step off 200 s in reflection mode.

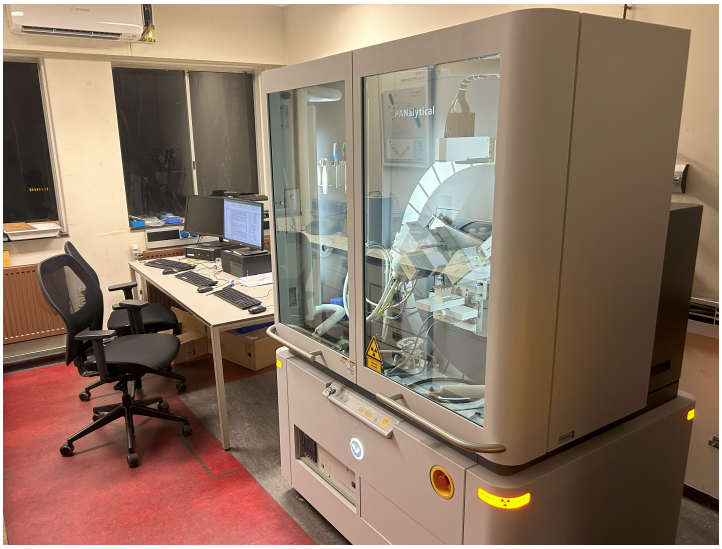

Figure 4.3: The XRD used to measure the bulk phases and proportions of the samples is this Bruker D8 Endeavour diffractometer.

The powder diffraction analysis has analysed all the input materials and pellets. To prepare the sample, the material is first ground to powder. Because amorphous phases do not refract in an organised pattern, the amorphous content can not be detected, and therefore, a silicon standard is added to the sample. The amorphous content can be calculated because it is known how much of this standard is used. The outcomes are analysed using the Rietveld refinement. Note that the detection limit of the XRD is about 0.5 wt%.

A pinhole traverse with the XRD is conducted using point measurement. Figure 4.4 shows the eight locations measured along the traverse. This is done to identify if the melt phases would refract. This will tell if the melt has a glass or crystal structure.

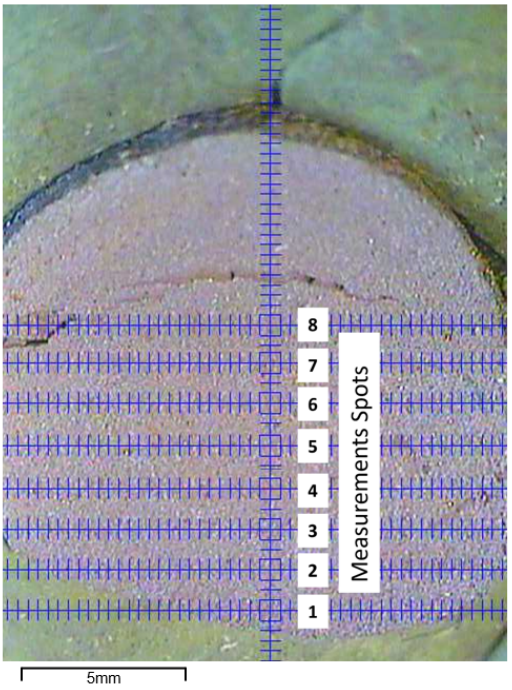

Figure 4.4: XRD pinhole traverse of pellet 5177-1 with point analyses.

4.1.3. SEM-EDS

For this thesis, two SEM instruments are used: one Jeol 5900LV, which is used for point analysis, and one Jeol 7001F, which is used for mapping an area and point analysis. The accompanying software is Thermo Scientific Pathfinder for the Jeol 5900LV and Oxford Aztec for the JEOL 7001F.

The Jeol 5900LV, is displayed in Figure 4.5. This SEM is equipped with a Thermo-Fischer Scientific microanalysis system with one Silicon Drift Detector (SDD). The equipment is typically used with an accelerating voltage of 15 kV, but sometimes it is needed to increase the voltage to distinguish elements with close k_α peaks. The working distance is set to 10 mm.

Figure 4.5: The SEM-EDS used for point analysis is this JEOL 5900LV.

The Jeol 7001F is displayed in Figure 4.6. This SEM has two large-angle SDD detectors. The accelerating voltage is set at 15 kV, and the working distance is 11.5 mm. The working distance differs from what is normally considered optimal, but this is done to improve the EDS count rate from the two SDD detectors.

Figure 4.6: The SEM-EDS used for point analysis and scanning tiles is this JEOL 7001F.

The SEM-EDS is used for phase classification and quantifying the chemical composition of different phases in the pellets. In addition, the backscatter detector produces very sharp images, but only in a greyscale. All samples are analysed with this equipment. Before use, the embedded samples are

carbon-coated to increase the signal/noise ratio and reduce the thermal damage of the electron beam. In addition, copper strips or silver paint are applied to the sides of the samples for the same purpose.

Point measurements are carried out with the SEM-EDS to identify phases and quantify their chemical composition. Based on the required accuracy, a counting live time of 3 to 5 seconds is used. The accelerating voltage is set at 15 kV and a current of 25 nA. The working distance is 11.5 mm.

The SEM-EDS is also used to map the distribution of different elements in the pellet. The SEM-EDS maps complete tiles along the pinhole traverse from the rim to the pellet's core. Based on the size of the pellets, 50 to 69 tiles are used to complete one pinhole traverse. The settings that are used are the same as from the point analysis. The maps are measured with a magnification of 1000x and have a 512 by 512 pixels resolution. The frame count is set at four, meaning each tile is scanned four times to increase the data quality. Besides the maps of element distributions, the data of these maps is further analysed in PARC, as will be explained in 4.2

4.1.4. LA-ICP-MS

The LA-ICP-MS is equipped with a Teledyne Irida laser and a ThermoFischer iCAP RQ ICP-MS. The mass analyser uses a quadrupole technique that measures the individual elements sequentially.

The LA-ICP-MS is used to validate the results from the SEM-EDS. In the SEM-EDS, artefacts can occur; for example, the K_α peaks of Ca + Mg cause an artefact in the V spectra. Three areas are mapped in one pellet: one in the core, mantle and rim. A pixel size of 5 μm is used. As explained in Subsection 2.4.4, this technique needs to be calibrated before use. The standards used for these measurements are shown in Table 4.1.

Table 4.1: Used standards with certified concentrations of $Fe, Na, Mg, Al, Si, Ca, V, Cr$ and Mn for LA-ICP-MS analysis.

Certified standard	Fe ppm	Na ppm	Mg ppm	Al ppm	Si ppm	Ca ppm	V ppm	Cr ppm	Mn ppm
Nist 612	51.0	101633.8	68.0	10743.3	337017.0	85048.5	38.8	36.4	38.7
Nist 610	458.0	99408.2	432.0	10319.9	325792.5	81475.0	450.0	408.0	444.0
BHVO-2G	87836.5	17804.5	42995.8	71974.9	230438.6	81475.0	308.0	293.0	1316.6
BIR-1G	80840.6	13724.3	56684.5	82030.2	222029.3	95037.3	326.0	392.0	1471.5
St H 6-80	33968.6	32938.2	11879.6	94202.4	297752.9	37735.8	90.3	16.9	588.6

4.2. PARC

PARC is used to analyse further the pinhole traverse data generated with the SEM-EDS. The goal is to quantify the phase abundances in the pellets along the traverse. PARC is a non-standard software tool whose fundamentals are explained in Subsection 2.4.3. PARC classifies the EDS spectral data for each pixel of an image field and groups these pixels based on the occurrence of the peaks in the spectra. The user can define thresholds, for example, for the intensity of the peak. The lower boundary of the spectrum is cut off at typically 0.9 kV. Different groups can be merged, or, based on density plots of spectral counts, new groups can be created. This way, a model can automatically identify all different phases in a random tile.

The SEM-EDS measures a series of individual tiles the pinhole traverse. The PARC model classifies all the different phases in these individual tiles. An example of a tile is shown in Figure 4.7, where Figure 4.7a shows the different phases in different colours, which can be compared to the SEM backscatter image in Figure 4.7b and Figure 4.7c shows the legends and the area % of different phases. The net area % in Figure 4.7c does exclude the categories unclassified, empty spectra and embedding, but this model also has a label epoxy, which also should be excluded. Besides the epoxy, the model can classify the melt phase, iron oxide and magnesium ferrite, which are the most important categories. In addition, it can classify primary minerals like olivine, apatite, and ilmenite. Some phases are difficult to classify as one of the before-mentioned phases because of very small abundances or because the pixel is on the boundary between two phases. So, the EDS received signals from both phases. Therefore, the results are checked afterwards to see if the amount of falsely classified pixels is acceptable. If needed, the model can be updated for one specific tile to be optimised and run again to minimise the error.

All individual tiles along the traverse are analysed this way. The maps that show the different phases, as in Figure 4.7a are finally stitched together to create one image. Also, the calculated phase

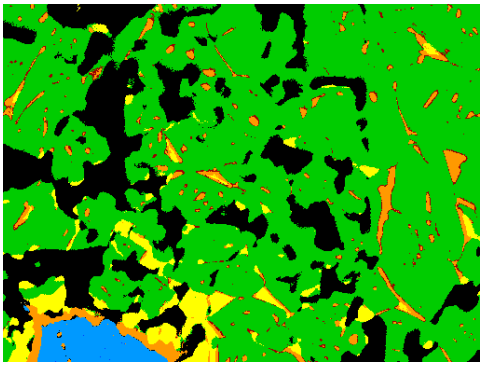

(a)

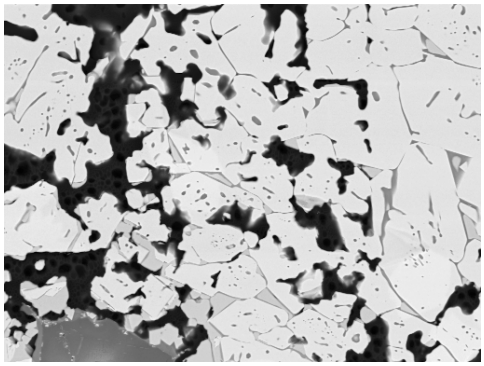

(b)

id	color	show	grain	p1	p2	p3	p4	p5	p6	p7	p8	area	net area	area %	net area %	label	spectr...
0		✔	✔									0		0.00		unclassified	
1		✔	✔									23634		12.02		empty spectra	1.00
2		✔	✔									0		0.00		embedding	1.00
3		✔	✔	Fe-KA1								129061	129061	65.64	74.61	Iron oxide	1.00
4		✔	✔	Mg-KA1	Fe-KA1							9296	9296	4.73	5.37	Magnesium ferrite	1.00
5		✔	✔	Si-KA1	Fe-KA1							3390	3390	1.72	1.96	Transition melt - FeO	1.00
6		✔	✔	Si-KA1	Ca-KA1							8123	8123	4.13	4.70	Melt	1.00
7		✔	✔	Si-KA1	Ca-KA1							4544	4544	2.31	2.63	Olivine	1.00
8		✔	✔	Mg-KA1								4	4	0.00	0.00	MgO	1.00
9		✔	✔	Ca-KA1	Fe-KA1							27	27	0.01	0.02	CaO-FeO	1.00
10		✔	✔	Ca-KA1								0	0	0.00	0.00	CaO	1.00
11		✔	✔	Mg-KA1	Si-KA1	S-KA1						0	0	0.00	0.00	Mg-Si-S	1.00
12		✔	✔									18522	18522	9.42	10.71	Epoxy	1.00
13		✔	✔									0	0	0.00	0.00	Apatite	1.00
14		✔	✔									0	0	0.00	0.00	Magnesium chromite	1.00
15		✔	✔	Fe-KA1								7	7	0.00	0.00	Ilmenite	1.00

(c)

Figure 4.7: PARC result of pellet 5177-3 tile 51, with (a) image of PARC indicating different groups, (b) backscatter image of SEM, and (c) legend and calculated phases abundance in this tile.

abundances per tile along the traverse are plotted in one graph to show if there are trends in the data.

4.3. Leaching test

A third party performed leaching tests in accordance with the standard NEN 7373:2004 to show how much V, Ca, and Si were leached and to determine the influence of the B_2 on the leaching of V.

The NEN 7373 describes a method to leach inorganic substances from granular materials in a column test as a function of the liquid and solid ratio (L/S). In the test, distilled water is poured over the dry material in the following ratios: L/S = 0,1; 0,1; 0,3; 0,5; 1,0; 3,0; 5,0 l/kg dry material. The results are recorded between each step, measuring leached substances in mg per kg of dry material. Before the start of the test, at least 95 wt% of the dry material must have a particle size smaller than 4 mm (NEN, 2004). This means that the pellets need to be crushed and grounded first.

5

Results

This chapter shows all the results from the analysis done in this research. First, all the input materials are characterized. This is done with the SEM-EDS and the XRD. Then, the results of the analysis of the pellets are given. This comprises the analysis of the microstructure, EDS maps, SEM-EDS point analysis, PARC results, XRD analysis and LA-ICP-MS maps. Finally, the results of the leaching tests are given.

5.1. Characterisation input materials

This section classifies all the input materials. It is mainly used as an inventory to determine where certain phases originate from and to show what contains relatively high concentrations of V. The appendix shows all the XRD profiles and the chemical compositions of all the points analyzed.

5.1.1. XRD

This subsection shows the results of the XRD analysis of the input materials. The results have been refined using the Rietveld refinement and the amorphous content is calculated using a silicon standard.

XRD data in Table 5.1 shows that the main oxide in the IOA ore is magnetite and only a small fraction of hematite. It also shows that there is about 3.6 wt% of amorphous material, but this could also be a collection of gangue minerals, whose signals remained below the detection limit of the equipment, which is +/- 0.5 wt%. An overview of the gangue minerals found in this research using the SEM-EDS is shown in Subsection 5.1.2.

The XRD results for the limestone, olivine and bentonite samples are shown in respectively Table 5.2, 5.3, and 5.4. The main component of limestone is calcite ($CaCo_3$), and olivine is forsterite (Mg_2SiO_4). The most abundant crystal phase is montmorillonite ($(Na,Ca)_{0.33}(Al,Mg)_2(Si_4O_{10})(OH)_2 \cdot nH_2O$), but this still less than the amorphous content of 43 wt%.

Table 5.1: XRD measurement IOA ore in compositional wt% with the std.

Phase	**Comp**	σ
Magnetite	96.3	0.15
Hematite	0.3	0.15
Amorphous	3.4	0.8

Table 5.2: XRD measurement limestone in compositional wt% with the std.

Phase	**Comp**	σ
Calcite	91.3	0.35
Graphite	1.8	0.25
Hematite	0.6	0.15
Dolomite	0.8	0.2
Magnetite	0.3	0.1
Corundum grinding	0.0	0.0
Amorphous	5.2	1.05

Table 5.3: XRD measurement olivine in compositional wt% with the std.

Phase	**Comp**	σ
Forsterite	86.1	0.5
Enstatite	8.6	0.35
Lizardite 1T	0.8	0.2
Lizardite 2H2	1.3	0.25
Brucite	0.2	0.15
Talc 1A	3.1	0.25
Corundum grinding	0.0	0.0
Amorphous	0.0	1.5

Table 5.4: XRD measurement bentonite in compositional wt% with the std.

Phase	**Comp**	σ
Cristobalite	2.0	0.45
Cristobalite high	7.6	0.4
Montmorillonite	24.2	0.75
Dolomite	1.9	0.25
Quartz	0.4	0.15
Calcite	2.9	0.2
Sanidine high	10.9	0.7
Enstatite	3.8	0.85
Muscovite	3.1	0.75
Amorphous	43.0	1.75

5.1.2. SEM-EDS JOEL 5900LV

This subsection shows the results of the SEM-EDS with the JOEL 5900LV equipment. Only the IOA ore sample was analysed using this equipment. The sample contains, besides iron oxide grains, quite some gangue material. Figure 5.1 shows two backscatter images of the IOA sample together with the locations of the EDS point analysis, with corresponding Table 5.5 showing the chemical compositions of these analyses. These images contain iron oxide, apatite, biotite, zircon and K-feldspar phases. The XRF results in Section 3.2 show that the IOA ores contain V, and the SEM-EDS results show that this is present in the iron oxides. Besides the gangue material shown in the figures, diopside, ilmenite, quartz, albite, titanite, pyrite, calcite, enstatite, actinolite-tremolite, and hornblende have been detected.

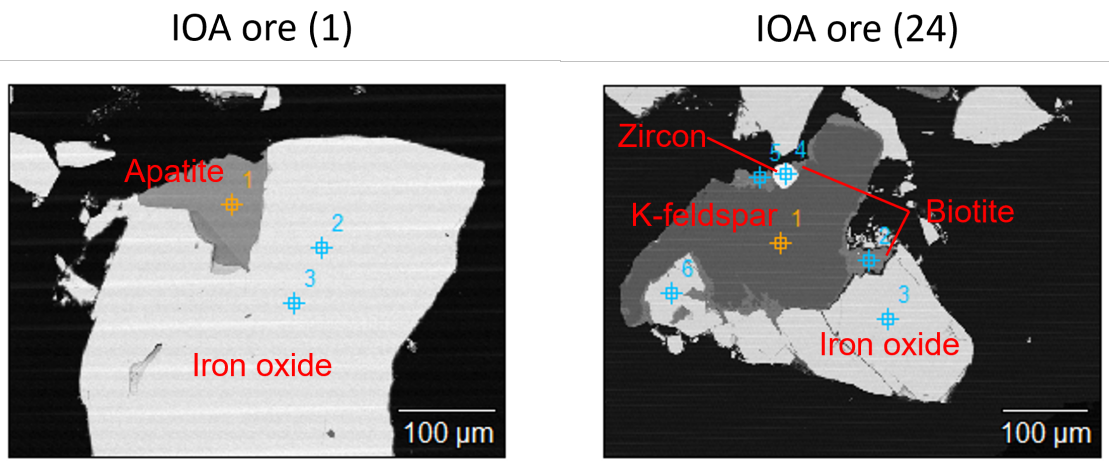

(a) (b)

Figure 5.1: Backscatter image of IOA ore sample using SEM-EDS at (a) area IOA ore(1), and (b) area IOA ore (24).

Table 5.5: SEM point analysis of region 1 and 24 in IOA ore sample corresponding to Figure 5.1 in wt% oxide.

Oxide	**Iron oxide**				**Apatite**	**K-feldspar**	**Biotite**		**Zircon**
F	-	-	-	-	3.43	-	-	-	-
Na_2O	-	-	-	-	-	11.35	-	-	-
MgO	0.35	0.09	-	-	-	-	12.36	12.71	-
Al_2O_3	0.24	0.29	0.17	-	-	20.79	19.58	18.51	-
SiO_2	-	-	-	0.15	0.20	66.94	37.27	37.91	31.23
P_2O_5	-	-	-	-	41.28	-	-	-	-
Cl	-	-	-	-	0.30	-	0.61	0.55	-
K_2O	-	-	-	-	-	-	9.36	8.94	-
CaO	-	-	-	-	54.36	0.91	-	-	-
Ti_2O_3	0.16	0.20	-	-	-	-	1.20	1.37	-
V_2O_5	0.29	0.29	0.42	0.31	-	-	-	-	-
Fe_2O_3	98.97	99.13	99.40	99.54	0.44	-	19.63	20.02	1.01
ZrO_2	-	-	-	-	-	-	-	-	67.76

5.1.3. SEM-EDS JOEL 7100F

This subsection shows the results of the limestone, olivine and bentonite samples analysed with the JEOL 7100F SEM-EDS. Figure 5.2 shows the SEM backscatter images of the limestone sample with corresponding chemical compositions in Table 5.6. With the SEM-EDS inclusions of a zinc sulfite ($(Zn, Fe)S$), pyrite (FeS_2), iron oxide, dolomite ($CaMg(CO_3)_2$) and quartz (SiO_4) have been detected. The SEM-EDS data of dolomite phases show high concentrations of V off 2.46 wt% oxide, but these are artefacts of the Ca Kα and Mg Kα peaks. Iron oxides and quartz show low concentrations of V, but these are not the main constituents of limestone and are, therefore, rare. The SEM-EDS data indicates high concentrations of Mo in the quartz, but this is an artefact of the Si and O $K\alpha$ peak.

The backscatter images of the olivine sample are shown in Figure 5.3, with Table 5.7 showing the corresponding chemical analysis. The chemical analysis shows that the olivine grains contain Fe and Mg. Therefore, the olivine phases are a mixture of mainly forsterite and, in smaller amounts, fayalite (Fe_2SiO_4). The olivine composition is usually referred to by Fo number, here $Fo90$. The sample also shows pyroxene gangue material. Pyroxene has a general formula of $XY(Si, Al)_2O_6$ where X could be Ca, Na, Fe, Mg, Sn, Mn or Li and Y could be $Cr, Al, Mg, Co, Mn, Sc, Ti, V$ or Fe. Also phases of pyrite, chromite ($FeCr_2O_4$, lizardite ($Mg_3(Si_2O_5)(OH)_4$) and iron oxide have been identified. V was only

measured by SEM-EDS in chromite but is probable an artefact as the $Cr\ K_\alpha$ peak shares the same energy levels as the $V\ K_\beta$ peak.

Figure 5.4 shows the SEM image of the bentonite sample with corresponding Table 5.8 showing the chemical analysis of different phases. As shown in Figure 5.4b, bentonite has a wide variety of silicate structures on a small particle. The Al and $Na\ Al$ silicates have higher concentrations in Si, but are lower in Al than the montmorillonite. Most likely, these silicates are part of the amorphous fraction of the XRD. High concentrations of P in the montmorillonite are most likely an artefact of the O plus $Al\ K\alpha$, and Mo is most likely Mo an artefact of the Si and $O\ K\alpha$ peak. Using the SEM-EDS, some inclusions of quartz, calcite, feldspar, Ti oxide, pyrite, and baryte ($BaSO_4$) were detected. One of the two Ti oxides is likely to be a rutile (TiO_2) phase, but the other shows high concentrations of Ca, Si, and Mg. It could be that this is another phase, the rutile is diluted, or the electron beam was too large for that spot and received signals from another phase. One of the feldspars is high in K, which matches with the sanidine ($K(AlSi_3O_8)$) from the XRD. Montmorillonite also shows low concentrations of V, which could also be a substitution for Al. Also, baryte shows low concentrations of V but is rare in the sample. Rutile shows low concentrations of V, which is probably an artefact because the K_β peak of Ti shares almost the same energy level as the K_α peak of V. The other phases might contain some V but in concentrations smaller than 0.1 wt% oxide.

In conclusion, iron oxide is the only phase in the total blend of the pellet that contributes significantly to the V concentrations in the pellet. Although the concentrations are relatively low, this is the main constituent in the pellet, as shown in Section 3.2. There might be other phases containing V, but in even smaller concentrations than the magnetite, and these are rare, so they are neglectable.

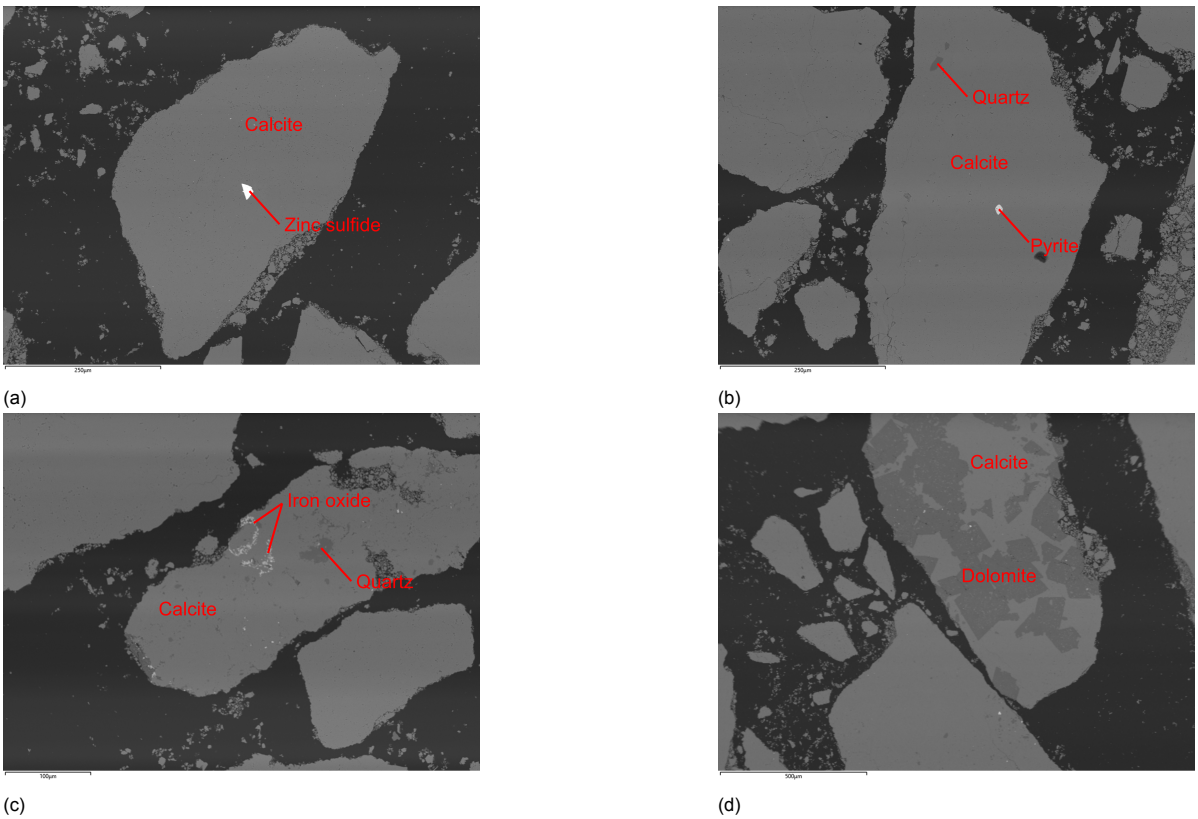

Figure 5.2: SEM backscatter images of the limestone sample: (a) zinc sulfide inclusion, (b) pyrite and quartz inclusion, (c) iron oxide and quartz inclusion, and (d) calcite with dolomite.

Table 5.6: SEM-EDS point analysis data of the limestone sample in wt% oxide.

Oxide	Calcite		Zinc sulfide	Pyrite	Iron Oxide		Quatz		Dolomite
Na_2O	0.41	0.46	3.18	-	1.16	0.89	0.65	0.67	0.56
MgO	1.68	0.67	0.44	-	4.62	5.21	0.01	0.02	48.09
Al_2O_3	0.09	0.10	0.08	0.05	3.56	3.05	0.04	0.75	0.36
SiO_2	-	-	-	-	6.22	6.02	93.46	92.56	0.94
P_2O_5	0.05	-	3.02	-	0.16	0.22	0.36	0.51	0.22
SO_3	0.66	0.14	56.26	73.38	0.12	0.19	-	-	0.93
K_2O	0.05	0.07	3.01	0.01	0.12	0.12	-	-	0.04
CaO	96.91	98.48	0.71	0.52	37.02	30.84	-	0.02	46.39
V_2O_5	-	-	-	-	0.19	0.19	0.11	0.08	2.46
Cr_2O_3	-	-	0.08	-	0.12	0.04	-	-	-
Fe_2O_3	0.06	0.09	-	22.87	46.45	53.03	0.02	-	-
ZnO	-	-	30.19	0.11	0.11	0.13	0.10	0.08	0.01
MoO_3	0.08	-	3.03	3.06	0.16	0.06	5.26	5.32	-

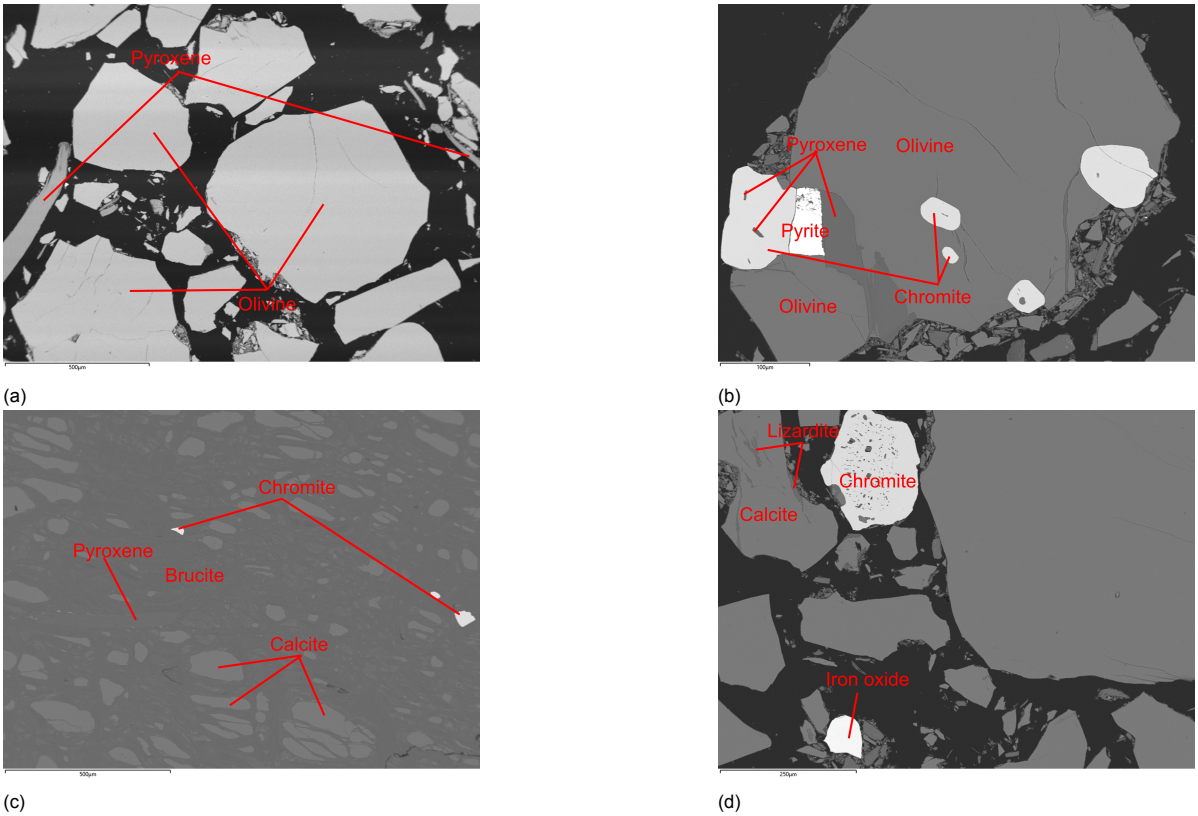

Figure 5.3: SEM backscatter images of the olivine sample: (a) olivine with pyroxene gangue, (b) olivine with pyroxene, chromite, and pyrite inclusions, (c) particle with structures of brucite, pyroxene, chromite, and calcite, and (d) iron oxide and chromite gangue and olivine with lizardite intrusions.

Table 5.7: SEM-EDS point analysis data of the olivine sample in wt%.

Oxide	Olivine		Chromite		Pyroxene		Pyrite	Brucite	Iron oxide	Lizardite
Na_2O	-	-	0.16	-	0.04	-	1.48	-	0.05	-
MgO	57.27	57.45	11.61	13.89	44.02	44.24	0.05	91.09	0.09	51.02
Al_2O_3	-	-	5.65	8.01	16.21	15.67	0.06	-	0.53	-
SiO_2	39.01	38.95	0.04	0.03	36.16	36.41	0.04	1.98	0.11	48.07
P_2O_5	-	-	0.08	-	-	-	0.19	-	-	-
SO_3	-	-	-	-	0.03	-	70.62	0.03	-	-
K_2O	0.03	0.02	0.02	-	0.03	-	0.02	0.02	-	0.03
CaO	-	0.02	0.02	0.02	-	-	-	0.05	-	0.02
V_2O_5	-	-	0.41	0.35	0.02	0.02	0.03	-	-	-
Cr_2O_3	-	0.04	54.82	56.37	2.15	2.31	0.17	0.02	0.03	-
Fe_2O_3	3.69	3.52	27.19	21.33	1.34	1.35	27.35	6.81	99.20	0.86

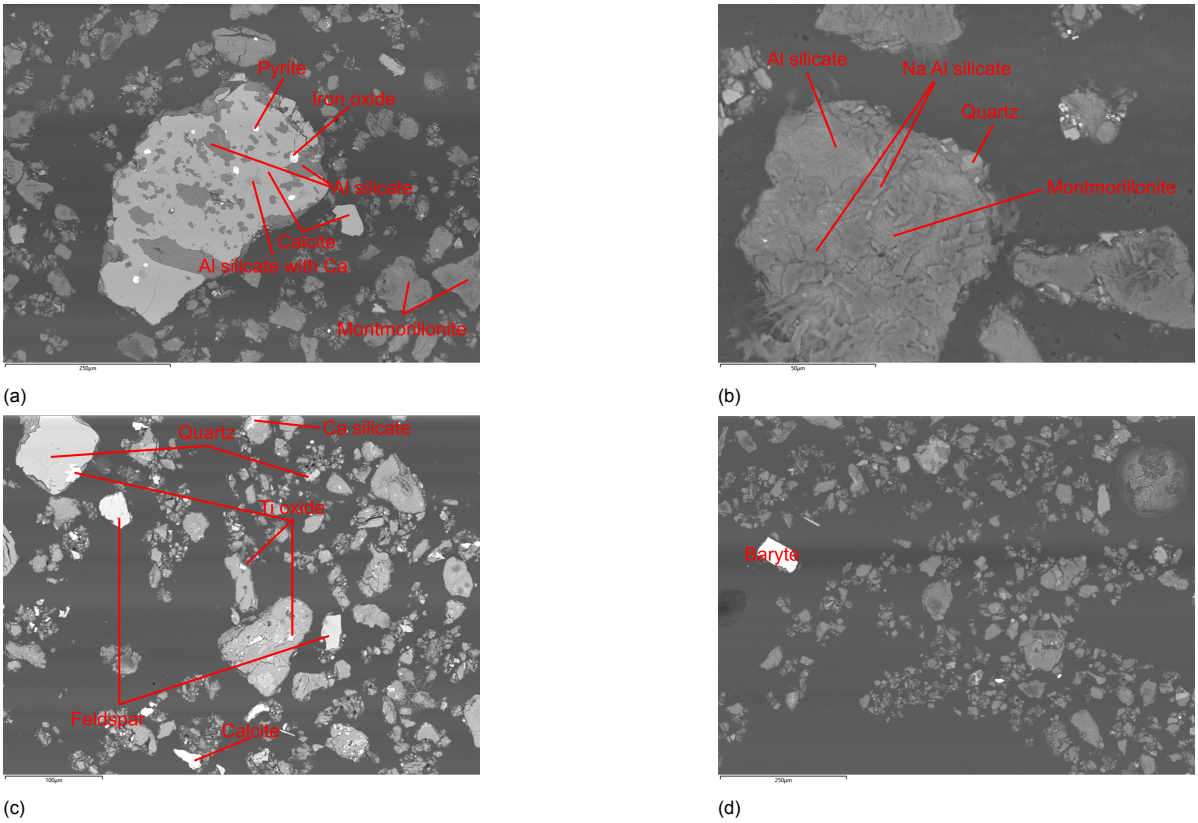

Figure 5.4: SEM backscatter of the bentonite sample: (a) silicate with inclusions, (b) bentonite particle, (c) quartz, feldspar, Ca silicate, rutile and calcite gangue, and (d) baryte gangue.

Table 5.8: SEM-EDS point analysis data of the bentonite sample in wt% oxide.

Oxide	Quartz		Calcite		Feldspar		Rutile		Pyrite	Baryte	Iron oxide	Montmorillonite			Aluminium silicate		Na Al silicate		Calcium silicate
Na_2O	0.71	0.89	0.44	0.05	3.11	7.59	-	2.08	-	1.05	2.31	3.77	2.08	0.57	0.89	2.17	9.79	10.60	2.03
MgO	0.01	0.10	0.28	0.08	-	-	0.03	5.58	0.01	0.14	3.55	3.54	3.24	3.74	1.57	1.21	1.10	1.08	2.59
Al_2O_3	-	1.34	0.73	0.03	15.30	22.69	0.19	0.60	0.02	0.24	1.07	21.32	22.34	22.64	9.39	5.91	6.41	10.44	1.59
SiO_2	93.40	92.47	1.39	0.08	72.04	61.82	0.26	5.24	-	-	3.81	65.26	67.23	65.05	83.45	86.20	79.83	75.07	51.03
P_2O_5	0.42	0.34	-	0.02	1.40	1.97	0.05	0.73	-	0.21	0.05	2.65	1.89	1.89	1.07	1.32	0.64	0.47	0.53
SO_3	-	-	-	0.04	-	-	-	14.95	62.59	65.72	0.64	-	-	-	-	-	-	-	1.79
K_2O	-	-	0.09	0.10	5.40	-	-	0.09	0.02	0.08	0.11	-	-	-	-	-	-	-	0.14
CaO	-	-	95.00	98.74	-	3.56	0.14	14.22	0.72	0.07	1.29	0.19	0.03	0.27	0.40	-	-	0.17	38.59
Ti_2O_3	0.02	-	0.51	0.11	0.12	0.06	98.37	47.12	-	0.31	-	0.08	0.08	2.37	0.01	0.04	0.08	0.08	0.33
V_2O_5	0.09	0.10	-	-	-	0.06	0.68	0.56	-	1.00	0.01	0.10	0.05	0.13	0.10	0.10	0.03	0.02	0.04
Fe_2O_3	0.03	0.08	1.42	0.71	0.01	0.12	0.29	8.19	34.10	0.13	86.98	0.91	1.03	1.37	0.52	0.31	0.45	0.81	0.14
MoO_3	5.29	4.64	0.13	0.03	2.63	2.13	-	0.57	2.55	1.34	0.19	2.19	2.02	1.98	2.58	2.73	1.68	1.25	1.19
BaO	0.03	0.03	-	0.02	-	0.01	-	0.08	-	29.71	-	-	-	-	0.01	-	-	-	-

5.2. Microstructural analysis of fired pellets

Firing pellets lead to complex microstructures, where the patterns differ depending on the pellet's location in the pellet bed. In Section 3.3, it is shown that the bottom zone in the pellet bed is fired for a shorter duration than the top layer. Because the air travels from the top to the bottom, magnetite grains of the pellets in the top layer are generally better oxidised to hematite than in the bottom layer. However, this doesn't mean the pellets in a certain zone are equally oxidised. Also, within the pellet itself, there is variation in the microstructures. In Subsection 2.2.4 it is discussed that the oxidation front moves from the shell to the core of the pellet, this can influence the oxidation state of the iron oxides depending on the location in the pellet. Also, the flux and gangue particles can influence the microstructures in a small local area, causing inhomogeneity.

The microscopy images of the researched pellets are shown in 5.5. In these pellets the following broader categories of pellets are encountered:

1. Magnetite dominates the pellet's core with minimal lamellar hematite formation on the magnetite grains. The grains have lost their original angular shape and are somewhat rounded, with some glass or silicate melt in between. This indicates the pellet has seen a standard firing profile but insufficient oxygen levels. This is encountered in the core of pellets 5177-2 and 5171-2, where 5171-2 has a finer grid than 5177-2. Microscopy and SEM images of the cores of these pellets are shown in Figure 5.6.

2. The same high-temperature conditions as in item 1, but the magnetite spinel has oxidised hematite in the presence of a liquid melt phase. In the liquid, Mg is dissolved from a flux component and stabilises the spinel structure, preventing the oxidation to hematite, as explained in 2.2.4. So, in this area, the dominant magnetite spinel plus a Mg rich melt phase oxidises to dominant hematite plus magnesioferrite spinel solution plus liquid. Because the reaction occurs in the presence of the liquid fraction, the phases are intimately intergrown. This microstructure is encountered in the cores of pellets 5177-1, 5171-1 and 9999. The microscope and SEM images of the cores of these pellets are shown in Figure 5.7. As particles sinter with each other in the presence of a liquid, the liquid can get trapped. If insufficient energy is available, the liquid will form pockets, trying to minimise the surface tension. This is shown in Figures 5.7b and 5.7d. If the temperature had been higher, the liquid would have enough energy to find its way to the pores.

3. This item has the same phases in the same propositions, as described in item 2. The main difference is that the magnetite spinels oxidised before forming any significant liquid fraction. So, the formation of the liquid fraction is restricted to the space between the hematite ore grains. So here, only the outlines of the original iron oxides have been replaced with hematite plus magnesioferrite spinel plus liquid and are not intimately intergrown. This mainly occurs in the shell of the pellet as the oxidation front moves inwards. The microscope and SEM images of the shell of pellet 5177-1 are shown in Figure 5.9.

4. This category represents pellets that are somewhat underfired. Here, less microstructure transformation by recrystallisation is visible in the presence of a liquid phase. This microstructure is encountered in the core of pellet 5177-3. The microscope and SEM images of the core of pellet 5177-3 are shown in Figure 5.9.

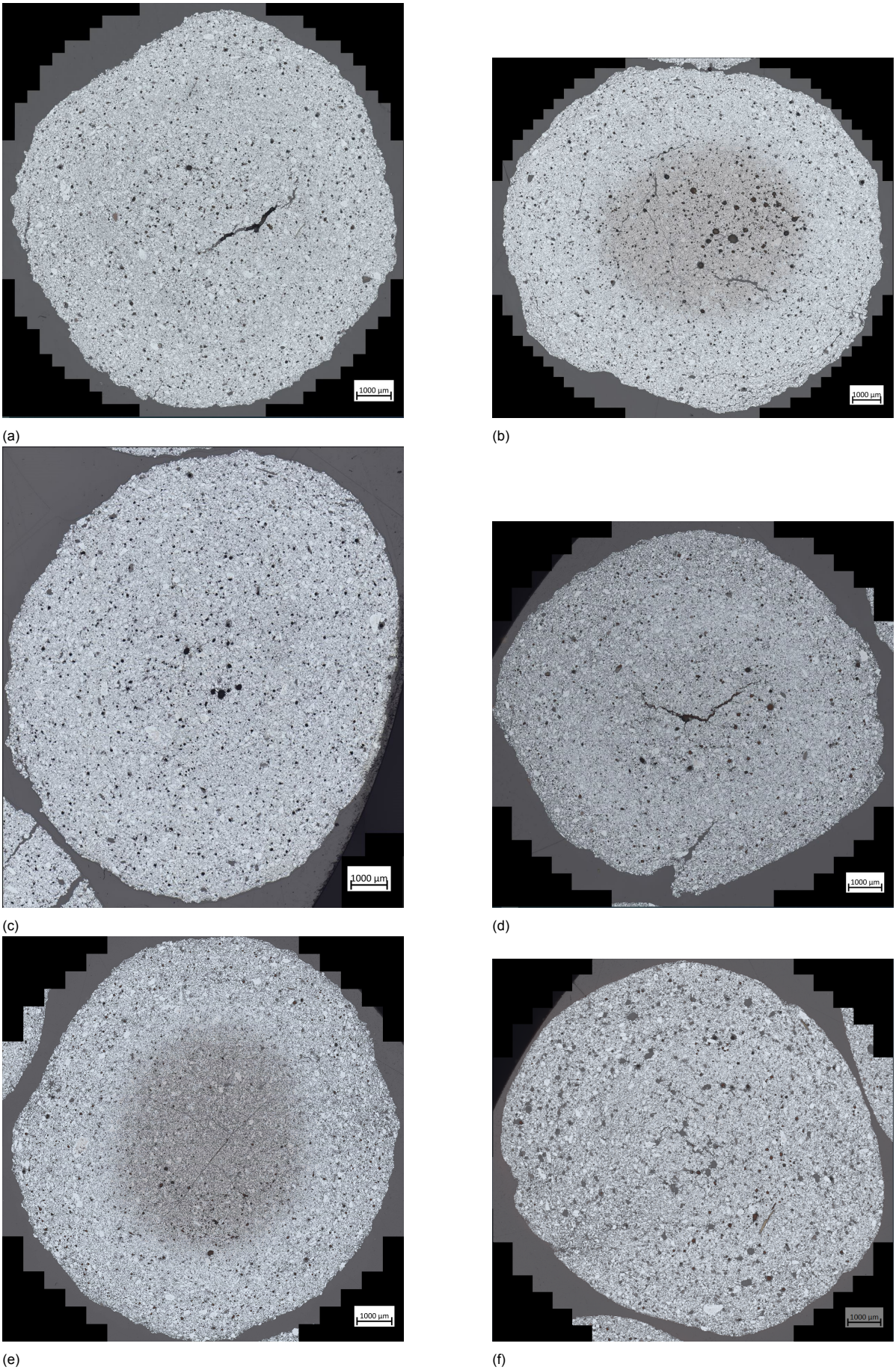

Figure 5.5: Polarised reflected light microscope images of all used pellets: (a) pellet 5177-1, (b) pellet 5177-2, (c) pellet 5177-3, (d) pellet 5171-1, (e) pellet 5171-2, and (f) pellet 9999.

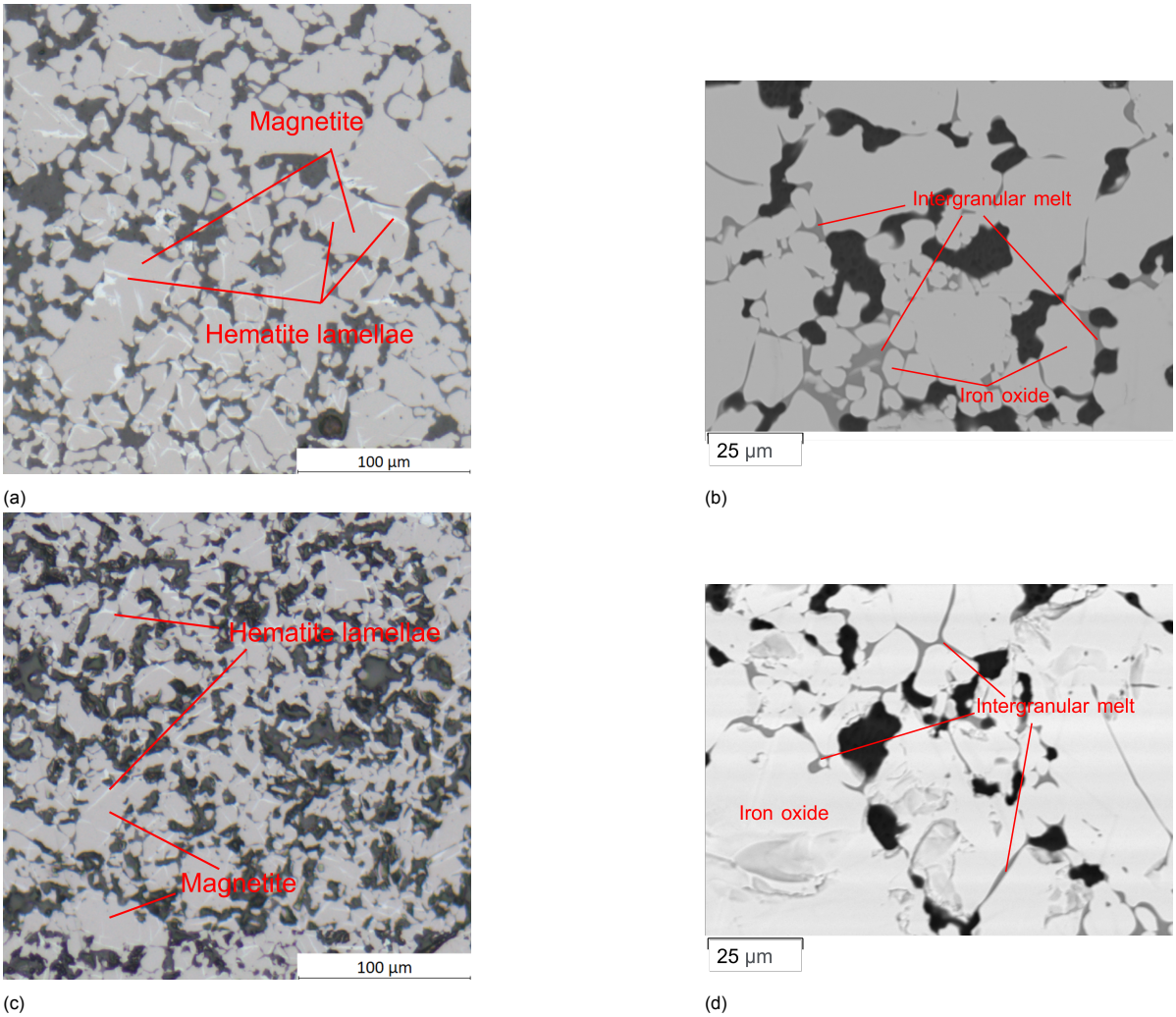

Figure 5.6: Micropcope and SEM images of microstructures in category 1, with (a) microscope image of the pellet 5177-2, (b) SEM image of pellet 5177-2, (c) microscope image of pellet 5171-2, and (d) SEM image of pellet 5171-2.

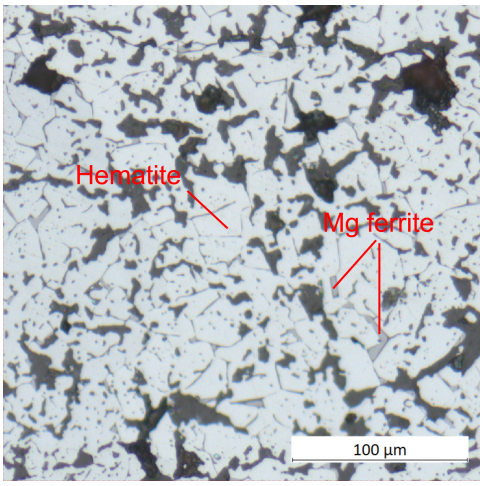

(a)

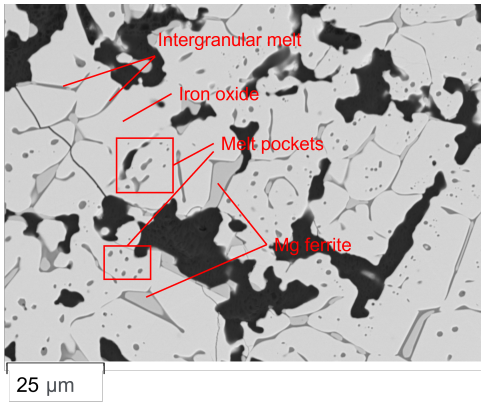

(b)

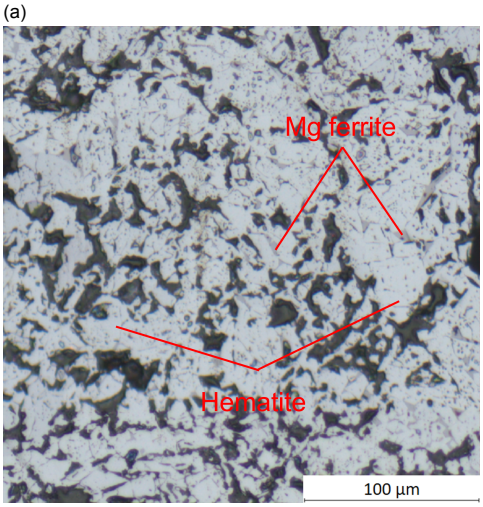

(c)

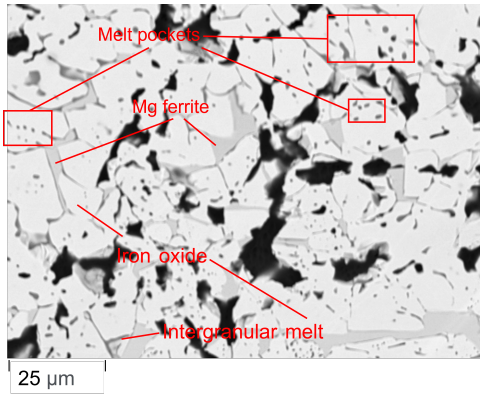

(d)

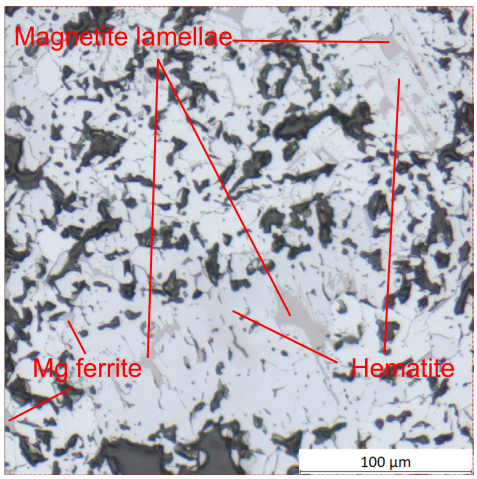

(e)

Figure 5.7: Micropcope and SEM images of microstructures in category 2, with (a) microscope image of the pellet 5177-1, (b) SEM image of pellet 5177-1, (c) microscope image of pellet 5171-1, (d) SEM image of pellet 5171-1, and (e) SEM image of pellet 9999

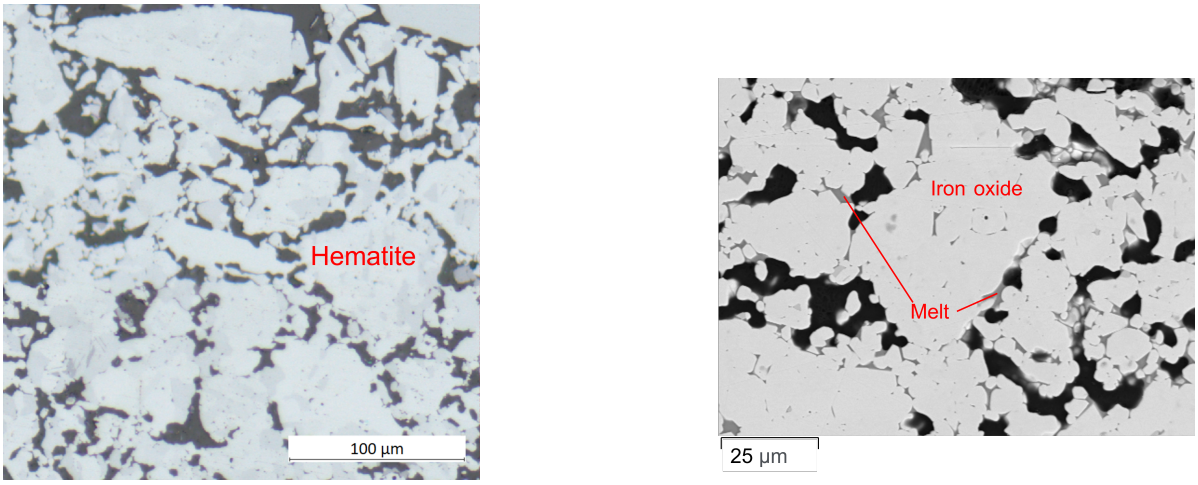

(a) (b)

Figure 5.8: Micropcope and SEM images of microstructures in category 3, with (a) microscope image of the pellet 5177-1, and (b) SEM image of pellet 5177-1.

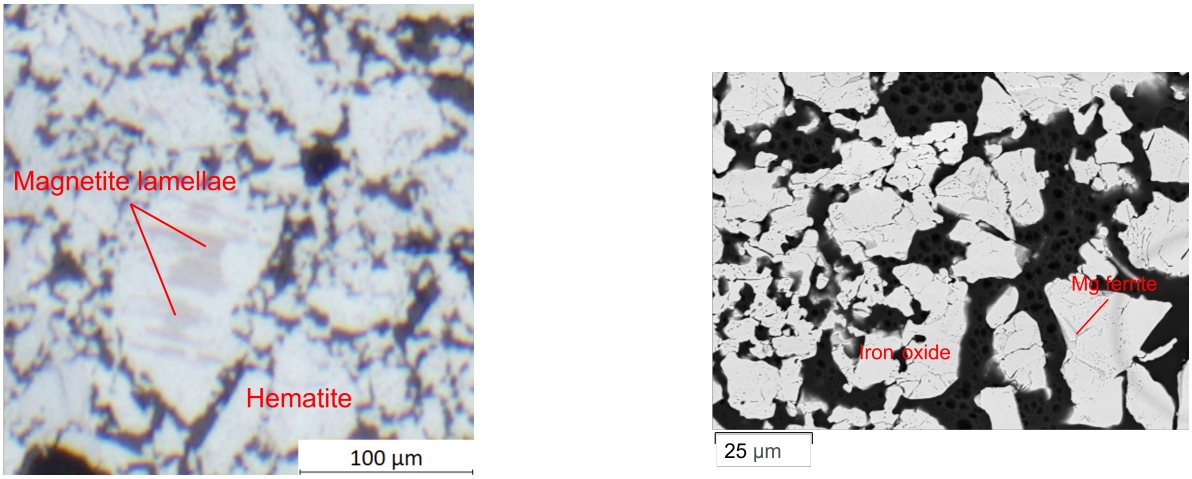

(a) (b)

Figure 5.9: Micropcope and SEM images of microstructures in category 4, with (a) microscope image of the pellet 5177-3, and (b) SEM image of pellet 5177-3.

5.3. EDS maps

This section will show different SEM-EDS maps and backscatter images of certain areas in the pellet which have been captured by Aztec. The aim is to visually show in which phases the V is present after firing and what artefacts can occur. Figure 5.10, shows the backscatter image and V, Al, Cr, Fe, Mg, Si and Ti maps of an area in the core of pellet 5177-2. The brighter the colours on the map, the higher the amount of counts detected of characteristic X-rays. On the backscatter image, the pores filled with epoxy can be recognised by the dark grey/black colour, while the glassy melt phase can be recognised by the medium-grey colour between the light-grey grains. As is shown on the other maps, this melt phase is high in Ca, Al and Si. For Mg the map shows that the highest concentrations are present in the iron oxides and low concentrations in the glass melt, but this is caused by an artefact where the sum of the Fe Lα peak with the O Kα matches the Mg Kα peak. Therefore, the Mg is probably present in the glassy melt phase, not the iron oxides. The maps show that trace elements like V, Cr and Ti are most abundant in the intergranular melt phase.

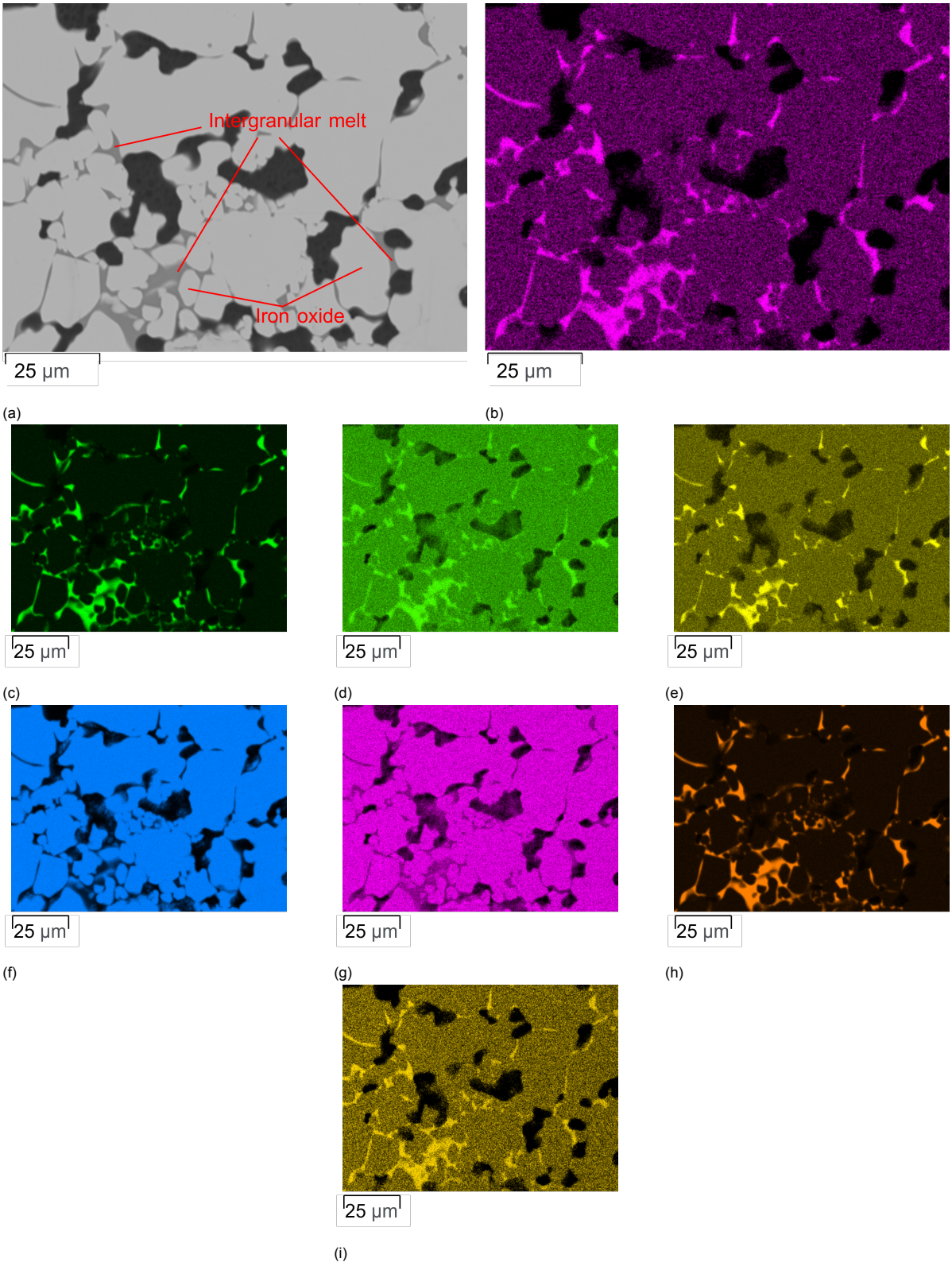

Figure 5.10: EDS maps of the core in pellet 5177-2. The brighter the colour, the higher the concentration of relevant elements, with (a) SEM backscatter image, (b) purple representing V concentration, (c) green representing Ca concentration, (d) green representing Al concentration, (e) yellow representing Cr concentration, (f) blue representing Fe concentration, (g) purple representing Mg concentration, (h) orange representing Si concentration, and (i) yellow representing Ti concentration.

Besides that V is present in the intergranular melt phases, Figure 5.11 shows that the V is also present in the melt pockets, which are present in well-sintered hematite grains. These pockets show again high concentrations of Ca and Si.

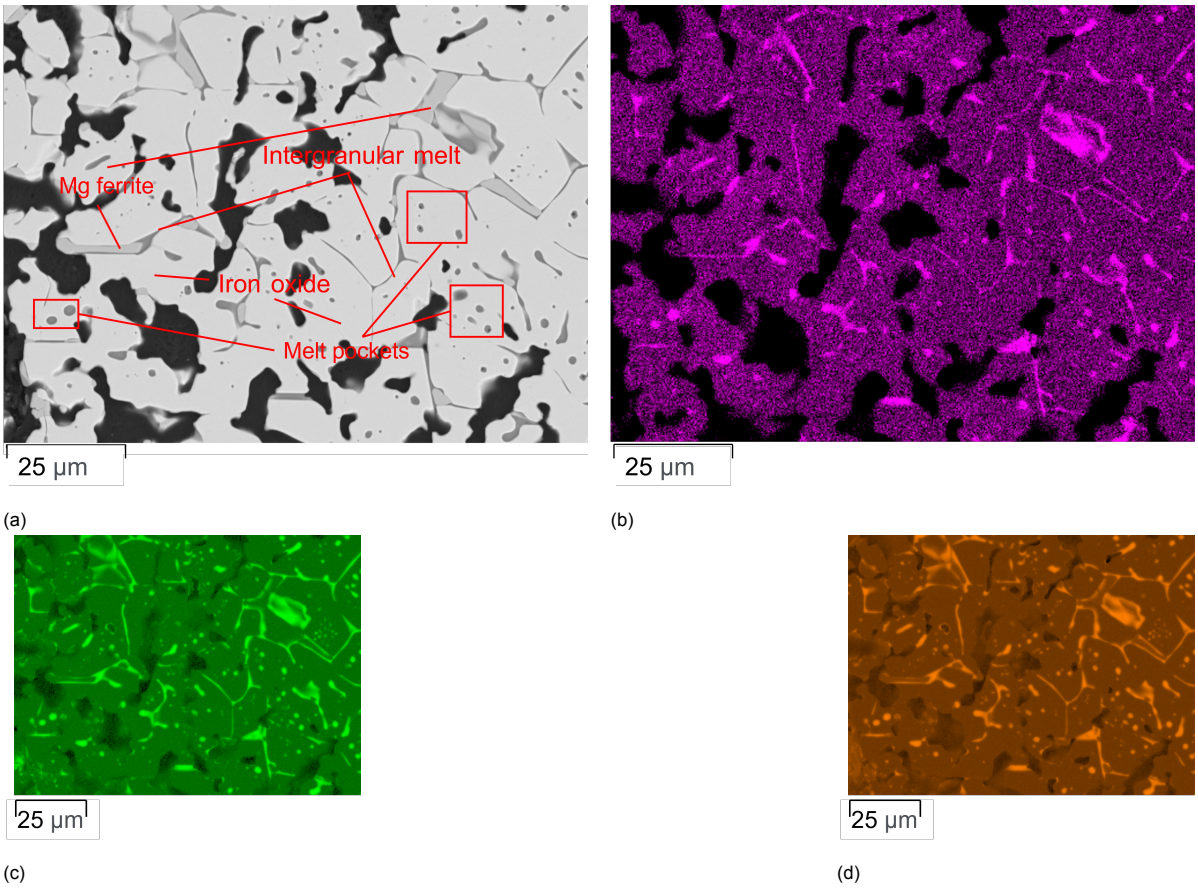

Figure 5.11: EDS maps of the core in pellet 5177-1. The brighter the colour, the higher the concentration of relevant elements, with (a) SEM backscatter image, (b) purple representing V concentration, (c) green representing Ca concentration, and (d) brown representing Si concentration.

Another artefact occurs in the EDS map of V when high concentrations of Ti are detected. The problem is that the Kβ peak of Ti interferes with the Kα peak of V. This is clearly shown in Figure 5.12, which shows a grain with two phases, of which one is a rutile (TiO_2) phase. The titanium and V maps show the same brightness, indicating high V concentration in rutile phases. Point analysis has measured a concentration of 88.6 % TiO_2 and 0.61 V_2O_5. Here, the software already processed the data to suppress the artefacts, but the V peak in the acquired spectrum of the point analysis is so large and obviously an artefact that it is questionable if there is any V present.

Knowing that the artefacts can occur improves the quality of the PARC maps because PARC automatically classifies phases based on the same data sets used to compile these EDS maps. With these artefacts present, these phases could be classified incorrectly. Therefore, the PARC model has been amended to prevent these artefacts. With the point analysis, it can be shown that the Mg will mostly be present in the melt phase and not in the iron oxide, but this shows that Mg can not be used to make a distinction between the iron oxide and the melt phase in PARC.

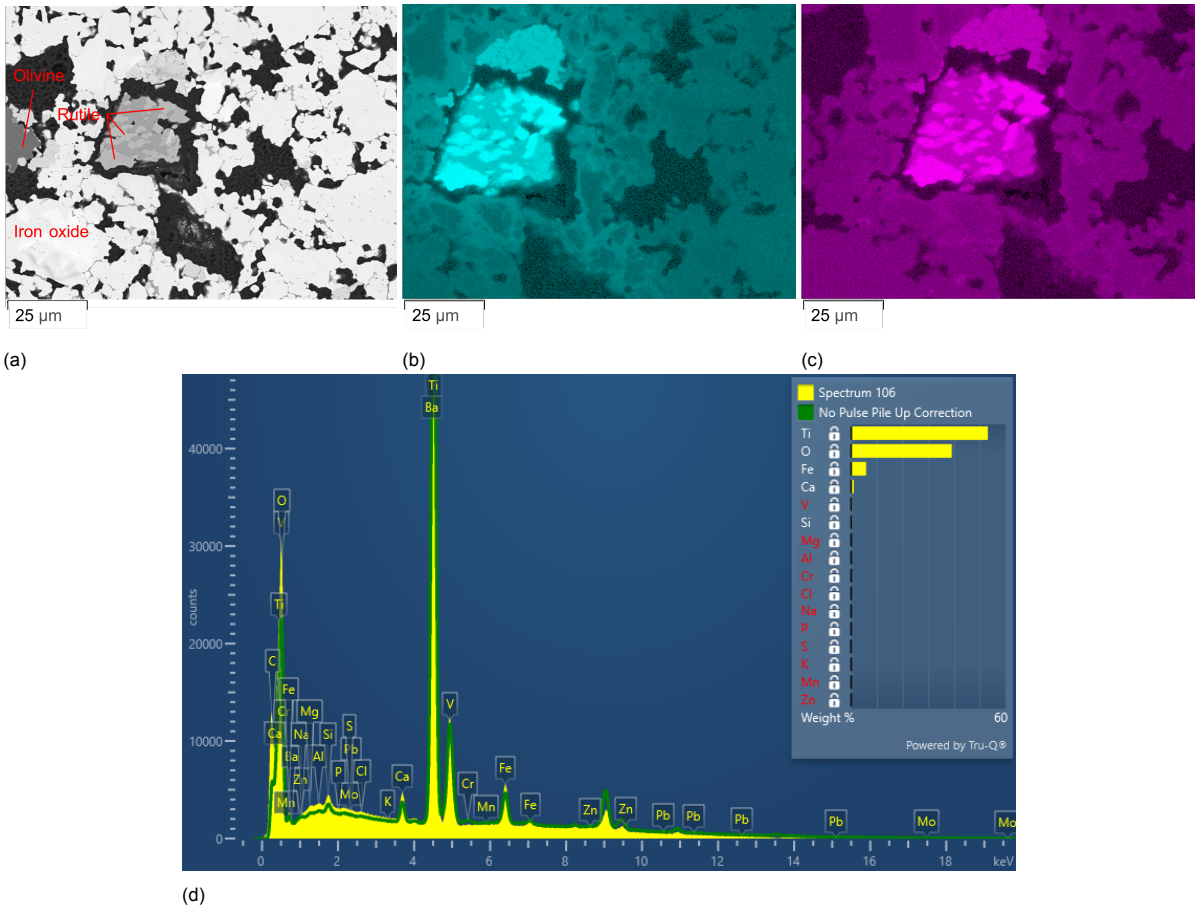

Figure 5.12: EDS maps of rutile particle. The brighter the colour, the higher the concentration of relevant elements, with (a) SEM backscatter image, (b) light blue representing Ti concentration, (c) purple representing V concentration, and (d) EDS spectrum of point analysis on rutile phase.

5.4. Pinhole traverses

This section shows the outcomes of the SEM-EDS pinhole traverses analysed with PARC. The pellets used for the pinhole traverse are 5177-1, 5177-2, 5177-3, 5171-1, and 5171-2. The aim is to give insight into the phase abundances of the different samples. The individual tiles along the pinhole traverse have been processed with PARC to characterize each pixel measured with the SEM-EDS, as explained in Section 4.2. For each tile, the area of the different phases is calculated. A graphical presentation of the phase abundances of the tiles along the pinhole traverse, excluding the porosity in the measured areas, and for the porosity are shown in the appendix.

The mean area % for the melt, iron oxide, magnesium ferrites and other phases is calculated based on the individual tiles' results. For the melt, this is done over the entire pinhole, for the rim, represented by the first ten tiles, and the core, represented by the last ten tiles and the results are shown in Table 5.9. These 10 tiles cover a distance of 0.92 mm, about 8 % of the diameter of the pellet. This is done this way to stay consistent because it is not always clear where the exact boundary is between the different zones. The mean area % excludes the porosity. The porosity of the different samples is shown in Table 5.10.

What stands out is pinhole 5177-1 and pellet 5171-1, which have a respectively significantly higher and lower percentages of melt phase than other pellets. That pellet 5171-1 has a lower percentage of melt is not surprising as for the low B_2 pellets, only 0.42 wt% of limestone flux is used, while for the high B_2 pellet 1.61 wt%. It is more surprising that pellet 5171-2 still has a high melting percentage. Still, for all pellets, the standard deviation is high, so the actual percentages of the pellets can deviate from what is presented here. For pellets 5177-3 and 5171-1, it is shown that the melt percentages are significantly lower in the core of the rim of the pellet. In Section 5.2, the pellet 5177-3 has been

described as somewhat underfired, which could cause less melt forming in the core.

Most of the phases consist of iron oxides, which vary between 88.56 and 93.03 area %. The variation could be caused by the different ratios of magnetite and hematite and the number of secondary phases that melt and magnesium ferrite formed. The area % of magnesium ferrite varies between 1.04 and 3.51 area $.

Table 5.9: Mean area of melt phases, iron oxides, magnesium ferrite and other phases in different samples. The mean melt with its standard deviation is given for the total pinhole traverse, rim and core. The mean of the rim is the mean of the first 10 tiles of the traverse, and of the core is the last 10 tiles. The phase abundances are corrected for epoxy.

Sample	Mean melt [%]	σ	Mean melt rim [%]	σ	Mean melt core [%]	σ	Mean iron oxide [%]	Mean magnesium ferrite [%]	Mean other phases [%]
5177-1	6.16	1.35	5.66	1.46	5.67	0.70	88.56	3.51	0.35
5177-2	4.11	1.48	2.90	1.44	4.71	1.25	93.03	1.04	0.02
5177-3	4.39	2.49	6.25	2.08	1.60	1.33	90.57	2.75	0.82
5171-1	2.27	1.44	2.50	0.39	1.37	1.36	91.21	2.27	0.22
5171-2	4.15	1.28	4.23	0.73	4.61	1.48	91.73	1.08	0.07

Sample 5177-3 shows a much higher porosity than the other pellets, wherein the core and rim reach a porosity of 29 area %. Unfortunately, the standard deviation is so high that all results fall in each other's error margins.

Table 5.10: Mean area and standard deviation of the porosity in different samples. Mean of the total pinhole traverse, rim and core. The mean of the rim is the mean of the first 10 tiles of the traverse, and of the core is the last 10 tiles.

Sample	Mean porosity [%]	σ	Mean porosity rim [%]	σ	Mean porosity core [%]	σ
5177-1	22.52	8.77	21.03	12.09	20.24	6.62
5177-2	23.19	8.88	20.13	9.14	23.79	5.29
5177-3	26.55	7.57	29.25	8.60	29.36	7.69
5171-1	17.20	7.96	17.75	2.96	17.60	7.26
5171-2	20.69	6.46	17.52	4.75	23.42	3.62
Mean	**22.03**		**21.14**		**22.88**	

5.5. Chemical analysis

The SEM-EDS point analysis measures the chemical composition of different phases in the pellet. This section aims to quantify the V content of those phases. Because the melt is inhomogenous, the V content varies widely. Many point analyses have been carried out; this data is listed in the appendix.

If the melt phase is too shallow or narrow, the electron beam of the SEM also penetrates underlying or surrounding phases. This dilutes the signal received with other phases than intended. To improve the quality of the data, melt phases with a Fe_30_5 higher than 40 wt% oxide have been filtered out for further analyses.

The statistics of the V content are listed in Table 5.11. Here, the V content for the melt is shown in pellets 5177, 5171, and 9999 and in the leached 5177 pellets. It shows that the V concentration in the melt of pellet 5177 and 9999, which are high in B_2, are higher than that of pellet 5171, which is low in B_2. In addition, the statistics of V are also calculated for the iron oxides and magnesium ferrites in the pellets. It is shown that the V concentration in the iron oxides is very low but not entirely gone. This means that not all the V is in the melt phase after firing. When iron oxides form magnesium ferrite, the V is mostly removed from the spinel structure.

Table 5.12: Pearson correlation coefficient between the concentrations of Ca and V in melt phase corresponding to data shown in Figure 5.13.

Phase	ρ
Melt 5171	0.26
Melt 5177	0.38
Melt 9999	0.42

Table 5.11: Statistical data on V concentrations from point analysis on different phases in pellet.

Phase	Mean	Median	Minimum	Maximum	σ	Data points
	% oxide					
Melt 5171	0.68	0.36	0.04	4.26	0.83	66
Melt 5177	3.22	3.30	0.13	5.52	1.43	84
Melt 9999	0.69	0.39	0.05	2.90	0.78	29
Melt in leached 5177	2.68	2.76	0.00	7.22	1.79	56
Melt near olivine	0.12	0.00	0.00	0.87	0.25	25
Iron oxide	0.19	0.20	0.05	0.39	0.08	39
Magnesium ferrite	0.03	0.04	0.00	0.07	0.03	7

In Figure 5.13 CaO concentrations are plotted against V_2O_5 concentration in the melt phase of different samples. Through the data, a straight trendline is plotted, and for each plot, there seems to be a positive correlation between the Ca and V content, but the data is very scattered. Table 5.12 lists the Pearson correlation coefficient for the different pellets. This shows a medium correlation between these elements for pellet 5177 and 5999 and a weak correlation for pellet 5171. This indicates that the V contents depend on the Ca concentrations in the slag phase. PARC also shows this correlation, where Ca concentrations are plotted against V concentrations in a tile density plot of every pixel in a tile, shown in 5.13d.

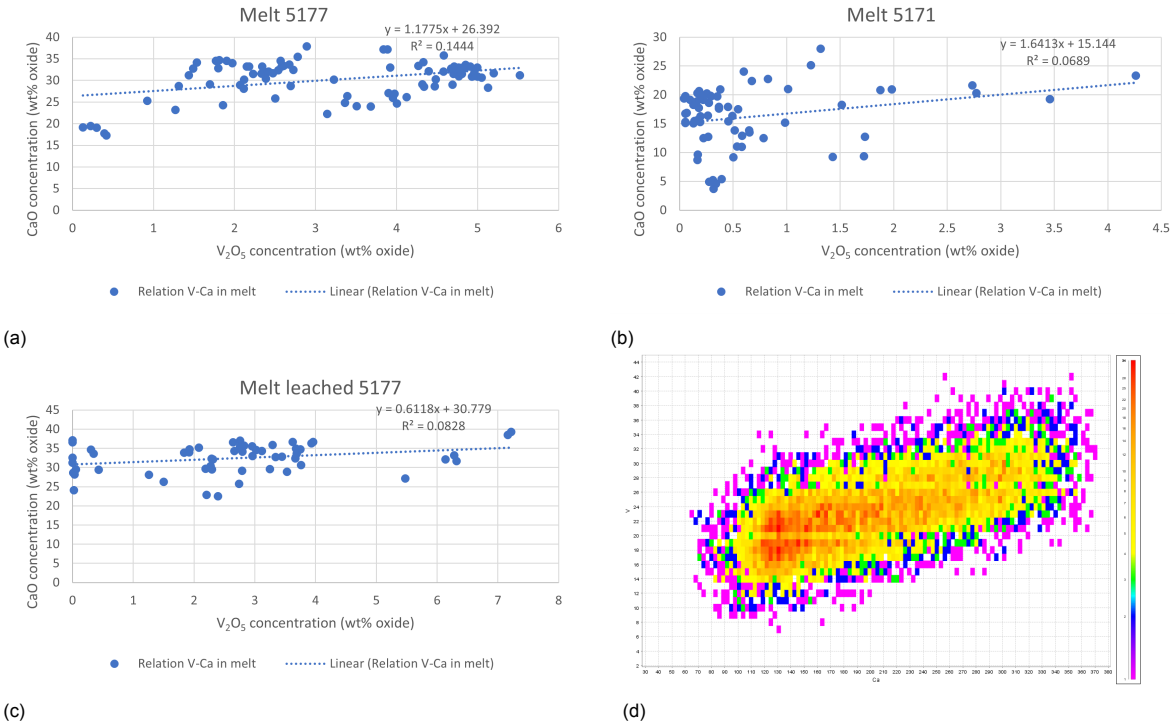

Figure 5.13: Relation between V and Ca in melt phase: (a) melt pellet 5177, (b) melt pellet 5171, (c) melt leached pellet 5177, and (d) PARC density plot of V and Ca of melt in pellet 5177 tile 3.

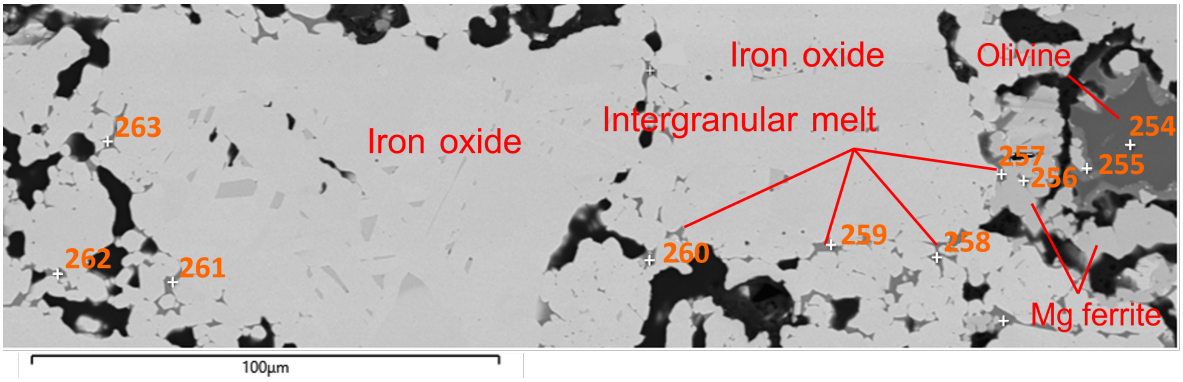

Figure 5.14: SEM image of an area near olivine particle partially dissolved in pellet 5177-1.

In Figure 5.11, one item is called melt near olivine. These are point measurements of the melt near flux particles that have only been partially dissolved. It stands out that the V content in this melt is almost 0 and much lower than that of other melts. Figure 5.14 shows an SEM backscatter image of an area around a partially dissolved olivine particle. The point analyses that have been taken in this area are displayed in Table 5.13 and correspond to the numbers displayed in Figure 5.14. The point analysis near the olivine particle shows that the V content is below the detection limit. The further away from the particle, the higher the V content until a certain distance.

Table 5.13: SEM point analysis in wt% oxide corresponding to Figure 5.14.

Element	254	255	256	257	258	259	260	261	262	263
	Olivine	Reaction zone olivine	Melt							
Na_2O	0.00	0.61	0.87	1.02	1.26	0.67	1.40	1.07	1.03	1.07
MgO	45.66	12.74	12.12	10.17	9.62	0.49	9.56	3.54	3.64	3.58
Al_2O_3	0.00	0.25	1.10	1.29	1.97	1.81	2.22	1.37	1.65	1.59
SiO_2	45.27	42.86	28.41	38.30	38.07	36.08	37.70	30.98	37.81	28.79
P_2O_5	0.00	0.00	0.00	0.00	0.04	1.36	0.00	0.61	0.83	0.62
SO_3	0.00	0.00	0.19	0.08	0.09	0.00	0.09	0.03	0.11	0.00
K_2O	0.01	0.13	0.11	0.14	0.20	0.64	0.23	0.38	0.59	0.35
CaO	0.02	38.88	22.97	34.58	34.00	38.48	32.54	25.74	36.67	22.53
Ti_2O_3	0.07	0.02	0.02	0.00	0.06	0.00	0.07	0.07	0.01	0.08
V_2O_5	0.00	0.00	0.06	0.00	0.54	7.16	0.00	2.74	3.96	2.39
Mn_3O_4	0.11	0.00	0.06	0.05	0.07	0.03	0.14	0.17	0.03	0.06
Fe_2O_3	8.45	4.26	33.85	14.13	13.97	13.09	15.77	33.01	13.31	38.70

Table 5.13 also shows that the main components of the secondary melt phase consist of Ca, Mg, Fe, Si and in lesser amounts Al Na, and V. The Mg is mainly high near the olivine particle, probably because the olivine starts reacting at higher temperatures as the limestone and gangue materials.

5.6. XRD results for the pellet

This section shows the results of the XRD analysis on the pellets. The pellets 5177 and 5171 were analysed using the powder diffraction method, and on pellet 5177, a pinhole traverse was conducted using point analysis from the rim to the pellet's core. The aim is to show if there are other major phases than iron oxide and if the melt phase has a crystal structure. If the melt has a glass structure, the X-ray should not diffract; therefore, it will not show a peak in the data. A silicon standard is added to calculate the amorphous content in the powder diffraction analysis. This is not possible with the point analysis. Note that the detection limit of the XRD is about 0.5 wt%.

Figure 5.15 shows the count peaks of the powder diffraction analysis of pellets 5177 and 5171. These peaks are used to calculate the mineral composition of the pellet. These results are shown in Table 5.14. This table shows the mineral composition after the correction of the silicon standard. The

result of pellets 5177 and 5171 shows that, respectively, 4.1 wt% and 6.7 wt% are amorphous. Although the melt will account for a substantial percentage of the amorphous content, other phases below the detection limit will also accumulate in this result. This will include phases like olivine and rutile, which are identified with the SEM-EDS but don't show in these results. It stands out that pellet 5171 shows a higher amorphous content than pellet 5177, although based on its B_2, you would expect more melt phase in pellet 5177 and, therefore, a higher amorphous content. Unfortunately, the standard deviation for both amorphous contents is high, so the results fall into errors for each other.

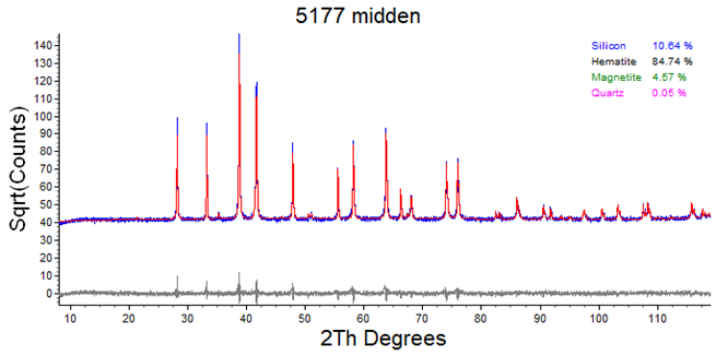

(a)

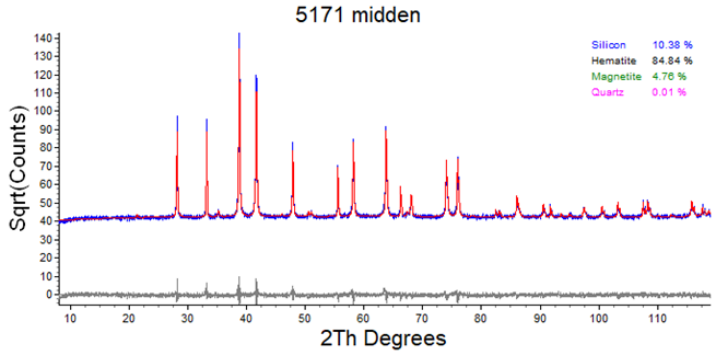

(b)

Figure 5.15: XRD powder refraction results of pellets: (a) pellet 5177, and (b) pellet 5171.

Table 5.14: XRD powder diffraction results corrected for silicon standard in compositional wt%.

Phase	**5177**	**σ**	**5171**	**σ**
Hematite	90.8	0.35	88.5	0.60
Magnetite	5.1	0.30	4.8	0.50
Quartz	0.0	0.20	0.1	0.20
Amorphous	4.1	1.25	6.7	1.25

The results of the pinhole traverse are combined in one graph, which is displayed in Figure 5.16. Using a silicon standard here is impossible, so the amorphous content can not be calculated. The results only show that there are major phases of hematite and magnetite. Akermanite is a mineral containing calcium, magnesium and silica, which could indicate that a small proportion of the melt phase has crystalised. The contact of this mineral varies between 0.4 and 0.1 wt%. Hedenbergite is a pyroxene mineral and could originate from gangue material.

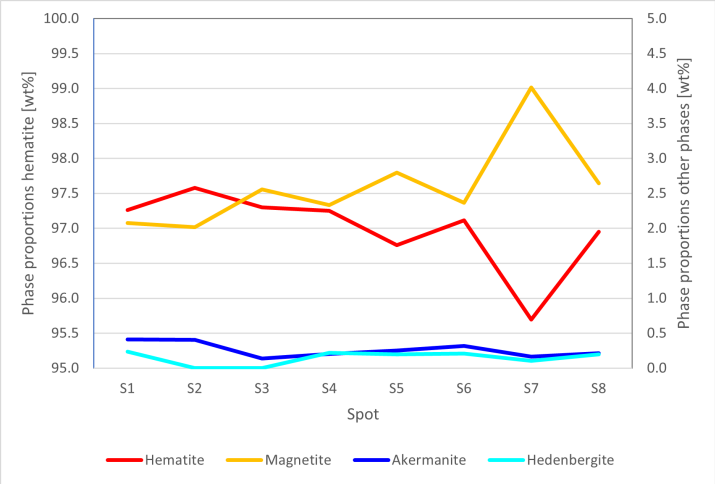

Figure 5.16: Results XRD pinhole traverse of pellet 5177-1 with point analyses.

5.7. LA-ICP-MS results

Only sample 5177-1 sample was used for the LA-ICP-MS analysis. This is because there was limited available time for the LA-ICP-MS. In addition, this test aims to validate previous results, which can suffice with one sample.

The sample is ablated in three zones in the pellet: the rim, mantle and core. The data from the LA-ICP-MS is processed in an Excel worksheet. The result is a list where, for each pixel, a V concentration is calculated. The pixel dimensions are 5x5 μm. Figure 5.17 shows a map of the results. It is clear to see that some spots are low in V. The bright green areas in the map have a concentration lower than 0.25 wt%. Unfortunately, these results can not be converted to wt% oxides because a limited range of elements is calculated, which does not cover the entire total weight. The means of each laser ablated area are listed in Table 5.15. There is little variation between the different areas; only the rim shows a slightly lower concentration of V than the mantle and core.

The boxplot in Figure 5.18 shows the result of the V concentrations for each area. Note that the spot size is quite large compared to the melt phase's dimensions; therefore, the melt phase is always diluted with iron oxides. Although the boxplot normally defines outliers in one population, multiple populations are combined in one plot. However, it still gives valuable insights into the data. One measurement in the mantle has a concentration of 12.7 wt% V. This could indicate that another phase is present, which has not been identified with the SEM-EDS or can be considered an outlier. Then there are a couple of measurements between 4 and 6 wt%. These concentrations are in the same range as the melt phase, considering the dilution of melt with iron oxides. The highest concentration of V measured in the melt is 8.67 wt%.

Unfortunately, the pixel size is too large to get a detailed map of the distribution of V in the pellet. So, the map can not be compared to the microscope image to show that the areas high in V are associated with the melt phase. However, Pearson's correlation between Ca and V is 0.51, which shows, like in Section 5.5, there is again a moderate correlation for the pellet with high B_2. Because the Ca content is linked to the melt phase, most of the V is likely present in the melt phase.

Table 5.15: Mean V concentrations of different laser-ablated areas in pellet 5177.

Location	Mean *V* concentration [wt%]
Core	0.24
Mantle	0.26
Rim	0.21

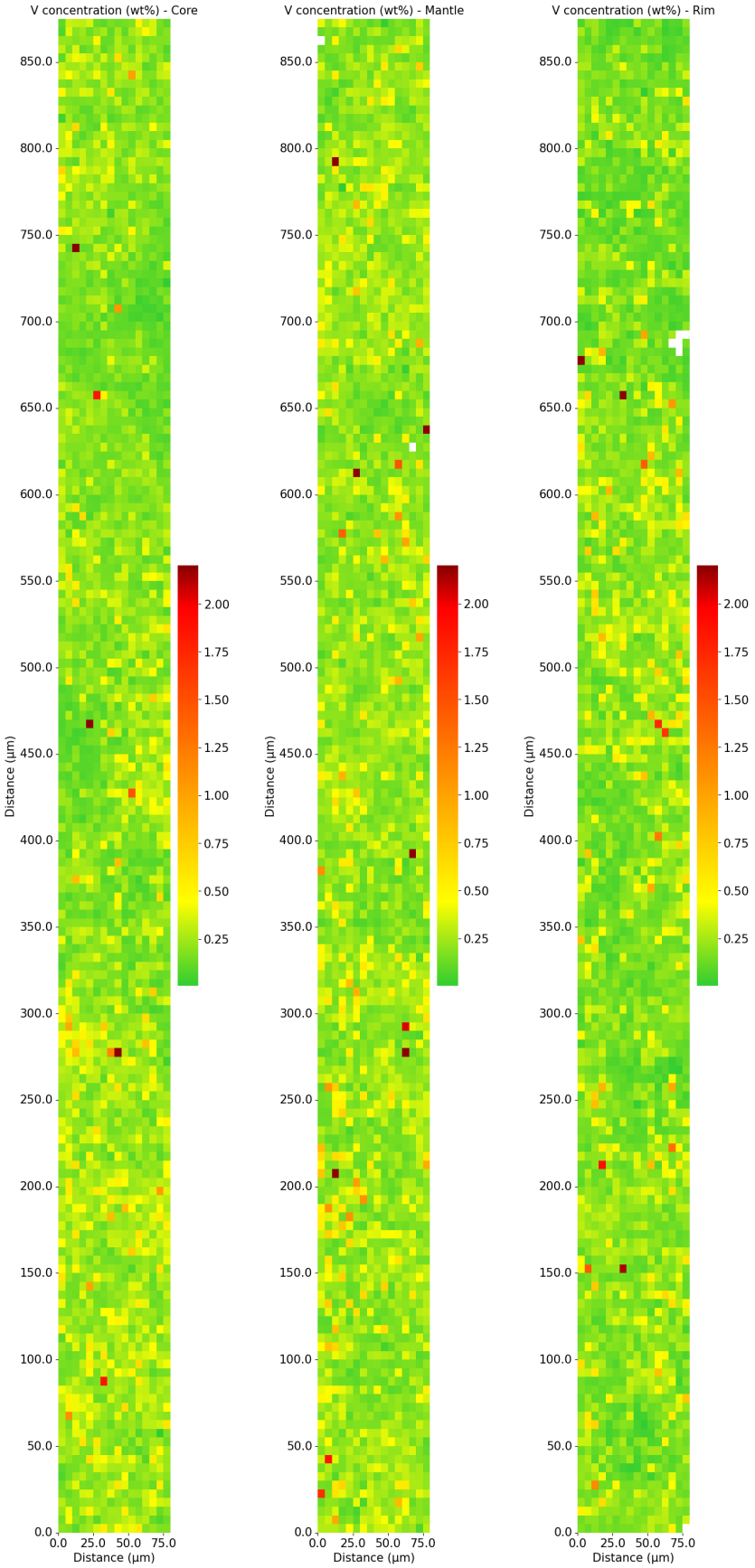

Figure 5.17: LA-IPC-MS maps, with pixel size of 5 μm.

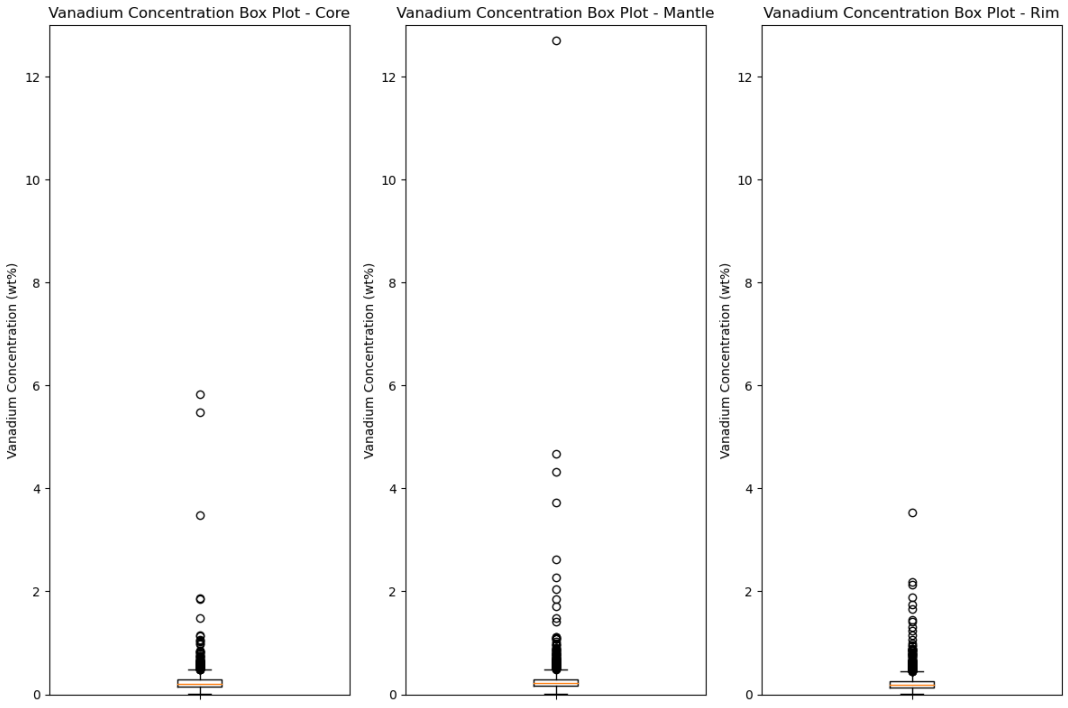

Figure 5.18: Boxplot of LA-IPC-MS data.

5.8. Leaching tests

The leaching tests have been performed in accordance with NEN 7373:2004. This gives insight into how much V the pellets leach and how the pellets' basicity influences the leaching behaviour. The iron ores are assumed not to leach because the V is only present in the spinel structures. Therefore, no leaching test has been conducted on the ores.

Figure 5.19 shows the outcomes of the leaching tests. Figure 5.19a shows the leaching of V, which starts at a high rate but flattens as more leaching substrate is used. This is while the Ca and Si leach proportionately to the amount of used leachate, as shown in Figure 5.19b and 5.19c. So, initially, V leaches relatively more than Ca, but finds an equilibrium at some point. This is also shown in Figure 5.19d, where the ratio of leached V over leached Ca is plotted.

The figures also show pellet 5177, which has a high B_2 pellet, leaches more Ca and V than pellet 5171, which is low in B_2. This is logical for the leaching rate of Ca since less Ca is present in the low B_2 pellets. In Subsection 2.3.2 and Section 5.5, it has been shown that there is a relation between the amount of V present in the melt and the Ca content. This explains why the low B_2 is leaching less V compared to the high B_2 pellet. For Si, this difference between the pellets is less, which indicates that the total glass content that leaches is about the same.

For each test, 10 l of leachate per kg of dry pellet is used. Because of this small amount, only a fraction of V will be leached. Table 5.16 shows the amount of V in one kg of pellets and how much is leached from this amount. In total, 0.018 wt% of the V is leached from this sample.

Table 5.16: Amount of V present in pellet 5171 and amount V from that pellet leached in leachate.

Element	Leached	In pellet	% leached
	mg/kg		
V	24	1300	0.018
Ca	276	12100	0.023
Si	162	14200	0.011

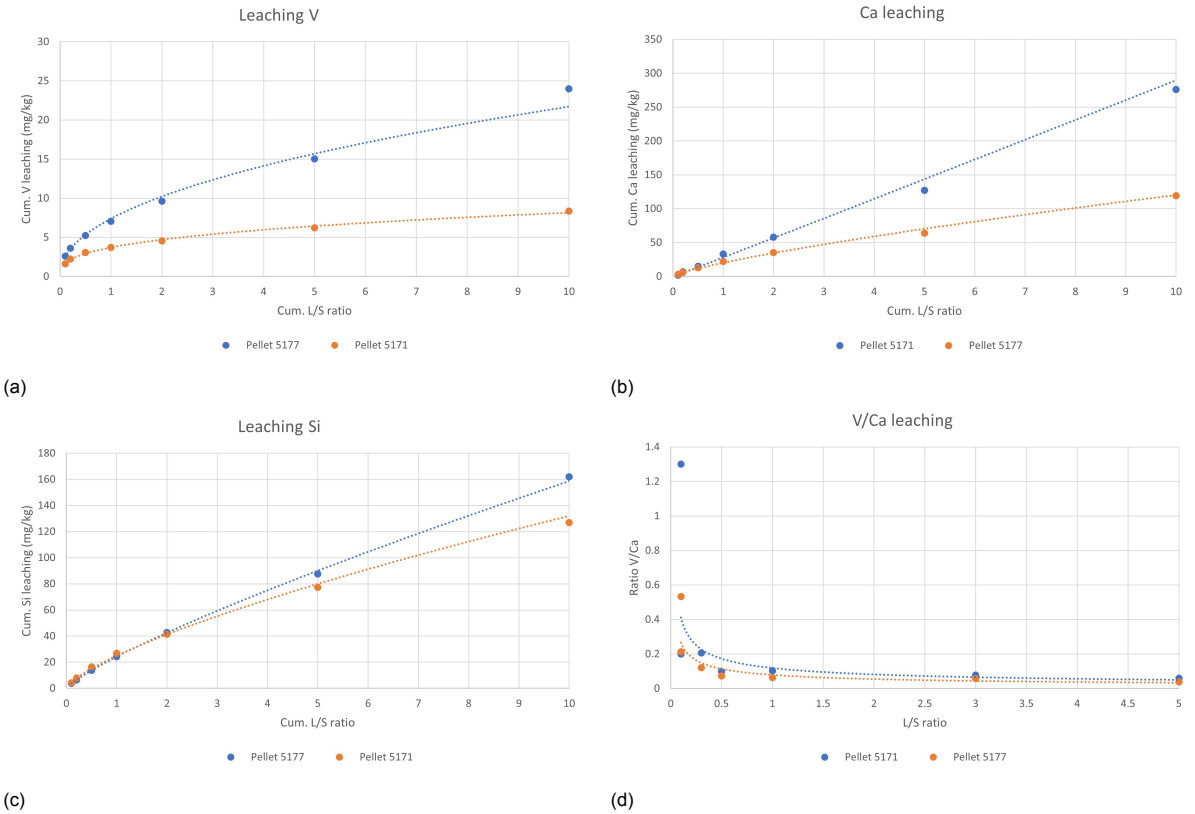

Figure 5.19: Results of leaching tests on pellets 5177 and 5171: (a) leaching V, (b) leaching Ca, (c) Leaching Si, and (d) ration leaching V/Ca.

6

Discussion

This discussion will connect all the results of this research, give an interpretation of it, and discuss the outcomes. This is done by first summarising the important findings from the literature review and the results of the tests. Then, the model is given, which connects the results. The outcomes of the chemical composition and phase abundances are validated with a mass balance. Then, the limitations of this research are discussed. Finally, this chapter highlights a possible way to prevent the leaching of V from the pellets when stored.

6.1. Summary

This research tests the hypothesis that the host phase for V in iron ores changes the agglomeration process to a phase susceptible to leach V. This research is limited to the pelletization process of agglomerating iron ores.

The specific objectives of this thesis are:

- To identify the main host phase of V and other major phases present in the pellets and input materials using SEM-EDS and XRD.
- To quantify concentrations of V in major phases of the pellets and input materials, using SEM-EDS, XRF and LA-IPC-MS.
- To identify the phases in iron pellets that leach V, using the leaching tests.
- To determine the key process parameters that primarily influence the distribution of V and the leaching potential of the fired pellets.

The XRF data in Section 3.2 shows only V detected in the IOA ores used for this research and not in any other input materials. Although XRF can detect trace elements up to ppm order of magnitude, there might still be phases containing V in the other input materials because the used XRF device has not been calibrated for V and is thus unreliable (Potts & Webb, 1992). However, no other phases containing significant concentrations of V were discovered during the SEM-EDS analysis of the input materials. Still, rare phases might be present with very low concentrations and, therefore, are neglectable.

SEM-EDS data shows that the iron oxides in the OIA ores, which, according to XRD, consist almost entirely out of magnetite phase, contain about 0.3 to 0.4 wt% oxide V_2O_5.

The EDS maps show that high concentrations of V are present in the intergranular melt phase after firing. The point analysis supports these EDS maps and shows that the highest concentrations of V are present in the melt, but low concentrations of V remain in the iron oxides. In the magnesioferrite, the V has almost entirely been replaced with Mg in the spinel structure. Therefore, there is not one main host phase for V. The most important one is the melt phase, which hosts the highest concentrations of V but, according to the PARC analysis, is relatively small in volume compared to the iron oxides, where the glass phase accounts for about 4 area% and iron oxides about 90 area%. According to the XRD data and microscopic images, the most dominant iron oxide in the pellet is hematite.

The XRD results, in Section 5.6, show no other significant phases than hematite and magnetite crystal structures in the pellets. This amorphous content can mainly be linked to the melt phase, but other minor phases, which remain below the detection limit of 0.5 wt%, can also be part of this amorphous content. In Subsection 2.2.4, the melt phase is described as having a glass structure, which is amorphous. The pinhole traverse analysis shows about the same area % melt as the XRD result of amorphous content.

Statistical data of the point analysis in Section 5.5 shows a difference in the V concentrations in the melt between the pellets with a high and a low B_2. An explanation for this can be found in Subsection 2.3.2, where Bergman (1988) shows a relation between the optical basicity of a melt phase and the V capacity. The higher the B_2 of a pellet, due to the addition of flux materials, the higher the optical basicity; thus, the more V will be present in the melt. A positive correlation exists between the Ca and V content, but the correlation coefficient is in the range of weak to moderate. More evidence for this relation is found in the same correlation for the LA-ICP-MS data in Section 5.7. A strong correlation will probably be impossible to see because the concentrations of the glassy melt phase are very inhomogeneous. For example, Section 5.5 shows that near olivine flux particles, the concentration of V_2O_5 in the melt varies from 0 to 0.5 wt% oxide, which is much lower than the average of the 3.22 wt% oxide in pellet 5177 while the melt still contains CaO. This has probably to do with the olivine dissolving throughout the firing process, forcing the melt that extracted V from the iron oxides to stream further away. So, the fact that there is a correlation between the Ca and V content in the melt and that the melt in the pellet with high B_2 shows higher V concentrations than the pellets with low B_2 shows that the optical basicity, as described by Bergman (1988), is a critical condition for the transfer of V from the iron ores to the melt phase.

Another important parameter influencing the distribution of V in pellets is the oxygen fugacity, as described in the literature review, Subsection 2.3.2. This is a measurement of the available oxygen during firing around the material. The amount of oxygen determines the valence state of V and whether it is compatible with staying in the iron oxides.

The literature review Subsection 2.2.5 shows that the temperature influences the microstructure and mineralogy of the pellets. Increasing the firing temperature, the flux and gangue material react more with the iron oxides, forming secondary phases like the melt and magnesio ferrites. This will influence the amount of V extracted from iron oxides, as it needs a melt phase to extract it. Note that the proper amount of sintering and slag phase in the pellet is required to meet the blast furnace requirements as listed in Subsection 2.2.1, like a high CCS and high softening temperatures at a narrow range. Hence, the pellets always need to be fired to a certain point.

According to SEM-EDS data, the V concentrations in the melt are about 0.7 wt% oxide for the low B_2 pellets and about 3.2 wt% oxide for the high B_2 pellets. Unfortunately, the spot size for the LA-ICP-MS is too large to capture only the melt phase and, therefore, gives no results.

The leaching results in Section 5.8 show that the elements V, Ca and Si are present in the melt phase leach in water. This implies that the melt phase causes the leaching of V. Unfortunately, no other data is available on a broader range of elements, which can then be linked to other phases. In addition, only a small amount of leachate is used, so insufficient V is being leached during the test to compare the V concentrations in the melt before and after the test. Different substances with different pH could enhance the leaching of V, but this is not an issue as the problem is that pellets are stored outside and can be exposed to only rainwater.

The leaching results also show a different leaching rate between the high and low B_2 pellets of V and Ca, while for Si, this difference is much smaller. This indicates that the leaching rate of the melt phase is the same, but it confirms that the melt containing higher concentrations of Ca also contains higher concentrations of V.

The pellet 9999, produced by an external party but with the same iron ore, showed a similar microstructure and V content in the melt as the pellet 5171.

6.2. Model

Iron ore is usually too fine to use directly in the BF. Therefore, the ores need to be agglomerated, and one method to do this is pelletization. For this process, varying amounts of fluxes, which are Mg and Ca rich sources, bentonite, and cokes are added to the iron ores. This blend is used to produce small spherical-shaped balls of 10 - 16 mm diameter, which are indurated to create porous and strong

pellets. The induration causes flux and gangue materials to react with the iron oxides. The higher the temperatures and lower the concentration of O_2 in the environment, the more secondary phases, like magnesio ferrites and melt, are formed.

Iron ores can contain low concentrations of V, mostly in valence start V^{3+}, depending on their origin. For magnetites, the V is hosted in the spinel structure of the ore. During the induration, the melt phase forms between the iron particles. At these temperatures, the V is transferred from the spinel structures to the melt phase, but two parameters control the amount. The first parameter is the fO_2.The higher the concentration of O_2 in the environment, the more V^{3+} can be converted to V^{5+}, making it incompatible with the spinel and will be transferred to the melt. The second parameter is the optical basicity, which is controlled by the amount of flux material present. The Ca sources are primarily causing this effect; as the concentration of this element increases, the concentration of V increases. The V, which is not transferred to the melt, remains in the spinel structures.

These parameters do not affect the area around olivine particles, an important source of Mg. The Mg reacts with iron oxides, forming magnesio ferrites. These magnesio ferrites have much lower concentrations V than the iron oxides, indicating the V is mostly substituted for Mg. The olivine starts dissolving at higher temperatures than the limestone fluxes; therefore, these magnesio ferrites occur mostly locally around the olivine particles, which often do not completely dissolve. As the olivine keeps slowly dissolving, the melt with the V is replaced by fresh melt, and this is why the melt near an olivine particle contains much lower concentrations than elsewhere.

The only phases containing V are the melt and iron oxides. V^{3+} in the iron oxides is insoluble to water, leaving the glassy melt phase the culprit for the leaching of V.

6.3. Mass balances

To validate the outcomes of this research, a mass balance calculation was performed on pellet 5177. The principle of the mass balance is the conservation of mass. In other words, the mass that goes in must be equal to the mass that comes out. If these are equal to each other, then it must mean that the outcomes of this thesis are correct and that no significant V bearing phases are missed. This equation requires the following input: phase abundances, chemical compositions, and the densities of different phases.

The magnetites are hoisting the V before induration. The XRD data shows that OIA ores contain about 96.3 wt % magnetite. In the pellet blend, 97.1 wt % IOA ores is used. This makes a magnetite content of about 94 wt % in the pellet. The results of the SEM-EDS on the iron ores show that the magnetites contain about 0.3 to 0.4 wt% oxide of V_2O_5. Therefore, a composition of 0.35 wt% oxide V is assumed.

After induration, two phases hoist the V: the iron oxide and melt. Most magnetite has been oxidised to hematite, except for some cores. Therefore, hematite is used for the iron oxides in this calculation. PARC shows that the phase abundance of the iron oxides is about 89 %, and SEM-EDS data shows that hematite has a V_2O_5 content of about 0.19 wt% oxide. The phase abundance for the melt is 6.1% and contains 3.1 wt% oxide of V_2O_5.

The densities for the magnetite and hematite phases are respectively 5.17 and 5.30 g/cm^3. The melt phase is not of a fixed composition and has a range of possible densities. Therefore, an assumption is required about the average chemical composition of the melt phase, which can be used to calculate the density using the glass density model. This glass density model is described in a paper published by Fluegel (2007). The problem is that the measured compositions for Si and Fe are outside the limits that are described for the model, so has the Si content be between 40 and 87 mol% and the Fe content below 10 mol%, but since there is only the need to approximate the density this is still the best method. The equation to calculate the density of the glass is given in Equation 6.1. Based on a Si content of 29 mol%, Fe content of 26 mol%, Ca content of 34 mol%, Mg content of 2 mol%, and Al content of 1.7 mol%, the density of the glass is approximately 3.7 g/cm^3.

$$\text{Density} = b_0 + \sum_{i=1}^{n}\left[b_i C_i + \sum_{k=i}^{n}\left(b_{ik} C_i C_k + \sum_{m=k}^{n} b_{ikm} C_i C_k C_m\right)\right] \tag{6.1}$$

where,

b-values: model coefficients for different elements

C-values: glass component concentrations in mol%

The outcomes for the mass balance is a V_2O_5 content of 0.33 wt% before induration and 0.31 wt% after induration. This difference is less than 10 %, and therefore, the quantitative results of this research seem accurate. Consequently, it is safe to say that there are no other major phases present other than the glass and iron oxide in the pellet containing high concentrations of V.

6.4. Limitations

6.4.1. Oxigen fugacity

Extensive research has been done on the influence of fO_2 on the partition of V in melt and crystal structures (Karner et al., 2006; Mallmann & O'Neill, 2009; Righter et al., 2006; Righter et al., 2011; Shearer, McKay, et al., 2006; Shearer, Papike, et al., 2006). However, this research does not give a clear insight into this influence, but it is assumed to be an important factor. This is because it is likely that in the presence of enough O_2 and a high temperature, the V oxidises and, therefore, the valence state changes, which makes it incompatible with the spinel structure. In addition, the mineralogy of the pellet changes as magnetite oxidises to hematite, which will affect the V compatibility. However, Subsection 2.2.5 also shows that the fO_2 also influences the amount of melt phase. The more reduced the environment the more melt is produced. This higher quantity might extract more V in total but with a lower content than in a more oxidised environment. This could not be researched because the pellets had already been prepared before starting this research, so there was no opportunity to control the firing conditions.

The influence of fO_2 could be researched by firing the same blend of green pellets in a controlled environment at the same temperature but with varying O_2 levels during firing. The SEM-EDS content of V_2O_5 could have been measured in the melt, and these results could have been compared.

6.4.2. Leachning method

The leaching test is performed according to the NEN 7373:2004, as described in Section 4.3, which is a good and fast method to show if a material has an environmental impact. The results must remain below a specific threshold to ensure safe usage. However, the results of this research have two implications.

The first implication is that, as described in Section 6.1, the test should have been performed over a broader range of elements. The test has only been done on the elements Si, Ca, and V, but the elements Fe and Mg should have been included. Including this, a better understanding of which phases are leaching would have been created. In addition, besides only leaching the pellets, the IOA ores should have been tested. Probably, the iron oxides do not leach V, but evidence is lacking.

The second implication is that only small amounts of leachate are used for these tests. Only 10 l of leachate per kg of dry material is used, which leaches only a tiny amount of V. It would have been beneficial for this research if the material had been continuously leached over a long duration with larger amounts of leachate to prevent it from being saturated. This way, significant amounts of V could have been leached so that the material could have been investigated before and after the test to see any substantial changes in chemical composition or that some phases mainly had been dissolved.

6.4.3. Dilution of melt phase measurements

It is already briefly discussed in Section 5.5, but if the spot size of the SEM-EDS is larger than the width of a phase, penetrates deeper than the depth of a phase, or the measurement is taken at the edge of a phase, the signal in the SEM-EDS of the melt phase can be diluted with the adjacent phase.

So, occasionally, the point analysis of the melt phase is diluted with iron oxide. This is shown in the point analysis in Figure 6.1 with corresponding Table 6.1. The content reaches almost 60 wt % oxide Fe_2O_3, which would unlikely be found in a melt phase and dilutes the other elements. The implication is that not all measurements of the melt phase are accurate, as the melt phase is often very narrow

between the iron oxide parts. To solve this problem, a filter has been applied to the data, where the Fe_2O_3 content of the melt should be below 40 wt% oxide to be included in the statistics.

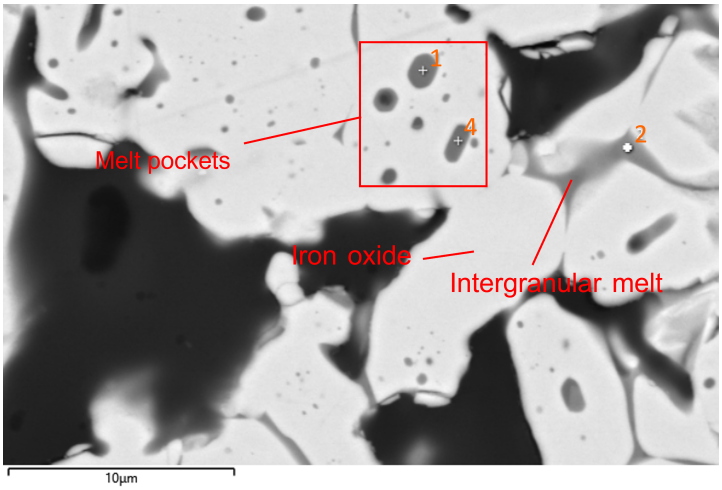

Figure 6.1: Backscatter image of SEM point analysis to show the dilution of iron oxide in the melt phase.

Table 6.1: SEM point analysis of melt in wt% oxide corresponding to Figure 6.1, showing the dilution of iron oxide in the melt phase.

Element	1	4	2
	Melt pocket		Intergranular melt
Na_2O	1.05	0.90	0.69
MgO	4.73	3.03	8.74
Al_2O_3	1.71	1.74	1.54
SiO_2	30.85	29.75	29.15
P_2O_5	0.53	0.24	0.34
SO_3	0.14	0.03	0.05
K_2O	0.31	0.29	0.01
CaO	10.27	10.43	12.29
Ti_2O_3	0.13	0.07	0.12
V_2O_5	0.45	0.44	0.14
Mn_3O_4	0.18	0.14	0.11
Fe_2O_3	49.55	52.86	46.71

6.5. Preventive leaching

This section presents the possible measures for TSN to prevent the leaching of V in the groundwater by industrially leaching the pellets before they are used in the BF or stored on the stockpile outside. This would prevent the leaching of V in the groundwater and change V from a burden to a valuable resource. As the European Union lists V as a Critical Raw Material, TSN could work with the European Union to set up this project. For the European industry, it will be interesting to diversify their supply of V and sign long-term contracts. TSN can also use the extracted V to produce steel alloys and address new markets.

The primary source of mined V is titaniferous magnetite. The V is locked in the spinel structure, which is stable, and so it is hard to extract V directly from magnetite concentrates (Gao et al., 2018). Therefore, other methods have been investigated. Often, these methods involve a roasting process with additives, followed by a leaching process. Table 6.2 shows different techniques for extracting V, which could potentially be applied to the pelletising process to extract V. This table shows the method used for roasting and leaching the pellet, the source material, the optimal duration of the processes, and the efficiency.

Table 6.2: Different V leaching methods.

Roasting method	Leaching method	Source	Reported (optimal) roasting time	Reported (optimal) leaching time	Vanadium leaching efficiency	Reference
Salt free roasting	Sulfuric acid leaching	Pellet	3 h	6 days	60.3 %	Luo, Che, Wang, et al. (2021)
-	Sodium alkaline leaching	Steel slag	-	3 h	85.6 %	Wan et al. (2021)
-	Sodium alkaline leaching	Magnetite concentrate	-	4 h	59.1 %	Zheng et al. (2019)
Potassium salt roasting	Sulfuric acid leaching	Magnetite concentrate	1h	1.5 h	71.4 %	R. Li et al. (2018)
Sodium salt roasting	Water leaching	Steel slag	2 h	20 min	87.9 %	H.-Y. Li et al. (2015)
Sodium salt roasting	Water leaching	Pellet	10 min	2 h	71.1 %	Zhang et al. (2021)
Calcium salt roasting	Sulfuric acid leaching	Pellet	3 h	6 days	89.0 %	Luo, Che, Cui, et al. (2021)
Calcium hydroxide roasting	Sulfuric acid leaching	Pellet	2 h	3 days	74.5 %	Y. Li et al. (2023)

Potassium salt roasting with sulfuric acid leaching is an effective method to leach V. Nevertheless, potassium is an element that decreases the efficiency of the BF and, therefore, is unsuitable to add to the pellet blend. Another effective way is to apply the sodium salt-water leaching method, but when roasting, this produces harmful HCl, SO_2 and Cl_2 gasses and therefore is unsuitable (Wang et al., 2014). Alkali leaching processes have been described as environmentally friendly, but so far, they have only been applied to steel slags, and magnetite concentrates (Wan et al., 2021; Zheng et al., 2019). The reported efficiency of alkali leaching on the concentrates is also relatively low, and pressure leaching was applied, which is unsuitable for use on pellets.

The most exciting method to extract V from pellets is by applying calcium roasting succeeded by acid leaching, as described in a paper of Y. Li et al. (2023). With the production of green balls, $Ca(OH_2)$ is added to the blend. After the sulfuric acid leaching, a secondary induration is required to remove the remaining sulfur from the pellet. In addition, after the leaching phase, the pellet's remaining strength is low, which needs to be upgraded by induration to use in the BF.

6.6. Reflection

The hypothesis which started this research is *'The host phase of V in iron ores changes during the agglomeration process to a phase susceptible to leaching'*. Section 2.5 at the end of the Literature Review indicated that the V comes from the iron oxides and is partially transferred to the secondary melt phase. Two parameters, the fO_2 during firing and the optical basicity of the melt, are suggested based on the literature influencing the distribution of V in the pellet. Based on the outcomes of the analysis, the hypothesis can be substantiated, and the gap in the literature can be closed.

SEM-EDS on the input materials has shown that the magnetite iron oxide is the only phase bearing significantly high concentrations of V. The SEM-EDS data of a representative magnetite grain before induration vary between 0.29 and 0.41 wt% oxide, and after induration, the mean of the iron oxides is 0.19 wt% oxide. This drop in V content confirms the magnetite to be the source of V in the pellet. The SEM-EDS data shows that this V is transferred to the secondary melt phase. So, the main host phase of V before induration is the magnetite, and after induration, this shifts to the iron oxide, which are the magnetite and hematite phases, and the secondary melt phase. With this, the gap in the literature is closed because it was already known what reactions occur during induration, but now it is also known what this does with the distribution of V.

This thesis provides evidence that the optical basicity influences the distribution of V. First, the SEM-EDS data show a significant difference in V content in the melt between the pellets with a high and low B_2. This means that if more fluxes are used in the pellet blend, the V concentrations are higher in the melt. Secondly, it has been shown that there is a correlation between the Ca and the V content in the blend. The higher the Ca content, the higher the optical basicity of the melt and the more V is detected. Finally, it has been shown that the pellet with a high B_2 pellet leaches more V and Ca than the low B_2 pellet, while the total amount of melt that is leached is assumed to be about the same because of the small difference in the leaching rate of Si between the pellets. For the other parameter, the fO_2, this thesis cannot provide evidence that this influences the V distribution. This is because the pellets should have been firing under different reduced environments to show the differences. The literature is quite convincing that this must have an influence, as the diagrams clearly show a relationship between the fO_2 and the partitioning of V in the melt. However, the literature also contradicts each other, as Subsection 2.2.5 states that in the reduced core of the pellet, more secondary melt is present and less flux and gangue than in the oxidised rim. The quantity of melt might have a more significant influence on the extraction of V from the iron oxides than the content V the melt can contain. In other words, there might be more V extracted in a higher quantity of melt with a lower V content than in a lower quantity

with a high content.

As stated in Subsection 6.4.2, the leaching tests could have been performed differently to get more insights into the leaching behaviour. However, it shows that V, Ca, and Si, major components in the melt phase, are leaching. Since no other phase is detected in the pellet with these elements, and if these existed, they must be so rare to have no impact, the secondary melt phase must cause the leaching of V from the pellets. The only issue is there might be another phase leaching, but besides the iron ores, which are assumed not to leach, no other phases are detected with significant V contents, which makes it very unlikely.

This thesis focussed on one type of iron ores. This is not a limitation of this thesis, as there was also the possibility of including pellets produced with iron ores containing hematite. The V concentrations were so low that it would not have been interesting to see what the induration process does with the distribution. Also, a pellet produced by an external party has been analysed. The pellet blend is unknown for commercial reasons, but the same iron ores are used. The microstructures observed were comparable to those of the pellet in the low B_2 pellet batch, and also, the V content in the melt is comparable. So probably, this pellet is also low in B_2. This comparison validates the outcomes of this thesis and makes this research also applicable to other pellets produced with magnetite ores.

7

Conclusions and recommnedations

This study investigates how the distribution of V in iron ores changes when processed into pellets and how this affects the leaching potential. The main objective of this thesis is to explore how the distribution of V in iron ores alters during pelletization and assess the impact of these changes on the leaching potential of V. A comprehensive lab program has been developed to research this, including using SEM-EDS, XRD, and LA-IPC-MS techniques. IOA iron ore pellets, which are relatively high in V concentrations, have been analysed with two different blends, one with a high and one with a low B_2. The SEM-EDS is used, besides point analysis, to scan the samples from the rim to the pellet's core. With the software PARC, this data is used to create a model which calculates the phase abundances along this pinhole traverse. A third party has performed leaching tests, measuring the concentrations of V, Ca, and Si.

Iron ore is the main contributor to V concentrations in the pellet. In the IOA ores used for this study, the V is hosted in the magnetite spinel structures as a trace element. Although the V is present in low concentrations, the iron ores are the major component in the blend.

In the pellet, the main phases containing V are the melt phase and the iron oxides, primarily hematite, except for some magnetite pellet cores. The melt phase contains the highest concentrations of V but is much less abundant than the iron oxides. The V concentrations in the iron oxides of the fired pellets' are lower than those in the original IOA ores. Another significant phase in the pellets is magnesioferrite, which has a spinel structure but contains negligible concentrations of V. Further rare phases are encountered, such as rutile, quartz, and forsterite.

The V concentrations in the secondary melt differ for pellets with a high and low B_2. The concentration for respectively high and low B_2 pellets is 3.2 and 0.7 wt% oxide V_2O_5. The mean concentration in the iron oxides is only 0.2 wt% oxide V_2O_5. This is still relevant, taking about 90 % of the area in a cross-section of the pellet, while the melt covers only 3 to 6 %. The concentration of V dropped during the induration process, as before firing, the magnetite contains about 0.3 to 0.4 wt% oxide V_2O_5.

It has been shown that the secondary melt phase leaches V. The V hosted in the iron oxide will be stable and will not contribute to leaching. If another phase is still leaching, this remained undetected with the SEM-EDS and, therefore, must be rare. Hence, this phase will be insignificant.

The critical process parameters influencing the distribution of V are the fO_2 and the optical basicity of the melt. The optical basicity is influenced by the pellet's B_2. The melt in the pellets with a low B_2 showed significantly lower concentrations of V and, as stated in the previous paragraph, leaches significantly less V than the pellets with a high B_2.

To conclude, during the induration of the pellets, a secondary melt phase is formed. Depending on the B_2 of the pellet and the fO_2, the V is partially transferred from the iron oxides to this melt phase, and the remaining stays in the iron oxide. The melt phase has a high V concentration but low abundance, while the iron oxides are low in concentration but have a high abundance. This glass phase is likely leaching V when in contact with a leachate.

Pellets stored outside and exposed to water will start leaching V if they contain this element. If nothing is done to prevent this, this V will end up in the groundwater. The melt phase is causing the leaching. This implies that nothing can be changed in the pellet's production process because the melt phase is needed to acquire the pellet's requirements for use in the BF, such as its required strength

and reducing properties. So, the solution to prevent the leaching of V is not in the production process but must be found elsewhere.

The following recommendations are given to further elaborate on this thesis:

1. Now is understood how the distribution of V develops in the pellet during the production process, further research is required to ensure that the leaching of V in the groundwater can be minimised or ideally avoided. This is not only a technical issue, but the business side of the story should also be included. The most obvious solution would be to put a roof over the stockpile to prevent contact between pellets and rainwater. Still, the V, and maybe other valuable metals like Cr, will not be utilised as they end up in the slags. This is while the European Union lists V as a critical raw material because this metal is much needed in different industries while the supply is mainly dependent on two countries. Therefore, a TSN could apply industrial leaching to extract the V before the pellets are stored, but this requires further research. This thesis has already suggested some options that could be used for further research.
2. More research should be conducted on the leaching behaviour of the pellets. Subsection 6.4.2 showed the limitation of the leaching results of this research. It is proposed to perform leaching tests on a broader range of elements and include these tests on the iron ores. Also the leaching should be done over a longer duration, without the pellets being crushed beforehand. This way, a more realistic approach is realised, and the pellets can be analysed with the SEM-EDS before and after the leaching process to compare the V contents in the melt.
3. Another topic for further research is the influence of the fO_2 on the distribution of V in the pellets. For this, a different set-up is required than in this research. To do this the green pellets should be fired under different reduced environments to see what influence the O_2 is on the distribution of V.
4. This research has only examined the pellets of agglomerated iron ores, but it could be extended to research the sinter BF feed. This research can serve as a guideline for conducting this new study, but the sinter material will contain more complicated phases, creating different challenges.

Bibliography

Allibert, M. (1995). *Slag atlas* (2nd ed) [OCLC: 36859350]. Verlag Stahleisen.

Balan, E., De Villiers, J. P., Eeckhout, S. G., Glatzel, P., Toplis, M. J., Fritsch, E., Allard, T., Galoisy, L., & Calas, G. (2006). The oxidation state of vanadium in titanomagnetite from layered basic intrusions. *American Mineralogist*, *91*(5-6), 953–956. https://doi.org/10.2138/am.2006.2192

Ball, D., Dartnell, J., & Davison, J. (1973). *Agglomeration of iron ores.* American Elsevier.

Bekker, A., Slack, J. F., Planavsky, N., Krapež, B., Hofmann, A., Konhauser, K. O., & Rouxel, O. J. (2010). Iron Formation: The Sedimentary Product of a Complex Interplay among Mantle, Tectonic, Oceanic, and Biospheric Processes*. *Economic Geology*, *105*(3), 467–508. https://doi.org/10.2113/gsecongeo.105.3.467

Bergman, Å. (1988). Representation of Phosphorus and Vanadium Equilibria between Liquid Iron and Complex Steelmaking Type Slags. *Transactions of the Iron and Steel Institute of Japan*, *28*(11), 945–951. https://doi.org/10.2355/isijinternational1966.28.945

Bhagat, R. P. (2019). *Agglomeration of Iron Ores* (1st ed.). CRC Press. https://doi.org/10.1201/9781315269504

Bilim, C., Atiş, C. D., Tanyildizi, H., & Karahan, O. (2009). Predicting the compressive strength of ground granulated blast furnace slag concrete using artificial neural network. *Advances in Engineering Software*, *40*(5), 334–340. https://doi.org/10.1016/j.advengsoft.2008.05.005

Boucher, M.-È., & Wilhelmy, J.-F. (2007). *Corem Virtual Atlas of Iron Ore Pellets* (1.0) [personal communication].

Canil, D. (1999). Vanadium partitioning between orthopyroxene, spinel, and silicate melt, and the redox states of mantle source regions for primary magmas. *Geochimica et Cosmochimica Acta*, *63*, 557–572. https://doi.org/10.1016/S0016-7037(98)00287-7

Chen, L., Wang, Z., Qin, Z., Zhang, G., Yue, H., Liang, B., & Luo, D. (2021). Investigation of the selective oxidation roasting of vanadium□iron spinel. *Powder Technology*, *387*, 434–443. https://doi.org/10.1016/j.powtec.2021.04.009

Clarijs, C. (2022). TSN Company presentation [personal communication].

Darken, L. S. (1948). Melting Points of Iron Oxides on Silica; Phase Equilibria in the System Fe-Si-O as a Function of Gas Composition and Temperature. *Journal of the American Chemical Society*, *70*(6), 2046–2053. https://doi.org/10.1021/ja01186a019

Dehn, J., & McNutt, S. R. (2015). Chapter 74 - Volcanic Materials in Commerce and Industry. In H. Sigurdsson (Ed.), *The Encyclopedia of Volcanoes (Second Edition)* (pp. 1285–1294). Academic Press. https://doi.org/10.1016/B978-0-12-385938-9.00074-2

de Villiers, J. P. R., & Lu, L. (2022). Chapter 3 - Quantitative XRD analysis and evaluation of iron ore, sinter, and pellets. In L. Lu (Ed.), *Iron Ore (Second Edition)* (pp. 109–126). Woodhead Publishing. https://doi.org/10.1016/B978-0-12-820226-5.00004-5

Domingo, J. L. (1996). Vanadium: A review of the reproductive and developmental toxicity. *Reproductive Toxicology*, *10*(3), 175–182. https://doi.org/10.1016/0890-6238(96)00019-6

Exner, H. E., & Weinbruc, S. (2004). 31. Scanning Electron Microscopy. In *ASM Handbook, Volume 09 - Metallography and Microstructures*. ASM International. https://app.knovel.com/hotlink/pdf/id:kt007O7UQ2/asm-handbook-volume-09/scanning-electron-microscopy

Fluegel, A. (2007). Global Model for Calculating Room-Temperature Glass Density from the Composition. *Journal of the American Ceramic Society*, *90*(8), 2622–2625. https://doi.org/10.1111/j.1551-2916.2007.01751.x

Foerster, H., & Jafarzadeh, A. (1994). The Bafq mining district in central Iran; a highly mineralized Infracambrian volcanic field. *Economic Geology*, *89*(8), 1697–1721. https://doi.org/10.2113/gsecongeo.89.8.1697

Fricker, M. B., & Günther, D. (2016). Instrumentation, Fundamentals, and Application of Laser Ablation-Inductively Coupled Plasma-Mass Spectrometry. In L. Dussubieux, M. Golitko, & B. Gratuze (Eds.), *Recent Advances in Laser Ablation ICP-MS for Archaeology* (pp. 1–19). Springer. https://doi.org/10.1007/978-3-662-49894-1_1

Frietsch, R., & Perdahl, J.-A. (1995). Rare earth elements in apatite and magnetite in Kiruna-type iron ores and some other iron ore types. *Ore Geology Reviews*, *9*(6), 489–510. https://doi.org/10.1016/0169-1368(94)00015-G

Gao, H., Jiang, T., Xu, Y., Wen, J., & Xue, X. (2018). Change in phase, microstructure, and physical-chemistry properties of high chromium vanadium slag during microwave calcification-roasting process. *Powder Technology*, *340*, 520–527. https://doi.org/10.1016/j.powtec.2018.09.045

Geerdes, M., Chaigneau, R., Kurunov, I., Lingiardi, O., & Ricketts, J. (2015). *Modern blast furnace ironmaking: An introduction* (Third edition). IOS Press, under the imprint of Delft University Press. Retrieved April 6, 2023, from https://ebookcentral-proquest-com.tudelft.idm.oclc.org/lib/delft/detail.action?docID=2033826

Grohol, M., & Veeh, C. (2023). *Study on the critical raw materials for the EU 2023: Final report*. Publications Office of the European Union. Retrieved November 12, 2023, from https://data.europa.eu/doi/10.2873/725585

Guo, Y., Liu, K., Chen, F., Wang, S., Zheng, F., Yang, L., & Liu, Y. (2021). Effect of basicity on the reduction swelling behavior and mechanism of limestone fluxed iron ore pellets. *Powder Technology*, *393*, 291–300. https://doi.org/10.1016/j.powtec.2021.07.057

Hobson, A. J., Stewart, D. I., Bray, A. W., Mortimer, R. J. G., Mayes, W. M., Rogerson, M., & Burke, I. T. (2017). Mechanism of Vanadium Leaching during Surface Weathering of Basic Oxygen Furnace Steel Slag Blocks: A Microfocus X-ray Absorption Spectroscopy and Electron Microscopy Study. *Environmental Science & Technology*, *51*(14), 7823–7830. https://doi.org/10.1021/acs.est.7b00874

Huang, J.-H., Huang, F., Evans, L., & Glasauer, S. (2015). Vanadium: Global (bio)geochemistry. *Chemical Geology*, *417*, 68–89. https://doi.org/10.1016/j.chemgeo.2015.09.019

Jankovic, A. (2015). 8 - Developments in iron ore comminution and classification technologies. In L. Lu (Ed.), *Iron Ore* (pp. 251–282). Woodhead Publishing. https://doi.org/10.1016/B978-1-78242-156-6.00008-3

Kaja, A. M., Delsing, A., van der Laan, S. R., Brouwers, H. J. H., & Yu, Q. (2021). Effects of carbonation on the retention of heavy metals in chemically activated BOF slag pastes. *Cement and Concrete Research*, *148*, 106534. https://doi.org/10.1016/j.cemconres.2021.106534

Karner, J., Papike, J. J., & Shearer, C. K. (2006). Comparative planetary mineralogy: Pyroxene major- and minor-element chemistry and partitioning of vanadium between pyroxene and melt in planetary basalts. *American Mineralogist*, *91*(10), 1574–1582. https://doi.org/10.2138/am.2006.2103

Knipping, J. L., Bilenker, L. D., Simon, A. C., Reich, M., Barra, F., Deditius, A. P., W□lle, M., Heinrich, C. A., Holtz, F., & Munizaga, R. (2015). Trace elements in magnetite from massive iron oxide-apatite deposits indicate a combined formation by igneous and magmatic-hydrothermal processes. *Geochimica et Cosmochimica Acta*, *171*, 15–38. https://doi.org/10.1016/j.gca.2015.08.010

Lan, C., Zhao, T., Chen, W. T., & Long, X. (2019). Trace elemental modification in magnetite from high-grade metamorphosed BIFs in the southern North China Craton. *Ore Geology Reviews*, *112*, 103019. https://doi.org/10.1016/j.oregeorev.2019.103019

Li, H.-Y., Fang, H.-X., Wang, K., Zhou, W., Yang, Z., Yan, X.-M., Ge, W.-S., Li, Q.-W., & Xie, B. (2015). Asynchronous extraction of vanadium and chromium from vanadium slag by stepwise sodium roasting–water leaching. *Hydrometallurgy*, *156*, 124–135. https://doi.org/10.1016/j.hydromet.2015.06.003

Li, R., Liu, T., Zhang, Y., Huang, J., & Xu, C. (2018). Efficient Extraction of Vanadium from Vanadium–Titanium Magnetite Concentrate by Potassium Salt Roasting Additives. *Minerals*, *8*(1), 25. https://doi.org/10.3390/min8010025

Li, Y., Peng, Z., Wang, Z., Zhu, Y., & Xie, K. (2023). Study on the Properties of Vanadium Pellets Extracted from Vanadium Titanium Magnetite Concentrate by Calcium Roasting and Acid Leaching. *Minerals*, *13*(3), 399. https://doi.org/10.3390/min13030399

Longerich, H. P., Jackson, S. E., & Günther, D. (1996). Inter-laboratory note. Laser ablation inductively coupled plasma mass spectrometric transient signal data acquisition and analyte concentration calculation. *Journal of Analytical Atomic Spectrometry*, *11*(9), 899–904. https://doi.org/10.1039/JA9961100899

Luo, Y., Che, X., Cui, X., Zheng, Q., & Wang, L. (2021). Selective leaching of vanadium from V-Ti magnetite concentrates by pellet calcification roasting-H2SO4 leaching process. *International Journal of Mining Science and Technology*, *31*(3), 507–513. https://doi.org/10.1016/j.ijmst.2021.02.002

Luo, Y., Che, X., Wang, H., Zheng, Q., & Wang, L. (2021). Selective extraction of vanadium from vanadium-titanium magnetite concentrates by non-salt roasting of pellets-H2SO4 leaching process. *Physicochemical Problems of Mineral Processing*, *Vol. 57, iss. 4*. https://doi.org/10.37190/ppmp/138281

Mallmann, G., & O'Neill, H. S. C. (2009). The Crystal/Melt Partitioning of V during Mantle Melting as a Function of Oxygen Fugacity Compared with some other Elements (Al, P, Ca, Sc, Ti, Cr, Fe, Ga, Y, Zr and Nb). *Journal of Petrology*, *50*(9), 1765–1794. https://doi.org/10.1093/petrology/egp053

Meyer, K. (1980). *Pelletizing of iron ores*. Springer.

Meyer, M., Lagoeiro, L. E., Graça, L. M., & Silva, C. J. (2016). Phase and Microstructural Characterization of Iron Ore Pellet and their Relation with Cold Crushing Strength Test. *Mineral Processing and Extractive Metallurgy Review*, *37*(5), 295–304. https://doi.org/10.1080/08827508.2016.1200574

Miliszkiewicz, N., Walas, S., & Tobiasz, A. (2015). Current approaches to calibration of LA-ICP-MS analysis. *Journal of Analytical Atomic Spectrometry*, *30*(2), 327–338. https://doi.org/10.1039/C4JA00325J

Mourao, J., Cameron, I., Huerta, M., Patel, N., & Pereira, R. (2020). Comparison of sinter and pellet usage in an integrated steel plant. https://www.researchgate.net/profile/Jose-Mourao-4/publication/341386739_COMPARISON_OF_SINTER_AND_PELLET_USAGE_IN_AN_INTEGRATED_STEEL_PLANT_1/links/5ebdb9f7299bf1c09abc15c6/COMPARISON-OF-SINTER-AND-PELLET-USAGE-IN-AN-INTEGRATED-STEEL-PLANT-1.pdf

Mousa, E., Wang, C., Riesbeck, J., & Larsson, M. (2016). Biomass applications in iron and steel industry: An overview of challenges and opportunities. *Renewable and Sustainable Energy Reviews*, *65*, 1247–1266. https://doi.org/10.1016/j.rser.2016.07.061

NEN. (2004). NEN 7373:2004 nl. Retrieved October 4, 2023, from https://www.nen.nl/nen-7373-2004-nl-91727

Nystroem, J. O., & Henriquez, F. (1994). Magmatic features of iron ores of the Kiruna type in Chile and Sweden; ore textures and magnetite geochemistry. *Economic Geology*, *89*(4), 820–839. https://doi.org/10.2113/gsecongeo.89.4.820

Palma, G., Reich, M., Barra, F., Ovalle, J. T., del Real, I., & Simon, A. C. (2021). Thermal evolution of Andean iron oxide–apatite (IOA) deposits as revealed by magnetite thermometry. *Scientific Reports*, *11*(1), 18424. https://doi.org/10.1038/s41598-021-97883-3

Panigrahy, S. C., Verstraeten, P., & Dilewijns, J. (1984). Influence of MgO addition on mineralogy of iron ore sinter. *Metallurgical Transactions B*, *15*(1), 23–32. https://doi.org/10.1007/BF02661059

Poojari, M., Vardhan, H., & Jathanna, H. M. (2023). Iron Ore Characterization Techniques in Mineral Processing. *Journal of The Institution of Engineers (India): Series D*. https://doi.org/10.1007/s40033-023-00483-w

Potts, P. J., & Webb, P. C. (1992). X-ray fluorescence spectrometry. *Journal of Geochemical Exploration*, *44*(1), 251–296. https://doi.org/10.1016/0375-6742(92)90052-A

Reich, M., Simon, A. C., Barra, F., Palma, G., Hou, T., & Bilenker, L. D. (2022). Formation of iron oxide–apatite deposits. *Nature Reviews Earth & Environment*, *3*(11), 758–775. https://doi.org/10.1038/s43017-022-00335-3

Reimann, C., & Caritat, P. d. (2012). *Chemical Elements in the Environment: Factsheets for the Geochemist and Environmental Scientist*. Springer Science & Business Media.

Righter, K., Leeman, W. P., & Hervig, R. L. (2006). Partitioning of Ni, Co and V between spinel-structured oxides and silicate melts: Importance of spinel composition. *Chemical Geology*, *227*(1), 1–25. https://doi.org/10.1016/j.chemgeo.2005.05.011

Righter, K., Sutton, S., Danielson, L., Pando, K., Schmidt, G., Yang, H., Berthet, S., Newville, M., Choi, Y., Downs, R., & Malavergne, V. (2011). The effect of fO2 on the partitioning and valence of V and Cr in garnet/melt pairs and the relation to terrestrial mantle V and Cr content. *American Mineralogist*, *96*(8-9), 1278–1290. https://doi.org/10.2138/am.2011.3690

Scarlett, N., & Madsen, I. (2018). Effect of microabsorption on the determination of amorphous content via powder X-ray diffraction. *Powder Diffraction*, *33*, 26–37. https://doi.org/10.1017/S0885715618000052

Schollbach, K., & Laan, S. v. d. (2021). Chapter 3 Microstructure analysis with quantitative phase mapping using SEM-EDS and Phase Recognition and Characterization (PARC) Software: Applied to steelmaking slag. In *Chapter 3 Microstructure analysis with quantitative phase mapping using SEM-EDS and Phase Recognition and Characterization (PARC) Software: Applied to steelmaking slag* (pp. 57–96). De Gruyter. https://doi.org/10.1515/9783110674941-003

Selin, R. (1990). The role of phosphorus, vanadium and slag forming oxides in direct reduction based steelmaking, 1. Retrieved October 2, 2023, from https://elibrary.ru/item.asp?id=6843286

Sharma, R. P. (1979). Vanadium, manganese and iron in the carbonate rocks of the Rohtas formation. *Proceedings of the Indian Academy of Sciences - Section A. Part 2, Earth and Planetary Sciences*, *88*(1), 19–28. https://doi.org/10.1007/BF02910949

Shearer, C., McKay, G., Papike, J., & Karner, J. (2006). Valence state partitioning of vanadium between olivine-liquid: Estimates of the oxygen fugacity of Y980459 and application to other olivine-phyric martian basalts. *American Mineralogist*, *91*(10), 1657–1663. https://doi.org/10.2138/am.2006.2155

Shearer, C., Papike, J., & Karner, J. (2006). Pyroxene europium valence oxybarometer: Effects of pyroxene composition, melt composition, and crystallization kinetics. *American Mineralogist*, *91*(10), 1565–1573. https://doi.org/10.2138/am.2006.2098

Small, J., & Firth, A. (2023). Iron ore pellets and oxidation [personal communication].

Smil, V. (2016). Chapter 6 - Materials in Modern Iron and Steel Production: Ores, Coke, Fluxes, Scrap, and Other Inputs. In V. Smil (Ed.), *Still the Iron Age* (pp. 115–138). Butterworth-Heinemann. https://doi.org/10.1016/B978-0-12-804233-5.00006-3

Strassburger, J. H. (1969). *Blast furnace - theory and practice. Vol. 1.* Gordon; Breach.

Sutton, S., Karner, J., Papike, J., Delaney, J., Shearer, C., Newville, M., Eng, P., Rivers, M., & Dyar, M. (2005). Vanadium K edge XANES of synthetic and natural basaltic glasses and application to microscale oxygen barometry. *Geochimica et Cosmochimica Acta*, *69*(9), 2333–2348. https://doi.org/10.1016/j.gca.2004.10.013

Tupkary, R. H. (2018). *Modern iron making handbook*. Mercury Learning & Information. Retrieved April 6, 2023, from http://app.knovel.com/hotlink/toc/id:kpMIMH0001/modern-iron-making?kpromoter=marc

van der Wilt, C. J. (2000). *Het saneringsbevel in de Wet bodembescherming*. Alphen aan den Rijn-Samsom. Retrieved April 6, 2023, from https://dare.uva.nl/search?identifier=c9c1cff4-0393-49dd-8191-39534204a5e4

van Hoek, C., Small, J., & van der Laan, S. (2016). Large-Area Phase Mapping Using PhAse Recognition and Characterization (PARC) Software. *Microscopy Today*, *24*(5), 12–21. https://doi.org/10.1017/S1551929516000572

Vogt, C., & Latkoczy, C. (2005). Laser Ablation ICP-MS. In *Inductively Coupled Plasma Mass Spectrometry Handbook* (pp. 228–258). John Wiley & Sons, Ltd. https://doi.org/10.1002/9781444305463.ch6

Wan, J., Du, H., Gao, F., Wang, S., Gao, M., Liu, B., & Zhang, Y. (2021). Direct Leaching of Vanadium from Vanadium-bearing Steel Slag Using NaOH Solutions: A Case Study. *Mineral Processing and Extractive Metallurgy Review*, *42*(4), 257–267. https://doi.org/10.1080/08827508.2020.1762182

Wang, Z.-h., Zheng, S.-l., Wang, S.-n., Liu, B., Wang, D.-w., Du, H., & Zhang, Y. (2014). Research and prospect on extraction of vanadium from vanadium slag by liquid oxidation technologies. *Transactions of Nonferrous Metals Society of China*, *24*(5), 1273–1288. https://doi.org/10.1016/S1003-6326(14)63189-7

WSA. (2021). Factsheet Steel and raw materials. https://worldsteel.org/wp-content/uploads/Factsheet-raw-materials-2023.pdf

WSA. (2024). World Steel in Figures 2024. Retrieved September 29, 2024, from https://worldsteel.org/data/world-steel-in-figures-2024/

Xiao, Y., & Pacheco, M. M. (2022). Iron ore agglomeration - Steel from Start to Finish [personal communication].

Yang, B., He, J., Zhang, G., & Guo, J. (Eds.). (2021). Chapter 3 - Vanadium mineral resources. In *Vanadium* (pp. 33–58). Elsevier. https://doi.org/https://doi.org/10.1016/B978-0-12-818898-9.00003-6

Zhang, S., Li, G., Xiao, R., Luo, J., Yi, L., & Rao, M. (2021). Extraction of vanadium from low-vanadium grade magnetite concentrate pellets with sodium salt. *Journal of Materials Research and Technology*, *15*, 5712–5722. https://doi.org/10.1016/j.jmrt.2021.11.039

Zhao, Q., Liu, C., Cao, L., Zheng, X., & Jiang, M. (2018). Effect of Lime on Stability of Chromium in Stainless Steel Slag. *Minerals*, *8*(10), 424. https://doi.org/10.3390/min8100424

Zheng, H., Zhang, W., Guo, Y., Gao, Q., & Shen, F. (2019). Transformation of Vanadium-Bearing Titanomagnetite Concentrate in Additive-Free Roasting and Alkaline-Pressure Leaching for Extracting Vanadium (V). *Minerals*, *9*(3), 197. https://doi.org/10.3390/min9030197

Zinngrebe, E., & van der Laan, S. R. (2014). Magnitude and causes of trace metal (V, Ba, Cr) leaching from slag in NEN 343 column tests [personal communication].

Zomeren, A. v., Laan, S. R. v. d., Kobesen, H. B. A., Huijgen, W. J. J., & Comans, R. N. J. (2011). Changes in mineralogical and leaching properties of converter steel slag resulting from accelerated carbonation at low CO2 pressure. *Waste Management*, *31*(11), 2236–2244. https://doi.org/https://doi.org/10.1016/j.wasman.2011.05.022

Appendix

A digital appendix is created to store a large number of results from the different analyses. The appendix can be found here:

https://www.dropbox.com/scl/fo/39qrdgi08teds8c2ks8ws/AK0eN8w5uog4cGbF97xQdxo?rlkey=bsfixssp4g13lk72j7wk9h1dv&st=730rq6md&dl=0

The content of the Appendix consists of:

- **Appendix A:** XRD results
  All XRD results of input materials and pellets in PDF format.
- **Appendix B:** XRF results
  All XRF results of input materials and pellets in pdf format as delivered by the analytical department of TSN.
- **Appendix C:** PARC results
  The results of the analysis of the pinhole traverses which were processed with PARC. This includes stitched greyscale images from the SEM and stitched images of the PARC results. Also, the mineral abundances of each image along the pinhole traverse are put in a graph.
- **Appendix D:** SEM-EDS point analysis JEOL 7001F
  All measurements, with their classification, performed with JEOL 7001F on the pellets, are collected in one Excel file. The numbers are displayed in atomic %, wt %, and wt % oxides.
- **Appendix E:** LA-ICP-MS results
  The raw, calibration and processed LA-ICP-MS data are in one Excel file.
- **Appendix F:** SEM-EDS point analysis JEOL 5900LV
  All SEM-EDS measurements with greyscale and data points are in PDF format.